

Optical Self-Phase Modulation in Graphene

by

Siddharatha Thakur

A thesis
presented to the University of Waterloo
in fulfilment of the
thesis requirement for the degree of
Master of Applied Science
in
Electrical and Computer Engineering

WATERLOO, ONTARIO, CANADA, 2018

Declaration

I hereby declare that I am the sole author of this thesis. This is a true copy of the thesis, including any required final revisions, as accepted by my examiners.

I understand that my thesis may be made electronically available to the public.

Abstract

Graphene is the first practically fabricated and stable two-dimensional material. It is an atomically thin layer of graphite with a unique gapless electronic band structure which leads to the observation of near-relativistic electron transport, 2.3% absorption of incident light, and a large nonlinear index of refraction. The relatively easy fabrication of graphene, coupled with its exceptional properties and integrability, makes this system unique for use in electronic and photonic circuits. Nonlinear optical processes in graphene stems from third-order nonlinear processes that originate from graphene's crystal symmetry. This nonlinearity manifests as frequency mixing, self-refraction and self-phase modulation as light traverses through the material. In literature thus far, this nonlinearity has been measured using different methods that probe the various nonlinear effects to report a large discrepancy (six orders of magnitude) in the value obtained for the nonlinear index of refraction (n_2). Large variations in this value disallow predictable behaviour when designing graphene integrated photonic devices. To this end, the thesis addresses this debate by systematically analysing the contributing factors to the variation in the nonlinear refractive index and forming a fundamental understanding of the governing processes that lead to the observed behaviour. Using the Z-scan technique, the effects of the wavelength and pulse-duration of the exciting source on the value of n_2 were studied. The Z-scan technique exploits light induced self-refraction to relate the change in transmittance to the value of n_2 . The pulse-duration measurement is conducted by taking a pulse and temporally stretching it with a dispersion-based prism set-up. In addition to that, using a pump-probe integrated Z-scan scheme, the temporal evolution of this nonlinearity is also studied. The combination of the pump-probe methodology, commonly used to study the dynamics of a system, and the Z-scan set-up gives an insight into the dynamic processes that contribute to the observed nonlinear behaviour. The n_2 of graphene is experimentally measured to depend quadratically on the wavelength, with n_2 growing larger with longer wavelengths. This result is also theoretically corroborated under a quantum theory developed by our group. The n_2 is also shown to grow larger as the pulse-duration grows larger in the hundreds of femtoseconds regime, a result predicted in a recent publication and shown by us. The temporal evolution of the nonlinearity follows the dynamics of the system, peaking at the zero-delay point and relaxing on the timescale of the effective decay of the system as dictated by the relaxation constants. The thesis does well to resolve a prevalent debate in the field of nonlinear optics of graphene by providing a systematic study on factors contributing to the discrepancy observed in literature, and in doing so opens a path to tuning the nonlinear behaviour as per the requirement of the application, which is limited in current silicon photonics.

Acknowledgements

During the course of my Master's degree I have been extremely fortunate to be afforded the opportunities that have allowed me to learn immensely alongside gifted colleagues and friends. It has been a period of my life where I learned about all facets of life. I'd firstly like to thank my parents for all their unconditional love and support. I'd also like to thank my friends, who have supported my goals, helped me when the path was uncertain, and gave me a reality check when life seemed nothing but chaos.

I would like to thank my supervisors, Dr. Hamed Majedi and Dr. Safieddin Safavi-Naeini for their utmost support and guidance. I would especially like to thank Dr. Majedi for giving me the opportunities that helped me grow as a researcher and as a person. I treasure our conversations on all topics spanning science, philosophy and life. I would also like to thank Dr. Behrooz Semnani for his friendship, mentorship and his knowledge. The project could not have reached its fruition without his help.

I would also like to thank the readers for this thesis Prof. Na Young Kim and Prof Simarjeet Saini for their time, I am grateful for their thoughts and reviews.

Contents

Declaration	ii
Abstract	iii
Acknowledgements	iv
List of Figures	vii
List of Tables	viii
1 Introduction	1
2 Nonlinear optical phenomena	3
2.1 Graphene	3
2.1.1 Crystal structure	4
2.1.2 Electronic structure	5
2.2 Nonlinear Response	7
2.2.1 Self-Refraction	8
2.3 Nonlinear Optics of Graphene: Brief Review	10
3 Spectral dependence of the effective Kerr coefficient of Graphene	17
3.1 Introduction	17
3.2 Z-scan Technique	18
3.2.1 Experimental Sources of Inaccuracy	19
3.3 Z-scan Experimental Set-up	24
3.3.1 Beam Characterisation	26
3.4 Spectrally-dependent Z-scan measurement	29
4 Pulse-width dependence of the effective Kerr coefficient of Graphene	36
4.1 Introduction	36
4.2 Effect of Dispersion	38
4.3 Prism-pair Pulse Stretching Set-up	41
4.3.1 Autocorrelation characterisation	44

4.4	Pulse-width dependent Z-scan measurement	47
5	Temporal evolution of the effective Kerr coefficient of Graphene	50
5.1	Introduction	50
5.2	Pump-probe Spectroscopy	51
5.3	Pump-probe Integrated Z-scan measurement	53
5.3.1	Experimental set-up	53
5.3.2	Temporal evolution of $n_{2,eff}$	54
6	Conclusions	58
	References	58
	Appendices	67
	Appendix A Mathematical Derivations	67
A.1	Gaussian Beam Equation (GBE)	67
A.2	Anharmonic Oscillator Model	73
A.2.1	Linear	74
A.2.2	Nonlinear	75
A.3	Nonlinear Refraction	79
	Appendix B Supplementary	85

List of Figures

2.1	Graphene crystal structure	4
2.2	Electronic band structure of graphene	7
2.3	Ray diagram of self-refraction in cubic nonlinear sample	9
3.1	Closed aperture (CA) transmittance and self-refraction illustrated for $\pm n_2$	18
3.2	Optical set-up used for the Z-scan measurement	24
3.3	LABVIEW program used for data acquisition	25
3.4	Beam profiles of the beam at 1050 nm at the locations of the focusing lens and far-field detector	27
3.5	Theoretical and experimental beam waist and Rayleigh lengths	28
3.6	Graphene characterisation	29
3.7	Z-scan profiles performed at 950 nm with three difference on-axis irradiance	31
3.8	Spectrally-dependent nonlinear refractive index	32
3.9	Z-scan profiles at wavelengths spanning 800-1050 nm with 50 nm increments	33
3.10	Carrier relaxation in graphene leading to Kerr-type nonlinearity	34
4.1	Prism-pair pulse stretching setup	42
4.2	Spectrum of the unmodified beam exiting the laser at 900 nm	44
4.3	Rotating mirror autocorrelator	45
4.4	Autocorrelation measurement for stretched pulses	46
4.5	Pulse-width dependence of $n_{2,eff}$	47
4.6	Z-scan profiles at 900 nm with pulse durations spanning 102-475 fs	48
5.1	Pump-probe integrated Z-scan	54
5.2	Temporal cross-correlation in graphene	55
5.3	Pump-probe integrated Z-scan measurement	56
A.1	Schematic illustration of a Gaussian beam [1]	72

List of Tables

2.1	Electronic and linear optical properties of Graphene	15
2.2	Nonlinear optical properties of Graphene	16
A.1	Maxwell Equations	67
B.1	Catalog of optical components and controllers used in experimental set up	86

Chapter 1

Introduction

The discovery of graphene opened up unimaginable avenues in a diverse array of scientific research and engineering design. This atomically thin single layer of graphite is unique because the very possibility of its existence was deemed improbable due to the laws of thermodynamics. However, its unique structure allows it stability making it the first practically fabricated two-dimensional material. Since its discovery in 2004, it has research in areas spanning electronics, chemistry, biomedical devices, mechanical devices, high-energy physics and countless others. As the dynamic of electronics and computing changes with the shift towards on-chip integrated devices, the applicability of lower dimensional materials becomes more pertinent. It is not only graphene's exceptional properties that makes it a sought after system, but a large part of its applicability is its dimensionality and how robust it is in that regime.

In addition to its well-known electronic properties, graphene also exhibits strong optical properties as well. In particular, we look at the strong light-matter interaction that graphene is capable of accommodating, which gives rise to a very strong nonlinear optical response. This is especially interesting due to the fact that this strong effect occurs at this reduced dimensionality. The nonlinear optical response can manifest as self-refraction, frequency mixing and self-phase modulation. Due to its integrability and strong nonlinear optical response, it makes it ideal for use in on-chip photonic circuits.

The nonlinear optical response has been studied both theoretically and experimentally by analysing the aforementioned phenomena. It is characterised by the parameter n_2 , which is the nonlinear index of refraction or the Kerr coefficient. However, the picture remains unclear regarding the characterisation of this nonlinearity. Depending on the method and experimental parameters, the nonlinearity varies largely in magnitude and sign with no consensus in the field. The motivation behind this work has been a more systematic and fundamental understanding of the effect of experimental parameters on the observed nonlinear effect. In doing so, we can understand how to modulate the effect in a controlled manner, if possible, and consolidate the results that have been reported thus far. Therefore, in this work we look at how the spectral and temporal properties of the impinging light effects the nonlinear response.

The thesis is organised to provide the reader with a self-consistent understanding of the work and

any relevant background information. The first chapter provides a detailed overview of the core technique of measurement, the Z-scan. After which the wavelength-dependent measurement of the $n_{2,eff}$ is presented. The parameter n_2 is referred to as $n_{2,eff}$ because we believe that the effect observed here is not purely electronic, which is what n_2 refers to. In addition to the experimental measurement, we also provide a theoretical validation of the observed trend. The second chapter focuses on probing the dependence on the pulse-width of the exciting source. The pulse is stretched using a dispersion based prism-pair set-up. The stretched beams are directed back into the original Z-scan set up. The set-up is elaborated upon and the results are presented thereafter. The third chapter presents a pump-probe integrated Z-scan set-up which provides a temporal evolution of the $n_{2,eff}$. This provides information regarding how impinging beam introduces a change in the carrier population resulting in the observation of nonlinear refraction. The measurement is achieved on a fast time-scale to attempt to probe the ultrafast dynamics in graphene. The final chapter presents succinct conclusions and future directions for the work.

Chapter 2

Nonlinear optical phenomena

A comprehensive understanding of any phenomena in experiment or theory necessitates an understanding of its origin. Most, if not all, electronic and optical phenomena stem from the material's crystallographic properties. The atomic distribution as described by the classification of crystal families and their characteristic symmetries prove fundamental in building theories that describe the macroscopic effects that are observed during experiment. Therefore, this chapter will provide a concise framework to provide the reader with background knowledge of the material and these processes, aiding the understanding of the experiments and discussions of this thesis. The chapter is divided into two primary sections. The first section presents a general discussion on the properties of graphene, placing it in perspective of the current landscape of scientific investigation and potential. The latter section provides a concise discussion on the nonlinear optical behaviour in graphene, with an emphasis on self-refraction, and the current state of the field. Due to graphene's unique structure, its nonlinear optical behaviour must be considered in a modified framework, while maintaining our understanding of the nonlinear optical behaviour of semiconductors presented as part of Appendix [A.2](#).

2.1 Graphene

Graphene is an atomically thin two-dimensional allotrope of carbon. It is the basic constituent of all graphitic compounds, i.e. fullerene, benzene rings, nanotubes. However fundamental its existence, the isolation of graphene only came to fruition very recently through a stroke of curiosity [\[2\]](#) in 2004. The isolation of a 2D crystal had been experimentally doubted due to the Mermin-Wagner theorem [\[3\]](#), which states that a crystal at this dimensionality cannot retain long-range order at any small but non-zero temperature due to thermal fluctuations, therefore it melts. The discovery of this new system revealed a plethora of new physics like the fact that electrons in graphene can be viewed as massless charged fermions living in 2D space, particles that are not encountered in our three-dimensional world, creating a bridge between solid-state physics and high-energy physics. This new physics has invited rigorous research on this system.

2.1.1 Crystal structure

The carbon (C) atoms in graphene form a honeycomb lattice attributed to a sp^2 hybridisation scheme. The electronic orbital configuration of an isolated C atom is $(1s)^2(2s)^2(2p)^4$, in a solid-state environment the $1s$ electronics remain more or less inert, but the $2s$ and $2p$ electrons hybridize. In the sp^2 hybridisation scheme, three sp^2 orbitals are formed leaving over a relatively pure p -orbital. In this case the orbitals arrange themselves in a plan at 120 deg angles, forming the honeycomb lattice. The honeycomb lattice is not a Bravais lattice as the two neighbouring sites are not equivalent. Both A and B sublattices are triangular Bravais lattice with a two-atom basis (A and B), as illustrated in Figure 2.1a. The three vectors connecting a site on the A sublattice to a nn on the sublattice B are given by vectors:

$$\boldsymbol{\delta}_1 = \frac{a}{2}(\sqrt{3}\mathbf{e}_x + \mathbf{e}_y), \quad \boldsymbol{\delta}_2 = \frac{a}{2}(-\sqrt{3}\mathbf{e}_x + \mathbf{e}_y), \quad \boldsymbol{\delta}_3 = -a\mathbf{e}_y \quad (2.1)$$

The distance between two nearest neighbouring (nn) carbon atoms is 0.142 nm. The triangular lattice is spanned by the basis vectors:

$$\mathbf{a}_1 = \sqrt{3}a\mathbf{e}_x, \quad \mathbf{a}_2 = \frac{\sqrt{3}a}{2}(\mathbf{e}_x + \sqrt{3}\mathbf{e}_y) \quad (2.2)$$

The modulus of the basis vectors yields the lattice spacing of $\tilde{a} = \sqrt{3}a = 0.24 \text{ nm}$, and the area of the unit cell is $A_{uc} = \sqrt{3}\tilde{a}^2/2 = 0.051 \text{ nm}^2$. The density of carbon atoms is given by $n_C = 2/A_{uc} = 39 \text{ nm}^{-2} = 3.9 \times 10^{15} \text{ cm}^{-2}$.

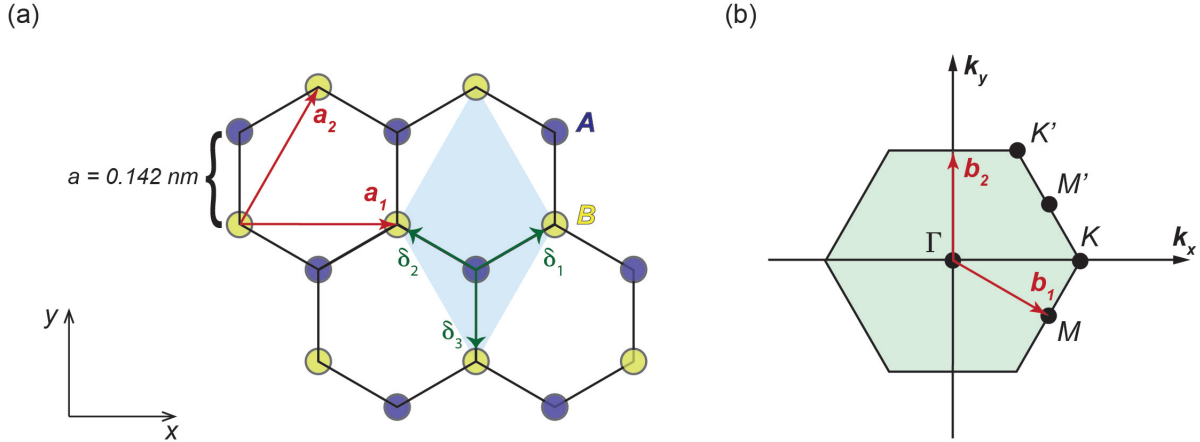


Figure 2.1: **Graphene crystal structure.** (a) Real space honeycomb lattice. The vectors $\boldsymbol{\delta}_1$, $\boldsymbol{\delta}_2$ and $\boldsymbol{\delta}_3$ connect the nn carbon atoms, separated by a distance of $a = 0.142 \text{ nm}$. The vectors \mathbf{a}_1 and \mathbf{a}_2 are basis vectors of the triangular Bravais lattice. (b) The triangular lattice in reciprocal space. Primitive lattice vectors are given by \mathbf{b}_1 and \mathbf{b}_2 . The shaded region is the first Brillouin zone (BZ), with the centre at Γ and two inequivalent points K and K' .

The reciprocal lattice, shown in Figure 2.1b, is defined with respect to the triangular Bravais lattice.

It is spanned by the vectors:

$$\mathbf{b}_1 = \frac{2\pi}{\sqrt{3}a}(\mathbf{e}_x - \mathbf{e}_y/\sqrt{3}), \quad \mathbf{b}_2 = \frac{4\pi}{3a}\mathbf{e}_y \quad (2.3)$$

The first Brillouin zone (FBZ), shaded region in Figure 2.1b), is defined as bounded by the planes bisecting the vectors to the nearest reciprocal lattice points. This gives a FBZ of the same form as the original hexagons of the honeycomb lattice, rotated with respect to them by $\pi/2$. The long wavelength excitations are situated in the vicinity of the Γ point, in the centre of the FBZ. One distinguishes the six corners of the FBZ, which consist of inequivalent points K and K' represented by the vectors:

$$\pm \mathbf{K} = \pm \frac{4\pi}{3\sqrt{3}a}\mathbf{e}_x \quad (2.4)$$

These crystallographic points, known as the Dirac points, play an essential role in the electronic properties of graphene.

2.1.2 Electronic structure

The electronic band structure of graphene can simply be described under a tight-binding (TB) model considering the nn carbon atoms. The electrons in the covalent bonds form deep fully filled valence bands, and thus their effects on the conductivity can be safely disregarded. The unhybridized p -orbital is only slightly perturbed by the neighbouring atoms. The TB Hamiltonian is given by [4]:

$$\mathcal{H} = -t \sum_{\mathbf{R}, \delta} c_{\mathbf{R}+\delta}^\dagger c_{\mathbf{R}} \quad (2.5)$$

where \mathbf{R} is a lattice point, and δ is the displacement to a nn lattice point. An electron at site \mathbf{R} can hop to any neighbouring sites, i.e. if $|\mathbf{R}\rangle$ denotes a state with one electron which is at \mathbf{R} we have:

$$\langle \mathbf{R} + \delta | \mathcal{H} | \mathbf{R} \rangle = -t \quad (2.6)$$

where t is the hopping energy between the two sites. If \mathbf{R} and \mathbf{R}' are not neighbours then, $\langle \mathbf{R}' | \mathcal{H} | \mathbf{R} \rangle = 0$. Looking at eigenvalues for the Hamiltonian, we consider a state with amplitude $\phi_{\mathbf{R}}$ for the electron at site \mathbf{R} . The eigenvalue equation is then:

$$-t \sum_{\delta} \phi_{\mathbf{R}+\delta} = \epsilon \phi_{\mathbf{R}} \quad (2.7)$$

We look for amplitudes which vary like $e^{i\mathbf{k}\cdot\mathbf{r}}$. This is the Bloch wave function. There will be different amplitudes ψ_A and ψ_B for sublattices A and B. An atom on sublattice A has neighbouring atoms all on sublattice B at displacements $(0, -a)$, $(\sqrt{3}a/2, a/2)$ and $(-\sqrt{3}a/2, a/2)$. An atom on sublattice B has three neighbours on sublattice A at displacements $(0, a)$, $(\sqrt{3}a/2, -a/2)$ and $(-\sqrt{3}a/2, -a/2)$. So the eigenvalue ϵ and the amplitudes ψ_A and ψ_B are determined for each wavevector \mathbf{k} , from the

two equations:

$$-t(e^{ik_y a} + 2e^{-ik_y a/2} \cos \frac{\sqrt{3}}{2} k_x a) \psi_A = \epsilon \psi_B \quad (2.8)$$

$$-t(e^{-ik_y a} + 2e^{ik_y a/2} \cos \frac{\sqrt{3}}{2} k_x a) \psi_B = \epsilon \psi_A \quad (2.9)$$

The eigenvalues are then given by:

$$\mathcal{E} = \pm t \left| e^{ik_y a} + 2e^{-ik_y a/2} \cos \frac{\sqrt{3}}{2} k_x a \right| \quad (2.10)$$

$$\begin{aligned} \mathcal{E} = \pm t \left[\left(\cos(k_y a) + 2 \cos \left(\frac{1}{2} k_y a \right) \cos \left(\frac{\sqrt{3}}{2} k_x a \right) \right)^2 + \right. \\ \left. \left(\sin(k_y a) - 2 \sin \left(\frac{1}{2} k_y a \right) \cos \left(\frac{\sqrt{3}}{2} k_x a \right) \right)^2 \right]^{\frac{1}{2}} \end{aligned} \quad (2.11)$$

There are two bands one with positive energy and the other with negative energy, and they touch at the corners of the Brillouin zone, at the Dirac points. Due to the fact that here are two electrons per unit cell, the lower band is completely filled and upper band is completely empty, placing the Fermi energy at $\mathcal{E}_F = 0$. In order to compute the dispersion relation in the vicinity of these zone corners where the energy tends to zero, we write; $\mathbf{k} = \mathbf{K} + \mathbf{q}$, where \mathbf{K} is the wavevector given by Eq. 2.4, and we assume \mathbf{q} is small and is the momentum measured relative to the Dirac points. Rewriting the Hamiltonian from Eq. 2.8 for a fixed- \mathbf{k} as:

$$\mathcal{H}(\mathbf{k}) = \begin{bmatrix} 0 & F(k_x, k_y) \\ F^*(k_x, k_y) & 0 \end{bmatrix} \quad (2.12)$$

where $F(k_x, k_y) = e^{ik_y a} + 2e^{-ik_y a/2} \cos \frac{\sqrt{3}}{2} k_x a$. To obtain the lowest order in \mathbf{q} we have, $F(k_x, k_y) = \frac{3}{2}a(q_x + iq_y)$ and therefore:

$$\mathcal{H}(\mathbf{k}) = \hbar\nu\boldsymbol{\sigma} \cdot \mathbf{q} \quad (2.13)$$

where the speed ν is given by: $\nu = \frac{3at}{2\hbar}$ and is around 10^6 m/s, and σ_x and σ_y are Pauli spin matrices. Hence the eigenvalues of $\mathcal{H}(\mathbf{k})$ are:

$$\mathcal{E} = \pm \hbar\nu q \quad (2.14)$$

This is the linear dispersion relation near the Dirac points that dictates the cone-like band structure synonymous with graphene, shown in Figure 2.2.

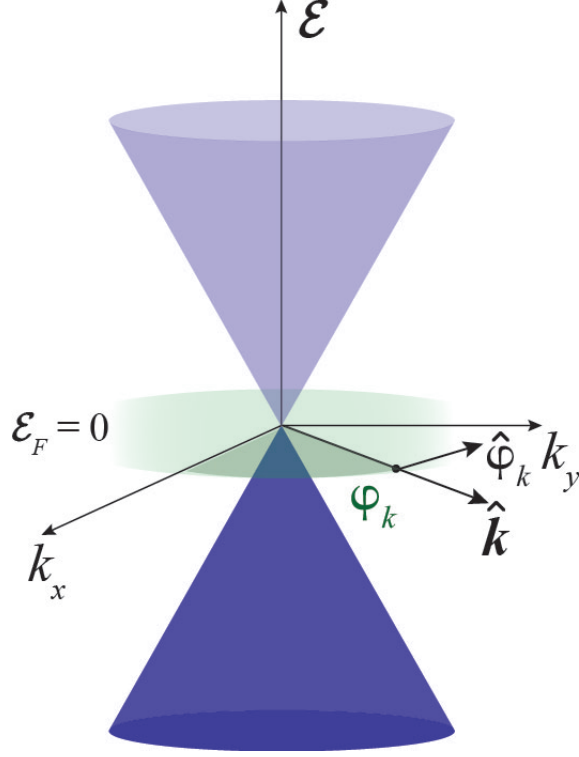


Figure 2.2: **Electronic band structure of graphene.** The linear dispersion relation in graphene at a Dirac point. Intrinsic graphene has a Fermi energy, $\mathcal{E}_F = 0$, shown in the figure.

2.2 Nonlinear Response

The nonlinear optical response in graphene stems from strong light-matter interaction that graphene is capable of accommodating and is characterised by the intensity dependent third order optical conductivity, $\sigma^{(3)}$, which is the first allowed nonlinear term due to the centrosymmetric symmetry of the lattice. In conventional nonlinear optics based on a semiconductor system, the nonlinear responses is derived using the Taylor expansion of the electrical susceptibility in electrical field to obtain the polarisation field vector with higher order terms. This is provided in Appendix A.2. The derivation in terms of optical conductivity provides the same response by relating the current density, i.e. $\mathbf{J}(\omega)$ to the electrical field, i.e. $\mathbf{E}(\omega)$ at a general frequency, ω . However, as shown in the previous subsection, graphene presents a unique electronic structure where the conventional semiconductor based nonlinear optics may not completely encompass the physics. Therefore, a short concise description of the third order nonlinear optical phenomena in a modified framework unique to graphene is provided here [5].

The optical response in graphene is influenced by the chiral nature of the carriers and the scale invariance of the band structure in the low energy limit. Chirality in the context of graphene refers to the pseudospin being locked parallel or antiparallel to the direction along which the electron propagates. Scale-invariance refers to properties of a system that remain universal regardless of

the scales of length, energy or other variables. One of the consequences of these properties is that graphene exhibits a universal optical response absorbing 2.3% of the normally incident light. Another consequence of these properties is the large nonlinear optical response observed in graphene upon irradiation, which has been conclusive regardless of the framework of the formulation. To circumvent computational and interpretive difficulties, Semiconductor Bloch Equations (SBEs) are employed. Using SBEs the contribution of both intraband and interband dynamics can be analysed. The SBEs introduce an effective dipole in reciprocal space that are able to reveal the peculiarities of graphene in terms of its optical response. Under a perturbative treatment, the higher order optical coefficients inherit a nonresolvable singularity. This singularity is a consequence of the topological properties of the band structure and the chiral nature of the charged carriers. Following a many-body analysis, it is revealed that under an electromagnetic field the charged carriers in the vicinity of the Dirac points undergo ultra-fast Rabi oscillations accompanied with slower relaxation dynamics, resulting in an unconventional saturation effect. This spontaneous saturation effect has been revealed to be imperative in the nonlinear optical response in graphene, deviating the behaviour from conventional semiconductor third order nonlinearity [6, 7]. The singularity is resolved by excluding the saturated states from the solution domain.

The process of third order frequency mixing can be understood as a three-photon processes with three complex time dependent fields, $e^{i\omega_p t}$, $e^{i\omega_q t}$ and $e^{i\omega_r t}$ mixing through the third-order conductivity. Different terms contribute to the conductivity tensor and therefore contribute to the mixing via pure interband, pure intraband, and a combination of both. The intraband dynamics cause the quasiparticles to travel along the trajectory determined by the direction of the electric field at the graphene plane. The interband dynamics occur between the two level transition of the quasiparticles predominantly around the zero detuning region. The different three-photon processes that are possible are: (i) pure intraband, (ii) pure interband, (iii) interband-intraband, (iv) interband-interband-intraband, (v) intraband-intraband-interband, (vi) intraband-interband-intraband, and (vii) interband-intraband-intraband.

2.2.1 Self-Refraction

There are several effects that originate from a cubic nonlinearity such as harmonic generation, four-wave mixing and self-phase modulation, which are applicable in their respective applications. The focus of this work is on self-phase modulation which is observed as the *self-refraction* that an optical beam undergoes as it traverses through a nonlinear medium, commonly known as the Kerr effect. In Appendix A we developed a mathematical framework for nonlinear optical phenomena, and now we can relate a macroscopic observable to this theory.

Keeping Eq.(A.53) in mind, we see that the contribution of n_2 to the cumulative refractive action is contingent on the intensity as described by the relation:

$$n = n_0 + n_2 I \tag{2.15}$$

Considering a Gaussian beam where the intensity of the beam peaks at the center, the greatest effect of self-refraction is seen near the center and then decreases as one moves away from the center. This profile is similar to that of a graded-index optical fiber. Taking $n_2 > 0$ and employing some basic ray tracing, it would appear that the rays bend towards the optical axis, thereby increasing the on-axis amplitude resulting in *self-focusing*. This results in the sample causing the beam to diverge before the focal plane, and converge after the focal plane. This is schematically illustrated in Figure 2.3a. Intuitively, such strong refraction would indicate an infinite on-axis amplitude, however, the minimum beam waist is limited by diffraction. The effect of diffraction here causes the beam to spread. Given a long interaction length, thick sample, the beam will again experience strong refraction, until it is spread by diffraction, resulting in *periodic focusing* [8]. It is possible to derive a set of beam parameters for a particular sample where refraction and diffraction can be balanced to allow linear transmittance through the sample [9]. If $n_2 < 0$, *self-defocusing* occurs, where the sample causes convergence of the beam before the focal plane and causes divergence after the focal plane. This is shown in Figure 2.3b. This will be re-visited again in Section 3.2 in the context of the Z-scan measurement.

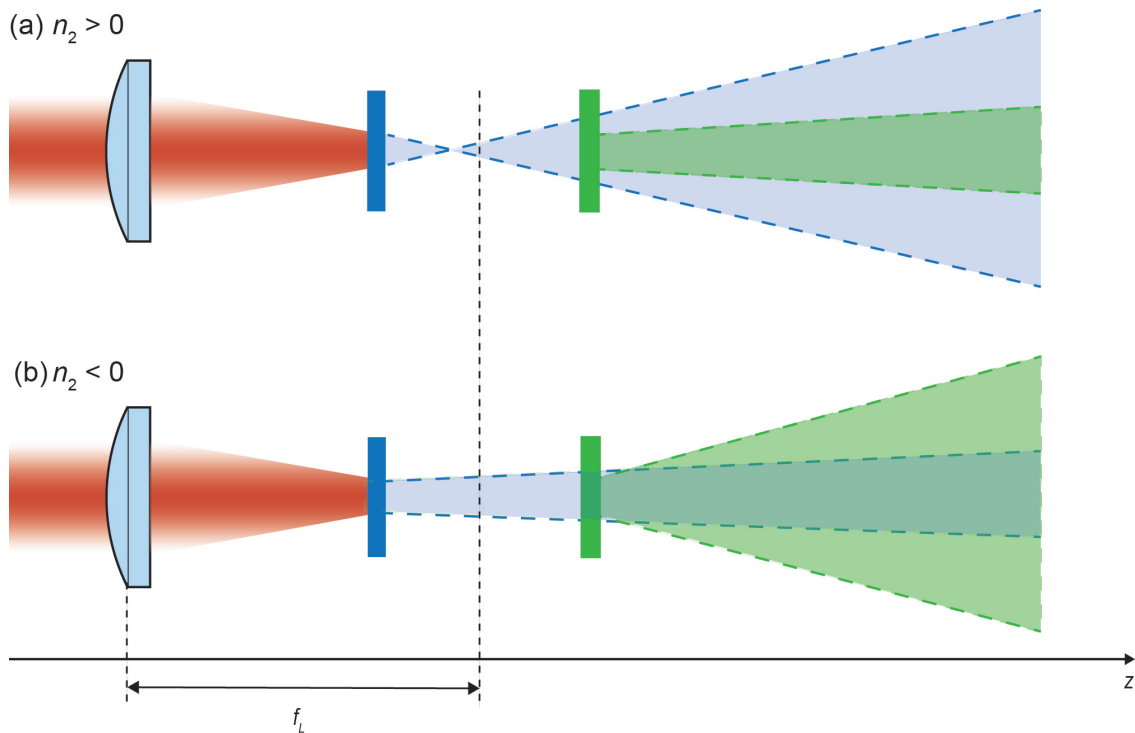


Figure 2.3: **Ray diagram of self-refraction in cubic nonlinear sample.** A lens of focal length f_L is used to focus down the incident beam and the sample is scanned along the optic axis across the confocal parameter (twice the Rayleigh length, (z_R) centred at the focal plane. The blue ray lines indicate the self-refraction when the sample is behind the focal plane, while the green ray lines show self-refraction when the sample is in front of the focal plane for a nonlinear sample with (a) $n_2 > 0$ and (b) $n_2 < 0$

With self-refraction stemming from an intensity-dependent phenomenon, it intuitively follows that there are specific conditions under which *self-focusing/defocusing* occurs. Two main points to consider are the relative contributions of n_0 and n_2 in Eq. (2.15) to total refraction, and the competing effects of diffraction and refraction. An expression for the critical power required for self-refraction is derived in Appendix A and is given by [8]:

$$\boxed{P_{cr} = \frac{c\epsilon_0\lambda^2}{8\pi n_2}} \quad (2.16)$$

From this expression it is seen that the beam power must exceed this threshold, *not the intensity*, for self-refraction to occur. Even if the beam is focused tighter, self-refraction will not occur as diffraction will also increase with a reduction in beam diameter.

2.3 Nonlinear Optics of Graphene: Brief Review

The investigation of graphene’s nonlinear electrodynamic response was incepted in the theoretical work of Mikhailov [10]. The primary result of this investigation was the expectancy of the generation of higher harmonics, i.e. third harmonic generation, with high up-conversion efficiency. Even though this discussion will not delve into theoretical work, since this thesis is primarily an experimental study, however, it is important to appreciate origin of this field of study as being a theoretical demonstration. To satiate the curious reader, several theoretical works that followed, in conjunction with experiment, have aided in our understanding of the nonlinear electrodynamic response of graphene and can be found in these references: [11–21].

With the initial theoretical demonstration of a strong nonlinear response in graphene, Hendry *et al.* [22] as part of Mikhailov’s group experimentally measured the third order susceptibility using four-wave mixing (FWM) using 6 ps pulses. The samples in this study were obtained using mechanical exfoliation and were deposited on a 100 μm thick glass cover slip. The principle of this technique is the generation of mixed optical frequency harmonics $\omega_e = 2\omega_1 - \omega_2$ under irradiation by two monochromatic waves with frequencies ω_1 and ω_2 . Experimentally this is accomplished as follows: two incident pump laser beams with wavelength λ_1 and λ_2 are focused collinearly onto a sample and mix together to generate a third, coherent beam of wavelength λ_e [22]. The result of the frequency mixing process is governed by the interplay of energy and momentum conservation, therefore is controlled by tuning the incident pump wavelengths.

The amplitude of the emission peak showed a cubic dependence on the intensity of the pump pulses, confirming the third-order nature of the response. The strength of the response is quantified by the familiar parameter of the third-order susceptibility $\chi^{(3)}$ (Eq. A.49), which relates the polarisation per unit volume to the third power of the electric field. However, it was argued that when considering a two-dimensional material, it is more appropriate to describe the response in terms of a sheet current $j^{(3)}$ and the third-order surface dynamical conductivity $\sigma^{(3)}$. Using an effective nonlinear susceptibility normalised with the effective thickness of a graphene layer, the

value of $|\chi_{gr}^{(3)}| \simeq 1.5 \times 10^{-7}$ esu or $n_2 \sim 10^{-9}$ cm²/W was obtained. All relevant values for the linear and nonlinear parameters reported in literature are summarised at the end of this section in Table 2.1 and Table 2.2, respectively. The large nonlinear response in graphene compared to other materials is attributed to the fact that all vertical (interband) transitions in graphene are resonant at all frequencies ω_1, ω_2 and ω_e . An interesting result of sheet current formulation was the observation that the strength of the nonlinear response in graphene has a λ^4 dependence.

Krishna *et al.* [23] also measured the nonlinear response of graphene using FWM as part of a larger study investigating the nonlinear optical properties of graphene-metal composite materials. They measured a $|\chi_{gr}^{(3)}| \simeq 4.2 \times 10^{-12}$ using 6 ns pulses at 532 nm. The graphene sheets were placed in a dimethylformamide (DMF) suspension. The nonlinear absorption coefficient was also measured using the open-aperture Z-scan method, which will be elaborated upon shortly and in detail in Section 3.2. In the nanosecond regime, graphene shows reverse saturable absorption with a value of $\beta \simeq 9 \times 10^{-7}$ cm/W. The parameter β quantifies the nonlinear absorption of the system. In a more application based study, Ciesielski *et al.* [24] measure the near-degenerate FWM signal of graphene as a nonlinear optical signal to determine the spectral phase profile of laser pulses in the focus of microscope objectives. The graphene was obtained with micromechanical exfoliation and then deposited on glass and studied using a 800 nm laser with 15 fs pulse duration. In this regime, a value of $|\chi_{gr}^{(3)}| \simeq 4.2 \times 10^{-6}$ is obtained. The deviation from Hendry's study [22] is attributed to the tight focusing of the excitation pulse. The previously mentioned λ^4 is also observed here showing a 40% variation within the 100 nm spectral bandwidth of the pulse. The impact of the scaling factor on the emitted intensity is unresolvable due to the spectral integration and the mixing of the frequency components which leads to a broad structureless emission spectrum.

Self-phase modulation observed via the action of self-refraction is previously discussed in Section 2.2.1, is the most common means of measuring the third order optical nonlinearity using the Z-scan measurement. This technique is the central tool of investigation in this thesis and will be explored in detail in Section 3.2. The basic principle behind the technique is that the self-refraction experienced by an incident beam traversing through a nonlinear material can be quantified by the transmittance observed in the far-field. The change in transmittance obtained in a closed aperture configuration (CA) i.e. aperture in the far-field, is related to the nonlinear phase shift and consequently the nonlinear refractive index, n_2 as defined in Eq. A.53. Transmittance obtained in an open-aperture configuration (OA), i.e. no aperture in the far-field, gives information regarding nonlinear absorption. Zhang *et al.* [25] used the Z-scan measurement to obtain both the real and imaginary parts of the complex refractive index of graphene. The graphene layers were fabricated using chemical vapour deposition (CVD) and then transferred onto a quartz substrate. The measurement was conducted using a laser with center wavelength 1550 nm and 3.8 ps pulse duration. The CA measurement revealed that the induced nonlinear phase shift has a power dependence characteristic of saturable absorption. A value of $n_2 \simeq -10^{-7}$ cm²/W is obtained in the low intensity regime, as n_2 is observed to decrease with increasing intensity. A value of $I_{sat} = 74$ MW/cm² for saturation intensity is reported. Comparing the value obtained by Hendry *et al.* [22]

in terms of n_2 which is $1.5 \times 10^{-9} \text{ cm}^2/\text{W}$, it is hypothesized that the discrepancy is attributed to the measured third-order susceptibility having multiple origins. The parametric process of FWM arises from the coherent electronic response, while the Z-scan measurement is a measure of the cumulative nonlinear response i.e. thermal or free-carrier.

The third-order optical response of monolayer to multilayer graphene was studied in the femtosecond regime by Chen *et al.* [26]. In particular the contribution of interlayer coupling was analysed. The graphene samples were all grown naturally by CVD and transferred to quartz substrate. To analyse the effect of decoupling, individual layers were transferred and stacked on top of each other, and compared to naturally grown samples of the same thickness. The Z-scan measurement was performed using a source centred at 733 nm with a pulse duration of 100 fs and a repetition rate of 80 MHz. The nonlinear refraction index was found to be $n_2 \simeq 1.4 \times 10^{-9} \text{ cm}^2/\text{W}$, while the nonlinear absorption coefficient was found to be $\beta \simeq 6 \times 10^{-6} \text{ cm}/\text{W}$ for monolayer samples. It should be pointed out that in the picosecond [25] and femtosecond [26] regimes, graphene shows strong saturable absorption in contrast to the reverse saturable absorption observed in the nanosecond regime [23]. This is important to mention as the nonlinear effect of graphene is closely related to the photon excited times and the dynamics of the system in particular excitation regimes. In graphene, photoexcited electron-hole pairs thermalise via carrier-carrier scattering and phonon emission within ~ 150 fs, a timescale denoted by τ_1 , to reach a new Fermi-Dirac distribution. This is followed by interband carrier relaxation and hot phonon emission on the picosecond timescale, denoted by τ_2 . Returning to the main motivation of study for this article, the result of this study was the conclusion that the intrinsic linear dispersion of monolayer graphene is imperative to obtaining a large nonlinearity as coupling of sheets modifies the band structure i.e. loss of linear dispersion in bi-layer, and thereby reduces the degree of nonlinearity. With Z-scan measuring the cumulative nonlinearity, high repetition rate sources tend to induce large thermal nonlinearities which dominate over the electronic nonlinearities. In the case of graphene it is argued that this issue can be ignored due to graphene being extremely heat-stable and the heat relaxation time of graphene (~ 1.4 ns) being shorter than the repetition time between pulses (12.5 ns) [26]. That is to say that the heat accumulation injected by one pulse has enough time to dissipate before the next pulse arrives.

Considering the λ^4 dependence of the optical nonlinearity, it follows that the nonlinear response would be larger in the mid-IR regime, compared to the visible and near-IR wavelengths used in the aforementioned studies. To this end Miao *et al.* [27] used a home-made mid-IR Z-scan measurement to identify the real and imaginary parts of the third-order susceptibility of graphene. The monolayer graphene sample was CVD grown and transferred to quartz. A pump-probe measurement was conducted using an 800 nm source with 100 fs pulses to reveal a fast time constant of 200 fs and a slower time constant of 1.07 to 2.0 ps, depending on pump intensity. At higher excitation intensity, electron relaxation creates a large quantity of optical phonons which could couple energy back into the electron distribution, therefore slowing down the cooling rate. For the Z-scan measurement, a laser centred at 1930 nm with pulse duration of 2.8 ps, and another source centred at 1562 nm

with pulse duration 1.5 ps were used. Values of $n_2 \simeq 4.58 \times 10^{-7} \text{ cm}^2/\text{W}$ and $1.64 \times 10^{-7} \text{ cm}^2/\text{W}$ are obtained for the two different wavelengths, respectively. The ratio of n_2 at 1.93 and 1.56 μm is about 2.8, which is a deviation from the λ^4 dependence which would have a ratio of 2.3. The deviation is attributed to experimental errors. It is emphasized that that Z-scan is a measure of all contributions to nonlinear refraction, not just the pure electronic response.

A comparative study in mid-IR but with femtosecond pulses was performed by Demetrious *et al.* [28]. The measurement was carried out using the Z-scan method at 1150, 1550, 1900 and 2400 nm with a 100-femtosecond laser source on multilayer (5-7) graphene to yield a negative values for n_2 ranging from -2.5×10^{-9} to $-0.55 \times 10^{-9} \text{ cm}^2/\text{W}$ for the respectively range of wavelengths. The samples were CVD grown and transferred onto quartz. The study specifically points out the intensity dependent nature of the nonlinear optical response measured by the Z-scan and the contribution of higher order processes (i.e. $\chi^{(5)}, \chi^{(7)}$) that would make the conventional n_2 coefficient unsuitable to describe the effect. With increasing intensities the effect of two photon absorption is also seen in the OA profiles. A thermal analysis is provided to discount the contribution of thermal effects, in addition to the use of a low repetition rate (1 kHz) laser source, which is unnecessary as discussed previously [26].

In addition to FWM and Z-scan measurement, the Optical Kerr Gate (OKG) measurement is also used to measure the third-order nonlinear susceptibility [29]. Conducted in a pump-probe configuration, the pump induces a transient uniaxial birefringence in the medium, while the probe, rotated 45° relative to the pump beam, undergoes optical retardance as it transverses through. This effect is similar to that of a quarter-wave plate that transforms a linearly polarised beam to circular polarisation, therefore, maximum OKG signal is obtained at 45° [30]. Using this method in conjunction with the Z-scan method, Dremetsika *et al.* [31] investigated the sign and magnitude of the n_2 of graphene. The OKG method is advantageous over the Z-scan method as it only probes the nonlinearity deriving from the electronic response, while the Z-scan probes the cumulative response of the system. The excitation source for this measurement is a source centred at 1600 nm with 180 fs pulse duration. The OKG set-up is coupled to optical heterodyne detection (OKG-OHD) to maximise the signal-to-noise ratio. A negative value of $n_2 \simeq -1.07 \times 10^{-9} \text{ cm}^2/\text{W}$ is obtained using this method. Performing the Z-scan measurement on the same sample using a source centred at 1500 nm with 3.8 ps pulse duration gives a value of $n_2 \simeq -2 \times 10^{-8} \text{ cm}^2/\text{W}$. The difference in the values obtained with these two methods is attributed to the electronic and cumulative nonlinear responses being probed. To complement their experimental work and the use of OKG-OHD, Dremetsika *et al.* [32] developed a 2D-OHD-OKE to measure separately the time response of the two main tensor components of the nonlinear susceptibility. They validate that the out-of-plane tensor components are small and show that the $\chi_{xyxy} + \chi_{xyyx}$ components account for the fast birefringent response while the χ_{xxyy} component has a slower (ps) relaxation time.

OKG and Z-scan were also used together to measure the n_2 of single and multi-layer graphene. In this study Ahn *et al.* [33] use these methods to derive dependence of n_2 on the wavelength and fluence. The wavelengths used were 720, 800, 940 and 1230 nm, all having a pulse duration of 100

fs. In contrast they obtain a positive value for the n_2 using both methods, with the n_2 increasing as the excitation tends to longer wavelengths. Our spectrally dependent study was also presented in a conference prior to the publication of this article [34] and revealed a similar dependence of n_2 on excitation wavelength.

The argument between the plus and minus sign for the n_2 value is one that cannot be unambiguously answered. There are discrepancies in theoretical works on this depending on the method of calculation and parameters considered. The theoretical study by Ooi *et al.* [12], Cheng *et al.* [11] and Semnani *et al.* [14] conclude in their respective theoretical formulations that the value of n_2 may take positive or negative values in specific ranges of Fermi-levels. Experimentally speaking, this occurs due to doping or electric field modulation. Therefore, difference in measurement methods, experimental conditions, and sample preparation techniques should be considered when comparing and discussing different studies.

Table 2.1: Electronic and linear optical properties of Graphene

Value(s)	Sample	Method	Experimental Parameters	Ref.
Relaxation time, τ (ps)				
$\tau_1 = 0.2$ $\tau_2 = 1.07 - 2.0$	CVD graphene transferred onto quartz	Pump-probe spectroscopy	$\lambda_{pump/probe} = 800$ nm $\tau_{pulse} = 100$ fs $f = 1$ kHz	[27]
$\tau_1 = 0.07 - 0.12$ $\tau_2 = 0.4 - 1.7$	Multi-layer epitaxial graphene on SiC	Pump-probe spectroscopy	$\lambda_{pump/probe} = 780$ nm $\tau_{pulse} = 85$ fs $f = 3$ kHz	[35]
$\tau_1 = 0.13 - 0.33$ $\tau_2 = 3.5 - 4.9$	Graphene dispersions in various solvents (water, THF, DMF)	Pump-probe spectroscopy	$\lambda_{pump/probe} = 790$ nm $\tau_{pulse} = 80$ fs $f = 383$ Hz	[36]
$\tau_1 = 0.2$ $\tau_2 = 2.5$	Exfoliated graphene on SiO ₂ /Si	Pump-probe spectroscopy	$\lambda_{pump/probe} = 800/1300$ nm $\tau_{pulse} = 150$ fs $f = 80$ MHz	[37]
Linear Refractive Index, n				
2.75 – 1.56i	Graphene on SiO ₂	Refln	1550 nm	[38]
Linear Absorption Coefficient, α (cm⁻¹)				
7.4×10^{-4}	Graphene placed across aperture	Transmittance and reflectance		[39]
Saturation Intensity, I_S (W/cm²)				
$4(\pm 1) \times 10^9$	Epitaxial graphene on SiC	Z-scan		[40]
(2.3, 2.6, 2.6) $\times 10^{10}$	Graphene dispersions in various solvents (water, THF, DMF)	Z-scan	$\lambda_{in} = 790$ nm $\tau_{pulse} = 80$ fs $f = 383$ Hz	[36]
7.4×10^7	CVD graphene transferred onto quartz	Intensity dependent transmittance	$\lambda_{in} = 1550$ nm $\tau_{pulse} = 3.8$ ps $f = 10$ MHz	[25]
(4.5, 3, 2.1, 1.9) $\times 10^9$	CVD graphene transferred onto quartz	Intensity dependent transmittance	$\lambda_{in} = 1150, 1550, 1900, 2400$ nm $\tau_{pulse} = 100$ fs $f = 1$ kHz	[28]
(0.1, 11.7) $\times 10^7$	CVD graphene transferred onto quartz	Z-scan	$\lambda_{in} = 1930, 1562$ nm $\tau_{pulse} = 2.8, 1.5$ ps $f = 32.3, 20.8$ MHz	[27]

Table 2.2: Nonlinear optical properties of Graphene

Value(s)	Sample	Method	Experimental Parameters	Ref.
Third-order Susceptibility, $\chi^{(3)}$ (esu)				
Nonlinear Refractive Index, n_2 (cm²/W)				
$ \chi^{(3)} = 1.5 \times 10^{-7}$	Mechanically exfoliated graphene deposited on 100 μm glass cover slip	FWM	$\lambda_1 = 670\text{-}980$ nm $\lambda_2 = 1130\text{-}1450$ nm $\tau_{pulse} = 6$ ps	[22]
$ \chi^{(3)} = 4.2 \times 10^{-12}$	Graphene suspension in DMF	FWM	$\lambda_{in} = 532$ nm $\tau_{pulse} = 6$ ns $f = 10$ Hz	[23]
$ \chi^{(3)} = 4.3 \times 10^{-6}$	Graphene suspension in DMF	FWM	$\lambda_{in} = 800$ nm $\tau_{pulse} = 15$ fs $f = 80$ MHz	[24]
$n_2 = -1 \times 10^{-7}$	CVD graphene transferred onto quartz	Z-scan	$\lambda_{in} = 1550$ nm $\tau_{pulse} = 3.8$ ps $f = 10$ MHz	[25]
$n_2 = 1.4 \times 10^{-9}$	CVD graphene transferred onto quartz	Z-scan	$\lambda_{in} = 733$ nm $\tau_{pulse} = 100$ fs $f = 80$ MHz	[26]
$n_2 = 4.58 \times 10^{-7}, 1.64 \times 10^{-7}$	CVD graphene transferred onto quartz	Z-scan	$\lambda_{in} = 1930, 1562$ nm $\tau_{pulse} = 2.8, 1.5$ ps $f = 32.3, 20.8$ MHz	[27]
$n_2 = -2 \times 10^{-8}$	CVD graphene transferred onto quartz	Z-scan	$\lambda_{in} = 1550$ nm $\tau_{pulse} = 3.8$ ps $f = 10$ MHz	[31]
$n_2 = -1.07 \times 10^{-9}$	CVD graphene transferred onto quartz	OKG-OHD	$\lambda_{in} = 1600$ nm $\tau_{pulse} = 180$ fs $f = 82$ MHz	[31]
$n_2 = -10^{-9}$	Graphene covered silicon-on-insulator (SOI) waveguide	Chirped-Pulse-Pumped Self-Phase Modulation	$\lambda_{in} = 1550$ nm	[41]
$ \chi^{(3)} = 10^{-7} - 10^{-6}$	CVD graphene transferred onto quartz; 1,2,4 layers	Z-scan and OKG	$\lambda_{in} = 720\text{-}1230$ nm $\tau_{pulse} = 100$ fs $f = 80$ MHz	[33]
Nonlinear Absorption Coefficient, β (cm/W)				
9×10^{-7}	Graphene suspension in DMF	Z-scan	$\lambda_{in} = 532$ nm $\tau_{pulse} = 6$ ns $f = 10$ Hz	[23]
$(1.2\text{-}4.4) \times 10^{-8}$	Graphene dispersions in various solvents (water, THF, DMF)	Z-scan	$\lambda_{in} = 790$ nm $\tau_{pulse} = 80$ fs $f = 383$ Hz	[36]
6×10^{-6}	CVD graphene on quartz	Z-scan	$\lambda_{in} = 733$ nm $\tau_{pulse} = 100$ fs $f = 80$ MHz	[26]
$(0.38, 0.9, 1.5, 1.9) \times 10^{-5}$	CVD graphene transferred onto quartz	Z-Scan	$\lambda_{in} = 1150\text{-}2400$ nm $\tau_{pulse} = 100$ fs $f = 1$ kHz	[28]

Chapter 3

Spectral dependence of the effective Kerr coefficient of Graphene

3.1 Introduction

The focus of this thesis is probing the spectral and temporal dependence, and evolution of the third order susceptibility of graphene. To this end, the Z-scan measurement is the technique that is central to the study. To probe the properties of interest, the basic measurement setup is integrated with a prism pulse-stretching and pump-probe setup. In the first set of experiments, the Z-scan method is used in its intrinsic form to measure the spectral dependence of the effective n_2 , referred to hereinafter as $n_{2,eff}$. The use of this verbiage will become more clear through the discussion of the experimental results of this thesis. In essence, n_2 refers to the pure electronic response of system resulting in the observation of nonlinear refraction. However, given experimental conditions and methods, the observed effect may not stem *only* from the electronic response, but can include contribution from another phenomenon. Therefore, it is more appropriate to use the aforementioned verbiage. This chapter includes three primary sections. The first section will provide a detailed experimental background on the Z-scan technique, including a general theory of the technique and sources of inaccuracy in measurement. The second section focuses on the experimental set-up and beam characterisation. The quality of the beam and it's alignment are significant contributors in obtaining accurate measurements. The last section will present the results obtained for the spectral dependence of $n_{2,eff}$ in graphene. The excitation spans 800-1050 nm, limited by the source (690-1050 nm) and the detectors (780-1800 nm). The results show a clear dependence of $n_{2,eff}$ on λ , with $n_{2,eff}$ increasing as the excitation tends to longer wavelengths.

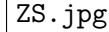


Figure 3.1: **Closed aperture (CA) transmittance and self-refraction illustrated for $\pm n_2$.** The closed aperture (CA) transmittance seen in the far-field for a medium that exhibits self-phase modulation and consequently self-refraction. A medium have an $n_2 > 0$ experiences self-focusing resulting in decreased transmittance (a) before focus, (b) no change at focus, and (c) increased transmittance after focus. Conversely in a medium having $n_2 < 0$, the self-defocusing effect causes (d) increased transmittance before focus, (e) no change at focus, and (f) decreased transmittance after focus. The peak to valley position is seperated by a factor of $\sim 1.7z_R$, where z_R is the Rayleigh length, for a third order nonlinearity. The baseline in the plots is a normalised power value for transmission in the linear regime.

3.2 Z-scan Technique

The investigation of higher order effects of any type brings with it many experimental complexities that make their investigation non-trivial. In nonlinear optics, the experimental measurement of the nonlinear index of refraction and nonlinear absorption may garner a similar perception in their realisability. However, in 1989 Sheik-bahae *et al.* [42] reported an experimentally facile single-beam method to measure the real and imaginary components of the third-order susceptibility with high sensitivity. This method is referred to as the Z-scan technique. The technique is based on the correlation of phase distortion and amplitude distortion during beam propagation through a nonlinear medium. Both nonlinear refraction and absorption can be probed by observing the transmittance in the far-field with a closed aperture (CA) and open aperture (OA) configuration, respectively. This chapter will provide a detailed outline of the theoretical and experimental aspects of the Z-scan method. Since this thesis focuses on nonlinear refraction, the derivation of the analytical theory, basis of experimental implementation, and additional details will focus around the CA measurement. Since the OA measurement is a necessary complementary measurement (i.e. for the normalisation of absorption effects in the CA profile), it will be considered only in experiment and not delved into in detail. In order to gain a more intuitive sense of how the self-refraction shown in Figure 2.3 is probed by the Z-scan method and can be extracted using the formulation derived in this section. Figure 3.1 illustrates the relative change in the CA transmittance profile as the sample scans across the focal plane of the beam.

3.2.1 Experimental Sources of Inaccuracy

The relative experimental simplicity of the Z-scan technique is contrasted by the strict control of certain parameters that must be exercised to obtain reliable and accurate measurements [43]. These parameters have implications on several assumptions of the analysis, and will be elucidated upon below.

Laser Beam Profile

With a nonlinear optical phenomenon where the observable effect of refraction is related to the magnitude of the incident intensity, it becomes imperative to consider the intensity distribution of the beam upon the sample. This is particularly important for the Z-scan, as the measurement relies on the sample induced distortions in the beam profile to characterise the nonlinearity, which necessitates the characterisation of the initial beam. In the analysis presented by Sheik-bahae *et al.* in their original paper, the profile is assumed to be a TEM₀₀ Gaussian beam, which provides a complete description of the intensity distribution of the beam when beam waist size, on-axis irradiance at focal point and ideality of the beam are considered. Several studies have been conducted to analyse the effects of non-Gaussian beams [44, 45], such as Lorentzian, parabolic and top-hat. An elliptical beam is a common output profile in many lasers, therefore the thin medium theory analysis for elliptical Gaussian beams presented by Mian *et al.* [46] is a very practical tool to ensure the accuracy in data analysis. An interesting observation that was made in this study was that under certain conditions of ellipticity, an additional peak appears in the Z-scan profile. A non-Gaussian beam can be characterised in terms of the M^2 parameter. The M^2 value is effectively the ratio of the divergence of the beam to the divergence of a Gaussian beam of the same waist size [47]. A Gaussian beam has the $M^2=1$, while all other profiles have $M^2 > 1$. The M^2 can be related to the beam divergence half-angle, θ , by the following relation:

$$\theta = M^2 \frac{\lambda}{\pi w_0} \quad (3.1)$$

Experimentally this quantity can be measured by scanning a beam profiler along the optic axis and measuring the beam radius at the focal plane to obtain the waist size. Following that, the beam radii will be measured at various distances away from the focal plane to accurately obtain the divergence angle of the beam. The divergence half-angle can simply be obtained geometrically through the relation:

$$\theta = \frac{w_2 - w_1}{z_2 - z_1} \quad (3.2)$$

where $w_{1(2)}$ is the radii at position $z_{1(2)}$. The M^2 is decomposed to its M_x^2 and M_y^2 components, along with θ_x and θ_y , to characterise a non-circular beam. Modelling studies [48] have been performed to determine the relationship between the M^2 value and the transmission (T) value. Several different types of non-ideal Gaussian beams were generated, close to what is seen in the laboratory, and the effects of the nonlinear medium were incorporated to generate data sets for both open and

closed aperture Z-scans. Two overarching trends were observed: (1) The scatter in the T increases with increasing M^2 ; (2) the value of T increases with increasing M^2 . The precise nature of the deviations depends on the particulars of the irregularities in the beam profile. However, this provides us with a good idea about the nature of the expected deviations when M^2 is far from ideal.

Temporal Characteristics of the Laser Pulse

Due to the intensity dependent nature of nonlinear optical effects, high laser powers are required to probe them. To this effect pulsed laser are employed which are capable of delivering extremely high peak energies. The temporal characteristics of the laser include the frequency and the pulse width which become important parameters as it pertains to the photophysical dynamics of the system. When the response time of the nonlinearity is much shorter than the laser pulse width, the nonlinear effect can be assumed to depend on the instantaneous irradiance in the sample. When the nonlinear response time is much longer than the laser pulse width, then the effects can be assumed to be fluence-dependent rather than irradiance dependent and a time integration must be performed as done in Eq. (A.73) in section A.3. This adds another layer of complexity to the analysis as the effects become dependent on temporal parameters.

Power Fluctuations

The Z-scan technique is based in analysing the medium induced distortions in the beam profile. Therefore, any external sources of distortion like those seen from fluctuations in laser output power, can prove detrimental to the accuracy of the experiment because the finer details of the curves are lost to noise. A common means of compensating for these fluctuations is to divide the signal of the far-field detector by the reference detector. This produces a much cleaner Z-scan profile as it effectively nullifies the effects of source fluctuations. However, this correction can be inadequate if the power varies by more than a few percent. Another method of obtaining a cleaner data set is only record a data point when the power falls within a well-defined limit. In general, the initial method proves sufficient.

Aperture Size

The importance of the aperture size is obvious, as the size directly correlates to the degree of isolation of the on-axis irradiance, where the medium induced distortion is most evident. In experiment, the far-field aperture is generally a pinhole. The distinction between aperture and pinhole in this context pertains to a particular assumption in the analysis which assumes that the far-field aperture is infinitesimally small, allowing an infinitesimal amount of transmission. In reality, the aperture is finite and with a finite linear transmission, which must be corrected for to obtain an accurate measurement. Qualitatively, the aperture is said to reach the infinitesimal limit when the transmission features become independent of the size, or no changes are seen in transmission if the aperture is translated in the x - or y -direction by one to two aperture diameters. A factor of

$(1 - S)^{0.268}$ can be multiplied to the ΔT relation as a means to account for a finite aperture. S is the linear transmittance of the aperture of the Gaussian beam and is given by:

$$S = 1 - e^{\frac{-2r_a^2}{w(z_1)^2}} \quad (3.3)$$

where r_a is the radius of the finite aperture and $w(z_1)$ is the waist size at the aperture plane.

Aperture Alignment

When the goal is to measure nonlinear refraction, a pinhole or aperture is placed in front of the far-field detector as a means to isolate the nonlinearity induced distortions. With these distortions being most prominent on the optical axis where the intensity of the impinging Gaussian beam is the largest, the alignment of the aperture is an important experimental factor. Since the irradiance on the optical axis is enhanced, the irradiance in the wings is reduced, so misalignment will produce a skewed transmittance profile in the far-field. The effects of misalignment are investigated by Hermann and Chapple [49]. They derived an expression to model the effects of misalignment where a misalignment parameter, ρ , is defined to be the radial displacement normalised by the beam size at the observation plane. For ΔT to agree with the on-axis result with 1%, ρ must be less than 0.1. Experimentally, we obtain the best alignment by mounting the aperture on an x- and y-direction translation stage to optimize for largest transmittance in the linear regime. For a Gaussian-shaped beam, $\rho = 0.1$ corresponds to a 2% drop in pinhole transmission. If the linear transmission is reduced by 5%, the error in ΔT is 3%. This illustrates the importance of obtaining the best alignment if error is to be minimised. In addition to that, practical alignment can be difficult if the beam profile is asymmetric, as we associate maximum linear transmittance with on-axis alignment, making this a non-trivial exercise.

Aperture-Waist Distance

Due to the fact that the Z-scan experiment relates nonlinearity induced spatial distortions in the field to nonlinear refraction via change in transmittance in the far field, the distance, z_1 , from the beam waist to the far field detector becomes an important parameter. This distance is ideally approaches infinity, but practically it is a finite values. The effect of having a finite distance on the differential transmittance (ΔT) can be obtained by differentiating Eq. (A.69) with respect to z . In doing so we obtain the formula:

$$\frac{\Delta T(z_1)}{\Delta T(\infty)} \approx 1 + \frac{0.9}{0.8 + \left(\frac{z_1}{z_R}\right)^2} \quad (3.4)$$

where the change in ΔT is normalised by ΔT when z_1 equals to infinity. Qualitatively, as expected we observe that as we increase the distance into the far-field the function approaches the infinity limit. However, by simply inserting some trial distances for z_1 , we see that for a distance of 10 Rayleigh length ΔT is 1% greater than the value at infinite distance and for 20 Rayleigh lengths the

variation decreases to 0.2%. Therefore, in experiment 10 Rayleigh lengths is a reasonable minimum approximation for the distance that can be considered far-field. In addition to that, a correction can further be made using Eq. (3.4).

Sample Thickness

The analytical simplicity of the Z-scan is primarily stems from the "thin film" approximation, which assumes that the path length inside the sample is not large enough to cause distortion in the beam shape, but only presents the effects of in-medium propagation as a phase shift. It intuitively follows that this approximation will break down after a certain sample thickness. The criterion for validity of this approximation requires that the sample length L is much shorter than the Rayleigh length (z_R). As seen previously, the Rayleigh length factors prominently in the optics and the subsequent analysis of the measurement. Since this parameter is a measure of the distance scale over which the beam profile changes, it imposes a requirement on the length of the sample with the condition: $L \ll z_R/|\Delta\Phi_0|$ when $|\Delta\Phi_0| > 1$. Experimentally, it is easy to increase (decrease) the Rayleigh length by increasing (decreasing) the initial beam diameter incident on the focusing optic or using a longer (shorter) focal length lens. However, for very thick samples, this may not be practical.

Defects

Since the techniques relies on relating wave distortion to nonlinear refraction, any other mechanisms contributing to these distortions will work to obscure the nonlinear effect. This can occur through physical imperfections in the sample, or beam steering caused when the sample sits non-perpendicular to the beam as it is scanned and the beam will be moved away from the axis of the aperture.

Etalon Effects

With samples that have not been anti-reflection coated, there is a strong possibility that they form low-finesse Fabry-Perot etalons. Etalon refers to an optical device that contains two parallel mirrors. It is intuitive to see that with the formation of this psuedo-cavity there will be a certain modulation in the transmission that is seen by the FF detector. The degree of transmission change depends on the refractive index of the medium and its optical length. In order to avoid the formation of an etalon, an anti-reflection coating must be applied to reduce the internal reflection of the surfaces. In addition to transmission variations, the reflections do vary with irradiance, which will indefinitely skew the measurement of nonlinearity. Studies have been performed to observe the effects of reflection in a self-focusing medium [50]. For low nonlinear phase shifts ($\Delta\Phi_0 \approx 0.01$), the reflectance is seen to enhance the nonlinear phase shift by a factor, when the cavity is in resonance. For a low reflectance and moderate phase shift ($R = 0.065, \Delta\Phi_0 = 0.5$), the nonlinear phase shift can push the cavity away from resonance, eradicating the symmetry in the Z-scan profile. For moderate reflectance and large phase shifts ($R \approx 0.5, \Delta\Phi_0 = \pi$), strong feedback effects such as

optical switching and bistability can occur. To avoid all etalon effects, it is best to at least coat the rear surface of the samples to reduce the formation of a cavity, especially in high refractive index materials.

3.3 Z-scan Experimental Set-up

The experimental set-up used in this experiment is similar to the original design as shown by Sheik-bahae *et al.* [42] in their original paper. In their layout, a reference detector was placed prior to the focusing lens to normalise for laser fluctuations. In their case the CS₂ samples used displayed negligible nonlinear and/or saturable absorption so normalising their CA scan by the OA scan was not required. In a subsequent article, Sheik-bahae [51] presented a more detailed analysis of both nonlinear refraction and absorption, utilising the OA configuration.

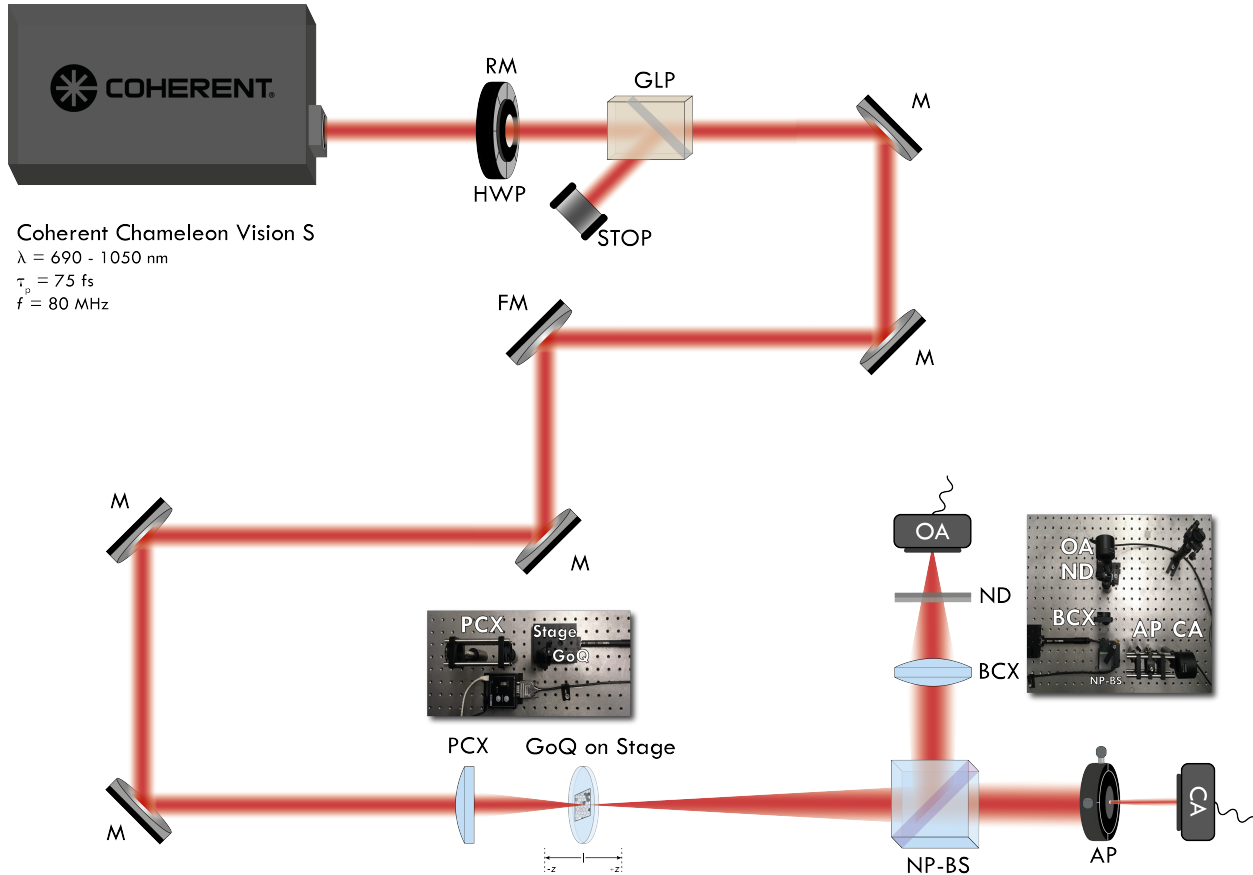


Figure 3.2: **Optical set-up used for the Z-scan measurement.** The path of the laser begins at the laser (Coherent) and is allowed to pass through a high power variable attenuator comprised of a half-wave plate (HWP) and polariser (GLP). The beam is guided to the first focusing lens (PCX) where the beam is focused and the sample (GoQ on Stage) is translated through the focal plane. The transmitted beam is split into two with a 50:50 beam splitter (NP-BS) into the open aperture detector (OA), and the closed aperture detector (CA) through the pinhole. The complete reference to the schematic is provided in Table B.1.

To optimise the data acquisition process, the closed and open aperture data is acquired simultaneously by splitting the far-field signal in half and directing them into their respective detectors. Since the absorption signal needn't be normalised by power fluctuations, the OA scan will allow

normalisation for laser fluctuations and the usual absorption effects.

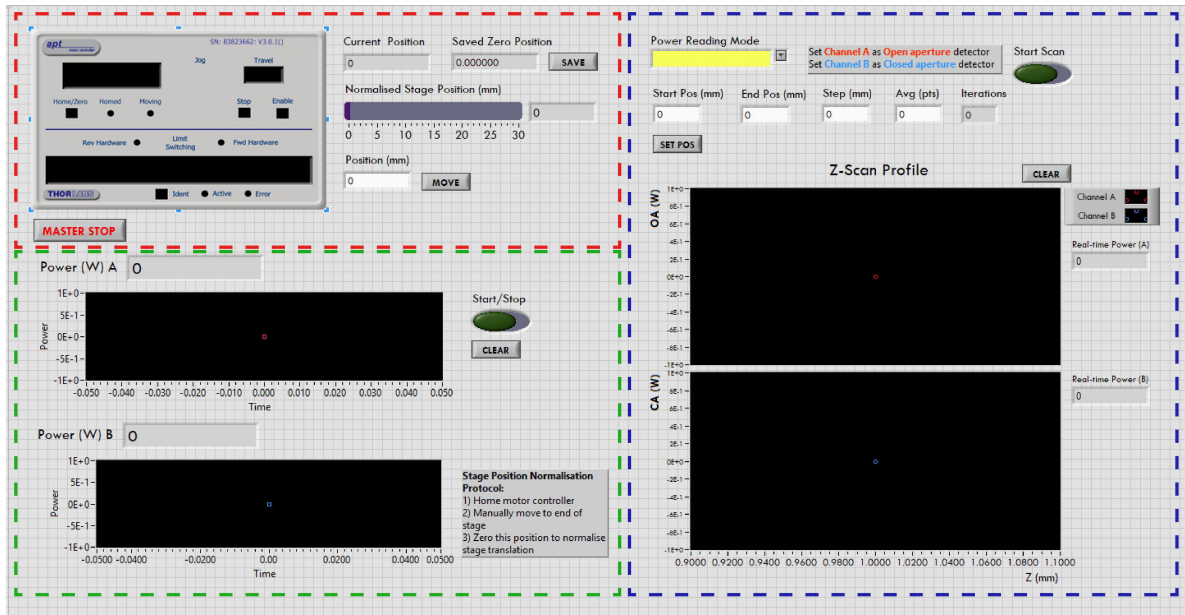


Figure 3.3: **LABVIEW program used for data acquisition.** LABVIEW program used for data acquisition displaying modules to control translation stage, acquisition of continuous power values, and Z-scan measurement.

The experimental Z-scan set-up is schematically illustrated in Figure 3.2. Each component is marked by an identifier (i.e. PCX) which can be referenced to Table B.1 for further detail. The source is a high power ultrafast tunable laser operating in the 690-1050 nm regime with a 75 fs pulse width, as advertised by the manufacturer, and a 80 MHz repetition rate. The laser power does not emit at equal power over the wavelength range, this factor is a limitation to the power that can be accessed for measurement. The power of the laser is controlled by a standard high power variable attenuator set-up comprising of a zero-order half wave-plate mounted on a manual rotation mount, directed through a polariser. The zero-order half wave plate is designed to create a phase shift that is exactly one quarter or one half of a wave, and offers relatively lower temperature and wavelength dependence. With rotation of the wave plate the transmitted light through the polariser is modulated with the rejected polarisation being dumped into the beam stop (STOP). The beam is then directed to the sample by silver mirrors (M) and in particular a flip mirror (FM). The beam is focused through a plano-convex lens (PCX) of a focal length of 70 mm. In the latter two experiments, i.e. pulse-width dependence and pump-probe integrated Z-scan, the focusing lens is changed to a 75 mm doublet lens to reduce aberrations. The beam is focused down and the sample mounter on a stage (GoQ on Stage) is translated through the focal plane. The transmitted beam is split in two using a 50:50 non-polarising beam splitter (NP-BS). The perpendicular arm collects the entire beam and focuses it through a bi-convex lens (BCX) and directs it into the open aperture (OA) detector. An optical density filter is placed to attenuate the beam to disallow detector saturation. The parallel arm directs the beam through a pinhole (AP) mounted on an

x-,y-direction translational stage and into the CA detector. The detectors were connected to the power meter via RS-232 inputs and the power meter was interfaced with the computer using via USB.

The data acquisition was accomplished using a custom LABVIEW program. A screen shot of the program is shown in Figure 3.3. The module serves three primary functions: (i) control of the sample translation stage via a Thorlabs provided controller (top-left), (ii) interface with the power meter to obtain continuous power values from both channels as a function of time (bottom-left), and (ii) perform the Z-scan measurement using the input parameters for relative start and stop positions, and translation resolution (right).

3.3.1 Beam Characterisation

Characterising the incident beam is an imperative aspect of the Z-scan measurement. As mentioned previously, a key assumption of the Z-scan technique is the use of a fundamental mode Gaussian beam which ensures that the experimental data and the consequent analysis are as accurate as possible. The pitfalls of deviation from this ideal profile have also been addressed in section 3.2.1. The beam profile is measured using the Thorlabs Beam Profiler (BP209-VIS [52]) which uses a dual scanning slit method to generate a beam profile. A photodetector is used to record data as two orthogonal slits of the same width are scanned across the cross section of an incident laser beam. To determine a beam's quality and spatial characteristics, the light is sampled by the detector in two directions, and the overall power distribution is calculated. From the resulting power distributions in the X and Y directions, beam characteristics are analysed. The beam profiler can measure a minimum beam diameter of 2.5 μm and a maximum diameter of 9 mm. All measurements are obtained using a 13.5% ($1/e^2$) clip width, which is the distance at which the intensity of the beam is 0.135 of the maximum intensity.

As seen in Figure 3.2, the beam goes through a high power variable attenuator set-up upon exit and is directed into the focusing lens (PCX) using a series of silver mirrors. The beam profiles shown in Figure 3.4 are taken at 1050 nm without any optics in the path and are 45 cm apart at PCX (Figure 3.4a) and at the CA detector (Figure 3.4b). The beam at PCX is measured to be 2.465 mm and the beam at CA is measured to be 2.743 mm, giving a divergence of 61.77 mrad. In order to obtain the most ideal beam profile and obtain an appropriate focusing, a 3.5 cm plano-convex and a 60 cm plano-convex lens were used as beam expander and collimator. The beam was expanded to 3.455 mm. However, during initial alignment attempts, it became clear that it would be very difficult to get the lens to the perfectly perpendicular to the incident beam and to each other. The lack of this perpendicularity will result in the beam tilting and gaining an off-axis propagation, which makes precise alignment through multiple pinholes impossible. For the CA measurement, it is of utmost importance to precisely probe the on-axis transmittance to obtain the most accurate results. Considering this engineering trade-off between accuracy of the results and less than ideal beam focus characteristics, it was appropriate to maximise accuracy of results. Therefore, the beam expander configuration was removed and the raw beam from the laser was used. To provide minor

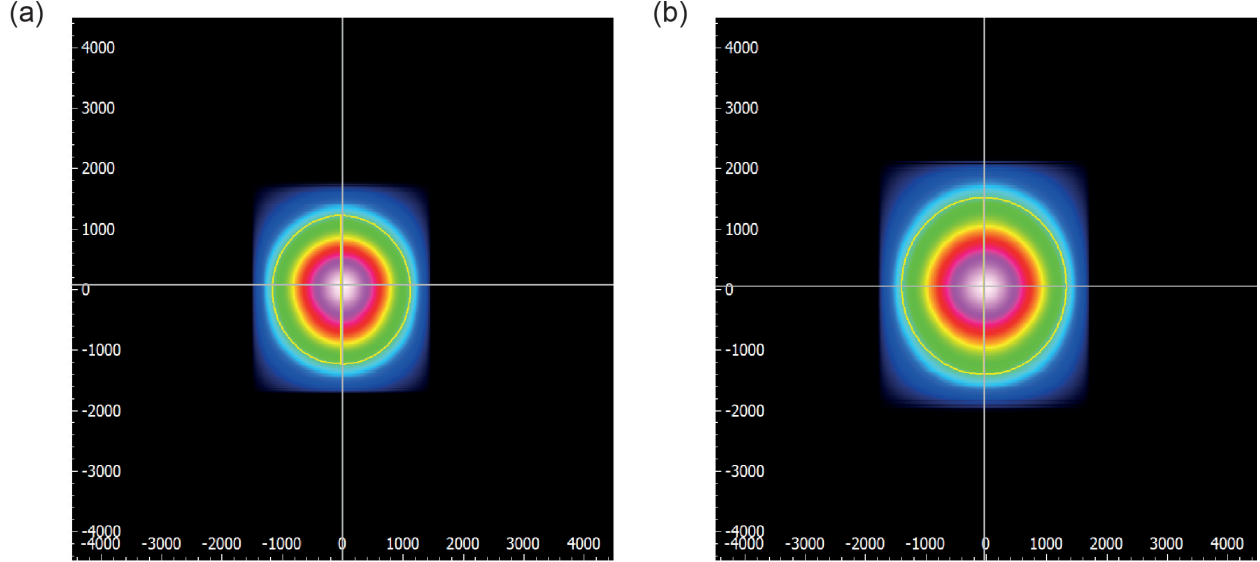


Figure 3.4: **Beam profiles of the beam at 1050 nm at the locations of the focusing lens and far-field detector.** Raw beam profiles at 1050 nm as measured 45 cm apart by a scanning slit beam profile at (a) the location of the focusing lens (PCX) with a diameter of 2.465 mm and (b) at the CA detector with a diameter of 2.743 mm

spatial filtering an iris was added prior to PCX.

The properties of the beam at the focal plane along with the corresponding Rayleigh length are important parameters that are required for the analysis. The relationships between the focusing optic, beam waist, wavelength and Rayleigh length are:

$$w_0 = \frac{2\lambda F}{\pi D} \quad (3.5)$$

$$z_R = \frac{\pi w_0^2}{\lambda} \quad (3.6)$$

where w_0 is the beam radius at the focal point, F is the focal length of the of focusing optic, D is the diameter of the incoming beam before it is focused, z_R is the Rayleigh length (see Appendix A.1), and λ is the excitation wavelength. The dependence of these properties of the beam are relatively intuitive as the lens will not focus every wavelength in a similar manner due to dispersion effects in the lens.

The Thorlabs Beam Profiler was used to scan the beam around the focal plane to find the smallest spot size along the translation axis. Since the experiment involves running the Z-scan with a range of wavelengths, the beam waist measurement was performed at the chosen excitation wavelengths. The beam measurement values are plotted in Figure 3.5. In addition to that, theoretical values calculated using Eq. (3.5-3.6) are also provided for comparison. By looking at the theoretical and experimental values, we do see that in practice we rarely achieve a perfect match to the theoretical limit. In theory, the degree to which a beam of light can be focused down, assuming a

perfectly collimated incoming beam, is imposed by the diffraction limit. Diffraction is a fundamental phenomenon that occurs due to the wave nature of light and depends on the wavelength and the diameter of the optic. Apart from this theoretical limit, we experience dispersion, aberrations and other losses which contribute to less than ideal focus. We know that our beam has a divergence of 61 mrad, as calculated previously, and focusing a slowly diverging beam will contribute to the beam waist being larger than calculated with the same focusing lens. The quality of the beam is relatively unaffected but the beam does not get as tightly focused, which is not problematic if we use the experimental beam waist to calculate the on-axis irradiance.

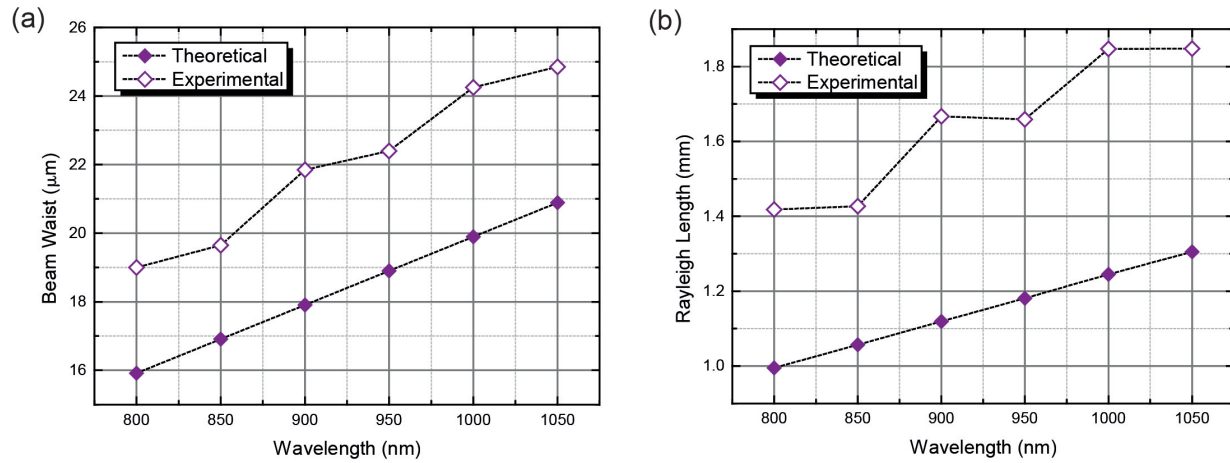


Figure 3.5: **Beam waist and Rayleigh length.** Theoretical and experimentally measured (a) beam waist and corresponding (b) Rayleigh length at excitation wavelengths

3.4 Spectrally-dependent Z-scan measurement

The initial part of the experiments focuses on extracting the nonlinear index of refraction for graphene over the excitation range 800-1050 nm. The range is limited by the source (690-1050 nm) and the detectors (780-1800 nm). This section focuses on presenting and discussing the results from the spectrally-dependent Z-scan measurement of graphene. The motivation behind this experiment is two-fold; firstly, the discrepancy in sign and value for the nonlinear refractive index has been the subject of debate for a few years (refer to Table 2.2), with values spanning six orders of magnitude, therefore, this measurement will address effect of excitation wavelength on the nonlinear refractive index to gain a fundamental understanding of the processes involved. Secondly, the cataloguing of these values over a range of wavelengths provides a reference for $n_{2,eff}$, when designing larger graphene integrated systems where the effective nonlinear refraction is required.

The CVD fabricated graphene samples ($1 \times 1 \text{ cm}^2$) transferred onto quartz were purchased from ACS Materials. In order to verify the quality and monolayer nature of the sample, we perform Raman spectroscopy, shown in Figure 3.6. The G-band, 2D-band and D-band peaks appear at 1576 cm^{-1} , 2661 cm^{-1} and 1328 cm^{-1} , respectively. The relative intensities and widths of the G and 2D peaks confirm that the sample is single layer.

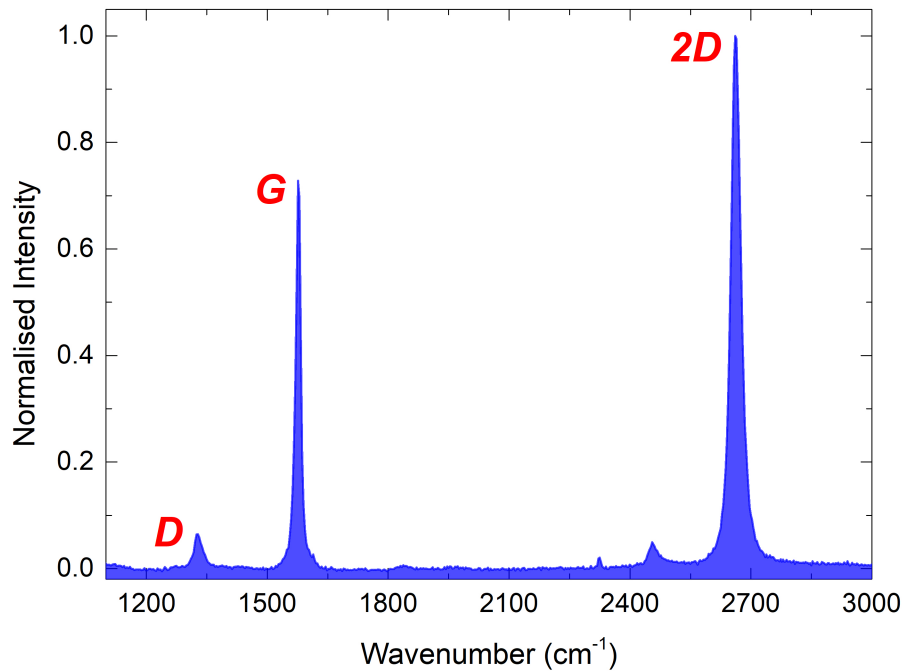


Figure 3.6: **Graphene characterisation.** Raman spectra of graphene sample with the G-band, 2D-band and D-band peaks appearing at 1576 cm^{-1} , 2661 cm^{-1} and 1328 cm^{-1} , confirming monolayer sample.

With the phenomenon under observation being intensity dependent, it is important to consider a normalisation between wavelengths. This is done by considering the on-axis irradiance and making sure that at every wavelength the on-axis irradiance is close to being the same. With irradiance we have equivalent energy impinging on a unit area, while the number of photons will differ, the order of magnitude remains the same. With knowledge of the beam waist value for every wavelength, the area is used to back calculate the average power required to produce the desired on-axis irradiance. To maintain this irradiance normalisation, the maximum usable power is limited by the wavelength with lowest maximum power (1050 nm). The measurement is performed with 50 nm increments in wavelength. The general scheme of data acquisition is to perform the measurement at a certain power and at a particular spot multiple times, then moving onto another spot for a few more acquisitions. After this, the power, if allowed, is increased to perform a similar acquisition scheme. Scanning repeatedly in multiple spots assured that any anomalous data sets are averaged out and effects of damage, if any, are also accounted for.

As permitted by the source, the measurement is performed using on-axis irradiances of $\sim 1.6, 2.5\text{-}3,$ and $4\text{-}4.9$ GW/cm². At 1050 nm, only the lowest irradiance is utilised; at 1000 nm, the two lowest irradiances are used; and at 950-800 nm, all three irradiances are used. Once the experimental data is obtained, it is fit to the theoretical model derived in section A.3. To be thorough with the fitting scheme, the data is simultaneously fit with both Eq. (A.69) and (A.72). Eq. (A.69) is fit using the nonlinear least squares algorithm, which allowed for more of a global data fit, while Eq. (A.72) allowed for manual fitting using the peak-valley separation. In addition to that, some data filtering is also performed for when the signal is noisy. Due to the fact that we probe the far visible wavelengths, without isolation from ambient light there is increased noise in the data. An outlier removal function in ORIGIN Pro. is used to reduce the noisier data points without affecting the data set.

Figure 3.7 provides the Z-scan profiles for measurements performed at 950 nm. The figure shows plots for the Z-scan measurement containing the OA profile, absorption normalised CA (CA/OA) profile and the fit from which the $n_{2,eff}$ value is extracted. The data shown here is for measurements performed with on-axis irradiances of (a) 1.621 GW/cm², (b) 3.014 GW/cm², and (c) 4.862 GW/cm². The $n_{2,eff}$ extracted from this data is seen to range from 1.062 to 1.437×10^{-8} cm²/W. This reduction of $n_{2,eff}$ with increasing on-axis irradiance is well-known saturation induced effect.

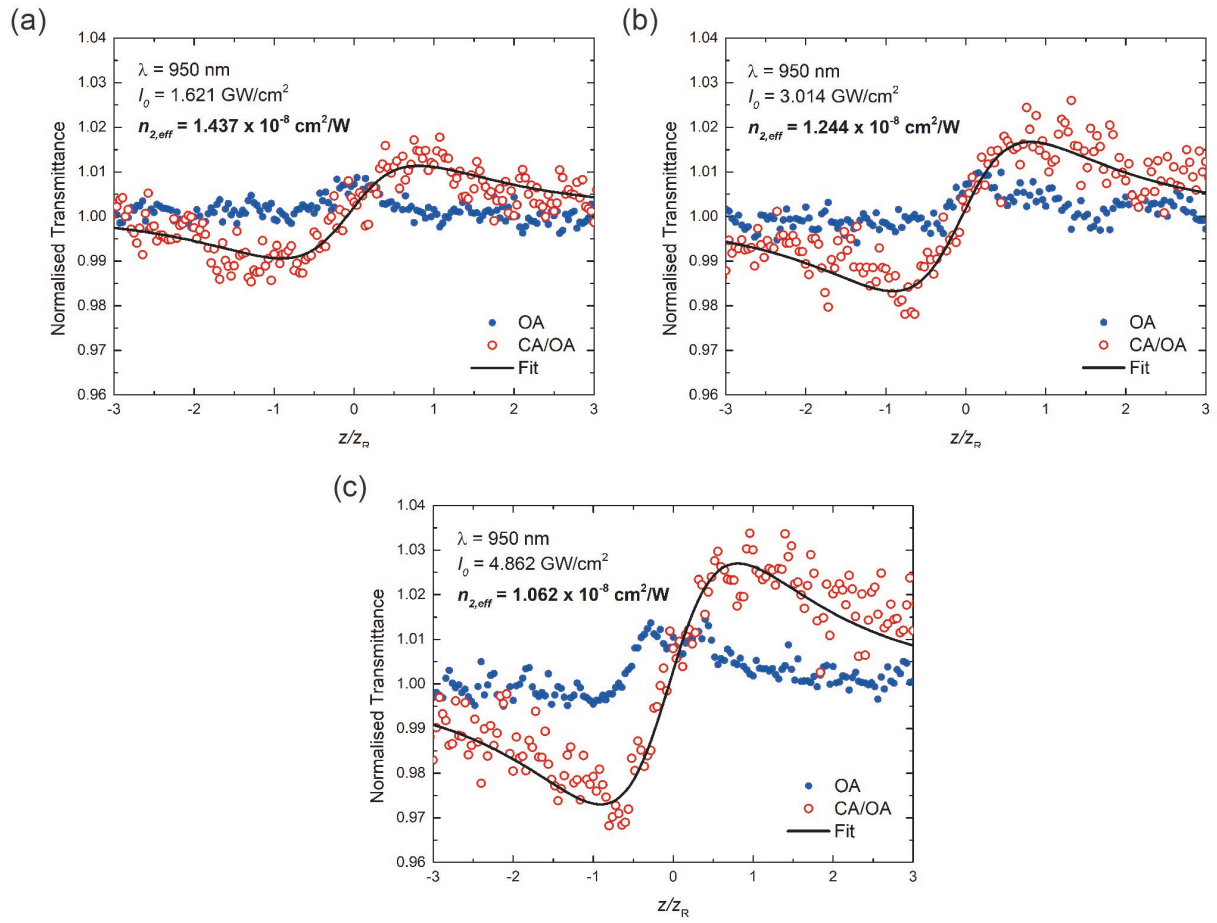


Figure 3.7: **Z-scan profiles at 950 nm.** Z-scan profiles performed at 950 nm with on-axis irradiances of (a) 1.621 GW/cm², (b) 3.014 GW/cm², and (c) 4.862 GW/cm². The decrease in $n_{2,eff}$ is attributed to a saturation induced effect.

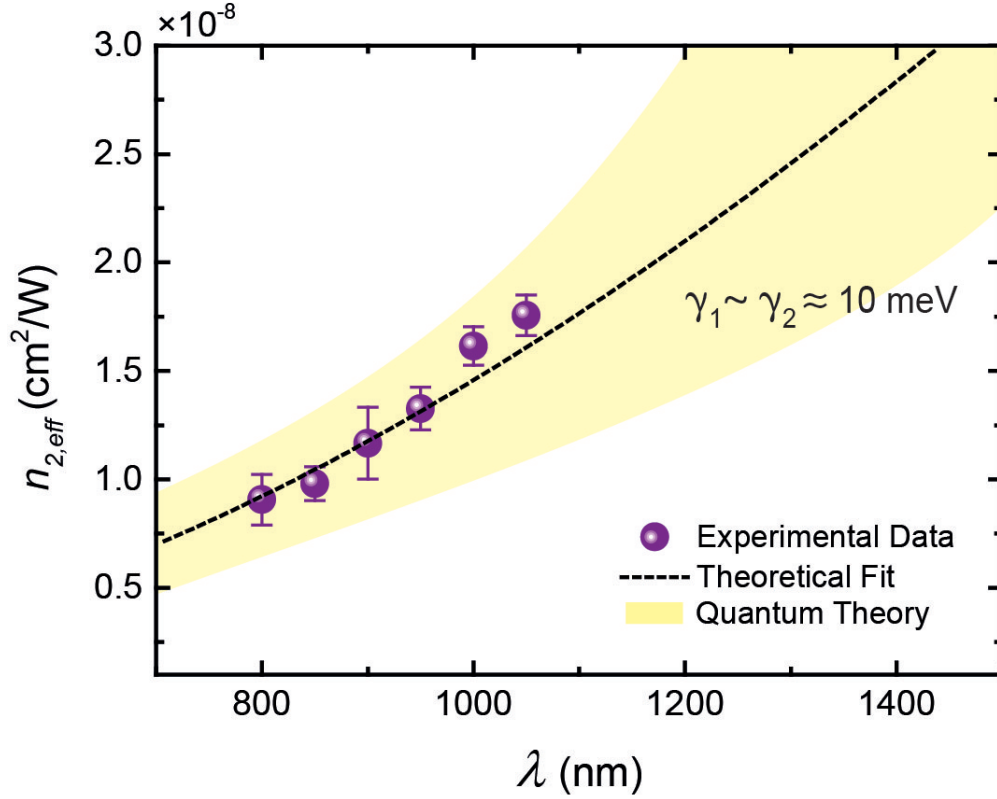


Figure 3.8: **Spectrally-dependent nonlinear refractive index.** Spectrally-dependent nonlinear refractive index spanning 800-1050 nm. The $n_{2,eff}$ values range from 9.065×10^{-9} - 1.757×10^{-8} cm 2 /W over this range with each point having error bars as the data has been averaged over multiple sets

The values for the nonlinear index of refraction, $n_{2,eff}$, are plotted as a function of wavelength in Figure 3.8, which will provide a visual about the relationship between the $n_{2,eff}$ and its dependence on the wavelength. The data at the mid-irradiance range are averaged and the standard deviation is determined to compile the plot. The value of $n_{2,eff}$ (cm 2 /W) is positive in this excitation regime. Sample Z-scan profiles measured from 800 to 1050 nm at 50 nm increments are presented in Figure 3.9. The measurements are conducted at approximately the same on-axis irradiance (~ 2.5 -3 GW/cm 2) over the wavelength range, except the lowest irradiance at 1050 nm is utilised due to the power limit of the laser. There is a large degree of noise for lower irradiances at shorter wavelengths. This is the cumulative nonlinear refractive response. The $n_{2,eff}$ is seen to have a dependence on the excitation wavelength, ranging from 9.065×10^{-8} to 1.757×10^{-8} cm 2 /W for a wavelength range of 800-1050 nm. Shorter wavelengths are observed to have a $n_{2,eff}$ value that is lower as compared to longer wavelengths, with approximately the same on-axis irradiance (W/cm 2).

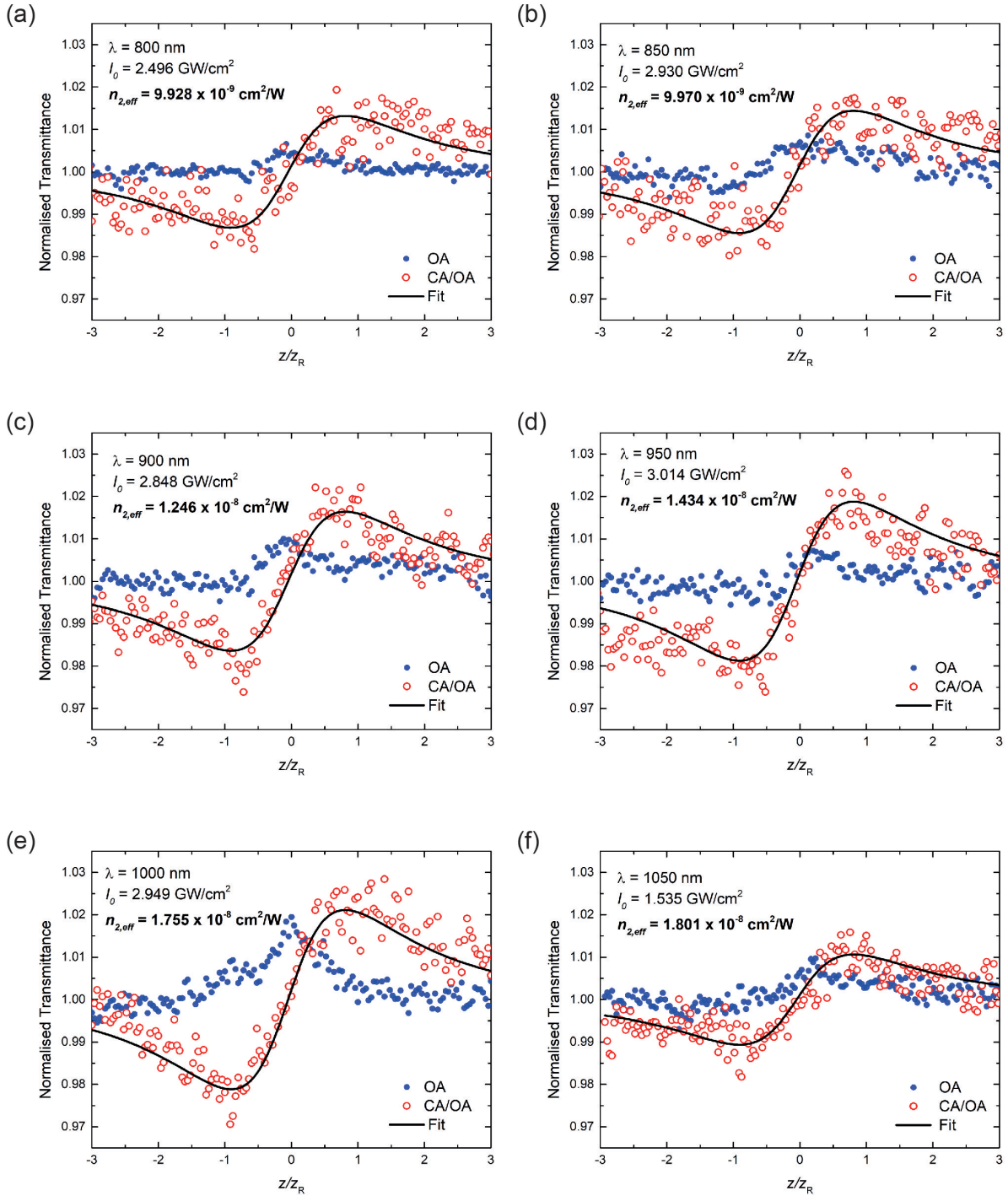


Figure 3.9: **Z-scan profiles at wavelengths spanning 800-1050 nm.** Z-scan profiles containing the OA, absorption normalised CA (CA/OA) and the fit. Plots (a-f) show the data and fits for excitation wavelengths of 800, 850, 900, 950, 1000 and 1050 nm, respectively. With the exception of 1050 nm, all data sets are taken at similar on-axis irradiances with the exact values and the corresponding $n_{2,eff}$ values also provided.

This dependence has been reported since the first measurements of n_2 in graphene were performed (refer to Section 2.3). It was explicitly derived by Hendry *et al.* [22] that n_2 had a λ^4 on the wavelength. However, a few reports after that have observed a power dependence but not with a power of 4. Fitting the data shown in Figure 3.9 to a power model ($n_2 = a * \lambda^b$), a value of $b = 2.13$ is obtained. It is clear that within a range of error the experimental results follow the quadratic theoretical model rather than the quartic. Through rigorous calculation Semnani *et al.* [14] developed a cohesive quantum theory to explain nonlinear optical phenomenon in graphene. To this end, they found that the dependence is quadratic in wavelength (λ^2), also shown in Figure 3.8.

It is noted that $n_{2,eff}$ exhibits negligible dependence on the Fermi level for a low-doped graphene monolayer. In our case $n_{2,eff}$ is dominated by contributions from interband transitions and the most relevant transitions occur at the zero detuning region where $\omega = 2|\mathbf{k}|v_F$. Detuning is defined as $\Delta_k = \hbar\omega - \mathcal{E}_{cv}$, where ω is the frequency of the excitation photon and \mathcal{E}_{cv} is the energy of the transition, see Figure 3.10a. The theoretical model employed in our theory use semiconductor Bloch equations (SBEs) to describe the cooperative intra-interband dynamics of the population difference $\mathcal{N}(\mathbf{k}, t)$ (between the valence and conduction bands) and the polarisation (coherence) $\mathcal{P}(\mathbf{k}, t)$ for the Bloch state \mathbf{k} . The phenomenological relaxation coefficients, $\gamma_{1/2}$, account for the collective broadening effects for the population and coherence decay, respectively. Under our theory, the electromagnetic coupling for normal illumination is defined by $\hat{\Phi}_k = \frac{\mathbf{E}\hat{\phi}_k}{\hbar k}$, where \mathbf{E} is the electric field and the unit vector $\hat{\phi}_k$ is defined as $\hat{\phi}_k = \hat{z} \times \mathbf{k}/k$, shown in Figure 3.10a.

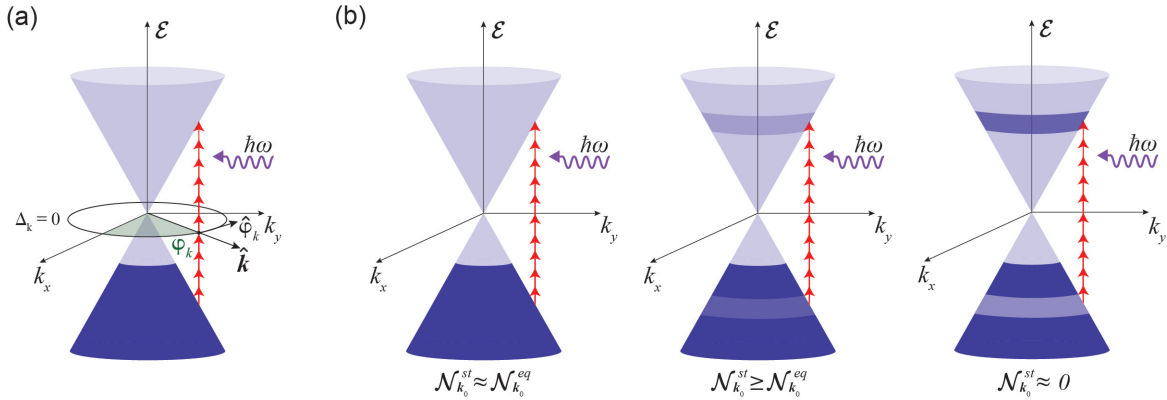


Figure 3.10: **Carrier relaxation in graphene leading to Kerr-type nonlinearity.** (a) Band structure of graphene showing the excitation pulse with energy $\hbar\omega$, the zero detuning circle $\Delta_k = 0$, and $\hat{\phi}_k$ is a vector in reciprocal space, (b) the evolution of the steady state population ($\mathcal{N}_{\mathbf{k}}^{st}$) and the equilibrium population ($\mathcal{N}_{\mathbf{k}}^{eq}$) difference upon intense illumination which disturbs the $\mathcal{N}_{\mathbf{k}}^{st}$ leading to the observation of a Kerr-type nonlinearity in graphene. The colour bands represent relative population differences in the schematic.

The nonlinear optical absorption has multiple origins namely bleaching effects culminating in saturation, and two photon absorption. Since the graphene sample used in our experiment is low-doped

(i.e $\mu \ll \hbar\omega$), absorption bleaching due to optically induced Pauli-blocking plays the leading role. Bleaching refers to the phenomena where the system cannot be excited anymore due to the available states filling up. This is the same idea as Pauli blocking. This assumption is supported by observation of the absorption drops upon high optical irradiance, refer to the OA trace in Figure 3.9. Furthermore, since the Fermi energy level is small compared to the energy of the photons, it naturally follows that Pauli blocking around zero detuning region is widely demolished. Under high intensity illumination in a Kerr-type material, the charged carriers undergo ultrafast Rabi oscillations, much faster than their relaxation rate. As a consequence the steady state population, $\mathcal{N}_{\mathbf{k}}^{st}$, is significantly modified by light, disturbing the distribution at equilibrium, $\mathcal{N}_{\mathbf{k}}^{eq}$. The origin of the Kerr-type nonlinearity is the optically induced change to the steady-state population difference. The relaxation dynamics as the population difference evolves is schematically shown in Figure 3.10b. Before saturation takes place, the nonlinear contribution of the field to the population difference around the zero detuning region is a quadratic function of the field magnitude, $\mathcal{N}_{\mathbf{k}}^{st} - \mathcal{N}_{\mathbf{k}}^{eq} \approx -\frac{1}{\gamma_1\gamma_2}\mathcal{N}_{\mathbf{k}}^{eq}|\phi_{\mathbf{k}}|^2$. The induced nonlinear current oscillating at the frequency ω is then given by $\mathbf{J}_{NL} = \sum_{\mathbf{k}}(\mathcal{N}_{\mathbf{k}}^{st} - \mathcal{N}_{\mathbf{k}}^{eq})\phi_{\mathbf{k}}\mathcal{L}_{\mathbf{k}}(\omega)$, where the Lorentzian $\mathcal{L}_{\mathbf{k}}(\omega) \triangleq 1/(\gamma_2 + i\Delta_{\mathbf{k}})$ accounts for the interband transitions. For a small enough γ_2 , the Kerr-type nonlinear induced current is given by

$$\mathbf{J}_{NL} = \chi^{(3)}(\omega, \omega, -\omega)|\mathbf{E}|^2\mathbf{E} \sim \beta \frac{e^2}{\hbar} g_s g_v D \frac{1}{\gamma_1\gamma_2} \left| \frac{e}{\hbar k} \mathbf{E} \right|^2 \mathcal{N}_{\mathbf{k}}^{eq} |_{\Delta_{\mathbf{k}}=0} \quad (3.7)$$

where g_s and g_v are the spin and valley degeneracy factors, respectively, $D = 1/4\pi^2$ is the density of states, and $\beta \sim \pi$ is a dimensionless quantity that arises from angular integration around the Dirac cone. Due to low doping, $\mathcal{N}_{\mathbf{k}}^{eq} \approx 1$ over the zero detuning circle. The quadratic wavelength dependence of the Kerr coefficient is a direct consequence of the linear energy-momentum dispersion of the Dirac quasiparticles in graphene, simplistically given as $n_2 \sim \frac{1}{\epsilon_0 c} \chi^{(3)}(\omega, \omega, -\omega) \propto \lambda^2$.

Chapter 4

Pulse-width dependence of the effective Kerr coefficient of Graphene

4.1 Introduction

In the previous chapter, the effect of varying the wavelength of the excitation on the observed $n_{2,eff}$ is probed. It naturally follows to investigate the temporal counter-part of this measurement. To this end, in this chapter the dependence of $n_{2,eff}$ on the pulse-width of the excitation source is investigated. The beam at 900 nm is stretched from 100 fs up to ~ 500 fs and the stretched beam is used as an input to the Z-scan set-up.

In general, there are several techniques to accomplish the stretching of laser pulses and are broadly classified into four categories; (a) optical pulse stretching using a configuration of optical elements that split the amplitude of the incident pulse, introducing optical delays between them, (b) pulse stretching by intracavity nonlinear materials, (c) electronic pulse stretching, and (d) pulse stretching by dispersion. Each technique finds application in niche applications due to the elements involved and their subsequent integration into optical or electronic systems. More importantly, there are limitations to the temporal stretching or expansion that can be achieved for certain systems. In the case of ultrashort pulses, pulse stretching by dispersion is generally used because the spectral bandwidth of the ultrashort pulses is very large. The dispersive pulse stretcher is a configuration of dispersive optical elements that introduce wavelength dependent optical delays to introduce frequency chirp for temporal stretching. The term *chirp* refers to the temporal arrangement of the frequency components of the laser pulse [53].

Frequency chirping via dispersion can be achieved with propagation through optical fibers, diffraction gratings or prisms. In a medium with positive dispersion, the higher frequency (shorter wavelengths) components of the pulse travel slower than the lower frequency (longer wavelengths) components and the pulse becomes positively-chirped or up-chirped. In a medium with negative dispersion, the converse effect is observed resulting in the pulse becoming negatively-chirped or down-chirped. Long propagation distances are required to disperse the beam sufficiently in optical

fibers. Diffraction gratings provide large stretching factors (>1000 times), but result in a huge loss in peak power in the reflection configuration. However, using gratings in transmission allows for the retention of peak powers with the same stretching factors. The prism-pair method provides for robust stretching of high power pulses, but is experimentally difficult to implement due to the need to have angular precision in the alignment of the beam as it goes through the prisms to ensure sufficient dispersion and recombination, resulting in no spatial chirp. In addition to that, the degree of stretching is governed by the separation distance of the prisms, which is limited by the available table space and adds to the difficulty of angular alignment over large distances. Given the knowledge and resources at the time, the pulse is temporally stretched using the prism-pair configuration. However, using gratings in transmission is objectively the better choice since it is experimentally easier to implement and allows for larger stretching factors and retention of power without the large separation distances.

This chapter is presented in a manner to first elucidate on the theory behind dispersion in the context of experimental implementation, followed by the details of the set-up to achieve the desired pulse-stretching. Considering the sensitivity of the alignment, it is imperative to characterise the stretched pulse to confirm that the beam has undergone the desired temporal modification. This is achieved through the use of a home-built autocorrelation set-up. A brief section is presented on the details of operation of this set-up followed by the characterisation results. The final section presents the results of pulse-width dependent Z -scan measurement which shows that $n_{2,eff}$ has clear dependence on the pulse-width of the excitation source.

4.2 Effect of Dispersion

In Appendix A.1, the Gaussian beam equation was derived (Eq. (A.54)). The equation is expanded to explicitly show the spatial components of the equation, while the temporal properties are confined within the leading term, $E(t)$. This section will elucidate on this leading term to derive the effect of dispersion on a Gaussian beam [54].

In time domain, the electric field of a Gaussian pulse is given by:

$$E(t) = \sqrt{A_t \exp^{-\ln 2 \left(\frac{2t}{\Delta t}\right)^2}} \exp^{-j(\omega_0 t + \theta(t))}$$

where A_t is the amplitude, ω_0 is the frequency, Δt is the pulse duration, and $\theta(t)$ determines the temporal relationship among the frequency components within the pulse envelope. Due to mathematical tedium of working in time domain when considering the effects of dispersion on the pulse, it is more convenient to consider the pulse in frequency domain via a Fourier transform. In order to determine the pulse duration after propagation through a dispersive material, it is necessary to solve a convolution integral when working in time domain. However, due to convolutions transforming to products in Fourier space, the problem is simplified when working in the frequency domain. Therefore, the electric field in frequency domain is given by:

$$E(\omega) = \sqrt{A_\omega \exp^{-\ln 2 \left(\frac{2(\omega - \omega_0)}{\Delta \omega}\right)^2}} \exp^{-j\phi_{pulse}(\omega - \omega_0)} \quad (4.1)$$

where Δt and $\Delta \omega$ are related through the uncertainty relation $\Delta \omega \Delta t = 4 \ln(2)$ [55], and the spectral phase, $\phi(\omega)$, describes the relationship between the frequency components within the pulse envelope. Both ω and $\Delta \omega$ denote angular frequencies which can be converted to linear frequency, ν , through the relation $\nu = \frac{\omega}{2\pi}$. Using this substitution, a parameter called the time-bandwidth product, $c_B = \Delta \nu \Delta t = \frac{2 \ln(2)}{\pi}$, is defined [56]. Since this parameter is the product of a pulse's width in the time and frequency domain, it sets a lower limit for the pulse duration, a limit imposed by the property of the Fourier transform. A term often used is *transform limited pulses*, this refers to how short the pulse duration can be given a spectral width. If a pulse is transform limited, it contains no chirp and therefore exhibits no effect of dispersion. For a Gaussian-shaped pulse $c_B \approx 0.44$, which is a minimum limit.

As an input pulse, $E_{in}(\omega)$, traverses through a dispersive medium, the phase added by the material is simply the product of the input field and the transfer function of the material. Therefore, the output pulse is given by:

$$E_{out}(\omega) = E_{in}(\omega) R(\omega) \exp^{-j\phi_{mat}(\omega - \omega_0)}$$

where $\phi_{mat}(\omega - \omega_0)$ is the spectral phase added by the material and $R(\omega)$ is an amplitude scaling factor which is approximated as 1 for a transparent medium. The spectral phase can be expressed

as a Taylor expansion around the carrier frequency, ω_0 , of the pulse as such:

$$\phi(\omega - \omega_0) = \phi_0 + \phi_1 \cdot (\omega - \omega_0) + \phi_2 \cdot \frac{(\omega - \omega_0)^2}{2} + \phi_3 \cdot \frac{(\omega - \omega_0)^3}{6} + \dots \quad (4.2)$$

This allows for a straightforward approach to comprehending the effect of material dispersion on the pulse. The first term in the expansion is simply $\phi(\omega_0) = k(\omega_0) \cdot L$, where $k(\omega)$ is the propagation constant defined, with consideration of the linear refractive index (n) of the material, as $k(\omega) = \frac{\omega n}{c}$ where c is the speed of light and L is the propagation length in the medium. The group velocity is then defined as $v_g = \frac{d\omega}{dk} = \frac{c}{n} - \frac{kc}{n^2} \cdot \frac{dn}{dk}$. Here we see that if the refractive index does not vary with frequency, $\frac{dn}{dk} = 0$, then $\frac{d\omega}{dk} = \frac{c}{n}$, which happens to be the phase velocity. Therefore, both the group and phase velocity are independent of frequency and the material is said to be non-dispersive. However, when both group and phase velocity vary with frequency we observe dispersion. From this we see that the first term in Eq.(4.2) adds a constant phase. The second term is proportional to $\frac{1}{v_g}$ and adds a delay to the pulse. The third term is referred to as the *group delay dispersion* (GDD) and is proportional to $\frac{d}{d\omega}(\frac{1}{v_g})$. It introduces a frequency dependent delay of the different spectral components of the pulse, therefore, inducing a temporal change in the pulse. The fourth term is referred to as the *third order dispersion* (TOD) and applies a quadratic phase across the pulse. However, for our purposes we can truncate the series to the third term. Now we can rewrite the output pulse in terms of the expanded spectral phase:

$$E_{out}(\omega) = \sqrt{A_\omega} \exp^{-ln2 \left(\frac{2(\omega - \omega_0)}{\Delta\omega} \right)^2} \exp^{-j \left(\phi_{2,pulse} + \phi_{2,mat} \frac{(\omega - \omega_0)^2}{2} \right)} \quad (4.3)$$

The phases in frequency domain are additive, which is the advantage of performing these calculations in Fourier space. Performing an inverse Fourier transform, the pulse in time domain is given by:

$$E_{out}(t) = \sqrt{A_t} \exp^{\frac{4(ln2)t^2}{2[\Delta t^2 + j4(ln2)\phi_2]}} \quad (4.4)$$

where ϕ_2 is the sum of the group delay dispersion of the material and the group delay of the pulse. The output pulse duration, Δt_{out} , is obtained by squaring the electric field to obtain the intensity and relating it to the general form of the Gaussian pulse:

$$\exp^{-ln2 \left(\frac{2t}{\Delta t_{out}} \right)^2} = \exp^{\frac{4(ln2)t^2 \Delta t^2}{\Delta t^4 + 16(ln2)^2 \phi_2^2}}$$

$$\Delta t_{out} = \frac{\sqrt{\Delta t^4 + 16(ln2)^2 \phi_2^2}}{\Delta t} \quad (4.5)$$

Isolating the GDD (ϕ_2) and replacing the transform limited pulse duration with the time-bandwidth product, the GDD can be expressed in terms of accessible quantities like the pulse width and spectrum:

$$\phi_2 = \frac{1}{4(ln2)} \sqrt{\left(\frac{c_B \Delta t_{out}}{\Delta \nu} \right)^2 - \left(\frac{c_B}{\Delta \nu} \right)^4} \quad (4.6)$$

where $\Delta\nu = c\Delta\lambda/\lambda^2$. By measuring the spectrum and performing an autocorrelation measurement, the GDD can be determined. In order to estimate the GDD introduced due to propagation through a material, the *group velocity dispersion* (GVD) needs to be calculated. GDD is simply the GVD multiplied by the propagation length, L , in the medium. The GVD is given by $\frac{\lambda^3}{2\pi c^2} \left(\frac{d^2n}{d\lambda^2} \right)$. The dependence of the refractive index on the wavelength for a specific medium is generally in the form of a Sellmeier equation so higher order derivatives can be easily calculated. In the following section, the derived equations will be applied to the specific prism-pair pulse stretching set-up used in this experiment to calculate the GDD introduced to the pulse when the separation distance between the prisms is varied.

4.3 Prism-pair Pulse Stretching Set-up

As discussed in the introduction, through dispersion a pulse can acquire positive or negative chirp, which means that the higher frequency components are lagging behind the lower frequency components or the lower frequency components are lagging behind the higher ones, respectively. Positive chirp corresponds to a positive GDD, while a negative chirp corresponds to a negative GDD. The refractive index tends to be larger for shorter wavelengths and smaller for longer wavelengths making $\frac{dn}{d\lambda}$ always negative. A pulse experiencing dispersion always experiences a positive chirp, positive GDD. However, angular dispersion using prisms introduces a negative GDD to the pulse, which is generally used to eliminate the effects of dispersion and allows the pulse to reach the transform limit. With a transform limited pulse, introducing positive or negative GDD will result in equivalent stretching of the pulse-width. In a prism-pair set-up the amount of GDD is governed primarily by the separation distance of the prisms, which is the parameter that controls the amount of dispersion introduced. Therefore even if the pulse is not transform limited, it can be stretched by simply increasing the separation distance between the prisms, beyond the distance required to compensate for dispersion.

The unfolded geometry of the prism compressor/stretcher consists of a four prism single pass sequence. The same effect can be achieved using two prisms in a double pass geometry with a folding mirror as illustrated in Figure 4.1. Figure 4.1 schematically illustrates the set-up used in this measurement. The beam enters the first prism near the apex at Brewster angle to maximise transmission. The first prism disperses the beam with the blue component of the beam undergoing a larger refraction than the red component. The second prism collimates the beam with the entrance angle of the second prism being to the entrance angle of the first prism; this ensures collimation. The beam is then returned through the two prisms in the same path at a different height to spatially recombine the beam. The wavelength dependent path length, $P(\lambda)$, due to dispersion is given by:

$$P = 2l\cos(\beta)$$

where l is the distance between the apexes of the two prisms and β is the angle of the dispersed beam after the first prism. The angle β can be estimated from, $\beta \approx -2\frac{dn}{d\lambda}\Delta\lambda$. The GDD introduced by this prism sequence is then given by [57]:

$$GDD_{prism} = \left(\frac{\lambda^3}{2\pi c^2}\right) \frac{d^2 P(\lambda)}{d\lambda^2}$$

$$GDD_{prism} \approx \frac{\lambda^3}{2\pi c^2} \left(4l \left(\left(\frac{d^2 n}{d\lambda^2} + \left(2n - \frac{1}{n^3} \right) \left(\frac{dn}{d\lambda} \right)^2 \right) \sin(\beta) - 2 \left(\frac{dn}{d\lambda} \right)^2 \cos(\beta) \right) + 4 \left(\frac{d^2 n}{d\lambda^2} \right) (2D_{1/e^2}) \right)$$

where D_{1/e^2} is the diameter of the beam entering the first prism at $1/e^2$. However, β is relatively

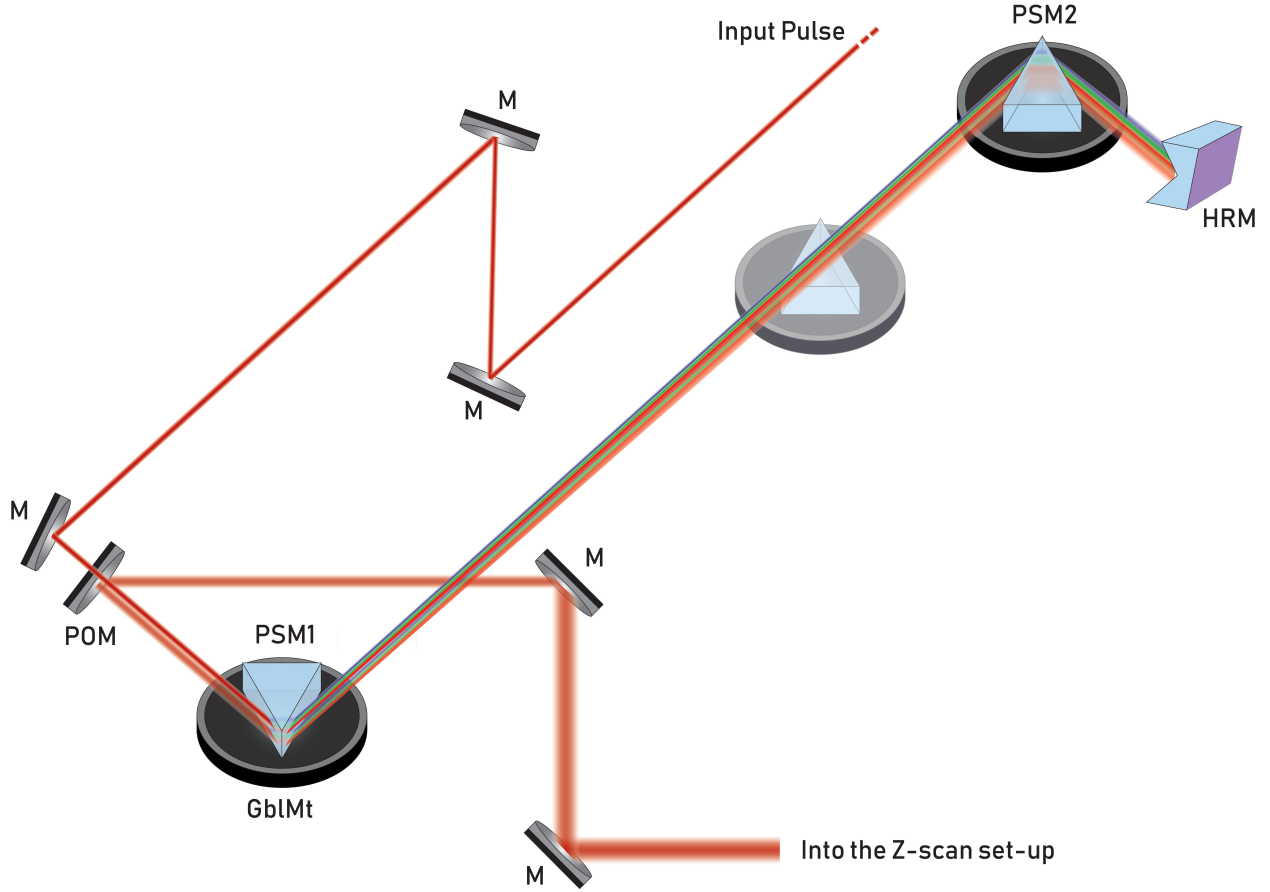


Figure 4.1: **Prism-pair pulse stretching setup.** Schematic illustration and an image of the prism-pair pulse stretching setup. The input beam is coupled from the high power variable attenuator in front of the laser and then subsequently couples to Z-scan set up at the output, both illustrated in Figure 3.2. A few mirrors are used to guide the beam into the first prism which is mounted on a gimble mount (GblMt) allowing 6 degrees of freedom. The beam is dispersed by the first prism (PSM1) and the diverging beam is then coupled to a second prism (PSM2) where it collimates on the other side. A hollow roof mirror (HRM) reflects the beam back exactly in the same path, but at a height 1 cm lower than the first beam. The beam follows the same path back and is reflected by a half pick-off mirror (POM). PSM2 is moved along the path of the beam to change the separation distance to vary the stretching factor. The complete reference to components in the schematic is provided in Table B.1.

small, so $\sin(\beta) \ll \cos(\beta)$, and the above equation can be simplified to:

$$GDD_{prism} \approx \frac{\lambda^3}{2\pi c^2} \left(-4l \left(2 \left(\frac{dn}{d\lambda} \right)^2 \right) + 4 \left(\frac{d^2n}{d\lambda^2} \right) (2D_{1/e^2}) \right) \quad (4.7)$$

The first term is always negative and is governed by the prism separation, l . The second term is always positive and depends on the path length through the prism, which introduced a positive dispersion. It is important to align the beams to enter and exit the prisms as close to the apex as

possible to reduce positive dispersion.

The derivatives are obtained using the Sellmeier equation [58]:

$$n^2(\lambda) = 1 + \frac{B_1\lambda^2}{\lambda^2 - C_1} + \frac{B_2\lambda^2}{\lambda^2 - C_2} + \frac{B_3\lambda^2}{\lambda^2 - C_3} \quad (4.8)$$

where $B_{1,2,3}$ and $C_{1,2,3}$ are material specific experimental Sellmeier coefficients, and λ is the wavelength of interest.

As mentioned previously, precision in angular alignment is of fundamental importance when building this set-up. The bulk of time is spent perfecting the alignment as it affects the temporal and spatial properties of the exiting beam. In addition to that there are a few practical points that must be considered when building this set-up. **(i) Beam size:** Given an initial beam diameter, angular dispersion will only increase the spatial size of the beam on exit. Even on return, unless perfectly aligned, the beam diameter will be larger. Therefore, when choosing the prism size, it is important to consider the available prism face area where the beams will be entering and exiting. This will also limit how far the prisms can be placed as the beam will grow larger with longer distances. **(ii) Spatial chirp:** Since the beam has to be dispersed and recombined, it is very likely that due to slight misalignment the beam is not combined correctly and there is spatial separation of the frequency components across the beam cross-section. A simple way to check is up coupling the beam into a spectrometer and moving the across the detector and observing changes in the spectrum. If there are shifts in the spectra, it may mean that the wavelengths are still spatially separated. **(iii) Return mirror:** In an unfolded geometry, there would be 4 prisms that would accomplish the task of dispersion and recombination, however, for efficiency and space, 2 prisms are used (Figure ??) with a folding mirror at the end to return the beam in the same path at a different height. It is important to use a mirror, rather than a conventional retroreflector. A retroreflector will invert the image of the beam rather than simply reflect it back. Use of appropriate equipment is important.

The measurement was performed at 900 nm, where the noise of the detectors can be kept low and there is sufficient power from the laser. Equilateral dispersive prisms made of N-SF11 flint glass were used. The Sellmeier coefficients for this material are: $B_{1,2,3} = 1.737, 0.3137, 1.899$, and $C_{1,2,3} = 1.319 \times 10^{-2} \mu m^2, 6.231 \times 10^{-2} \mu m^2, 1.552 \times 10^2 \mu m^2$, respectively. Using Eq. (4.8) the linear refractive index (n), the first-order derivative ($\frac{dn}{d\lambda}$) and the second-order derivative ($\frac{d^2n}{d\lambda^2}$) are calculated to be 1.7594, $-0.0427 \mu m^{-1}$ and $0.121 \mu m^{-1}$, respectively. The spectrum obtained for beam prior to stretching is shown in Figure 4.2. The spectral bandwidth obtained from this spectrum is 11.96 nm. Using the time-bandwidth product the transform limited pulse duration for the spectral bandwidth is calculated to be 99.56 fs. In the subsequent section, the results for the autocorrelation measurement for the original and stretched beams will be presented.

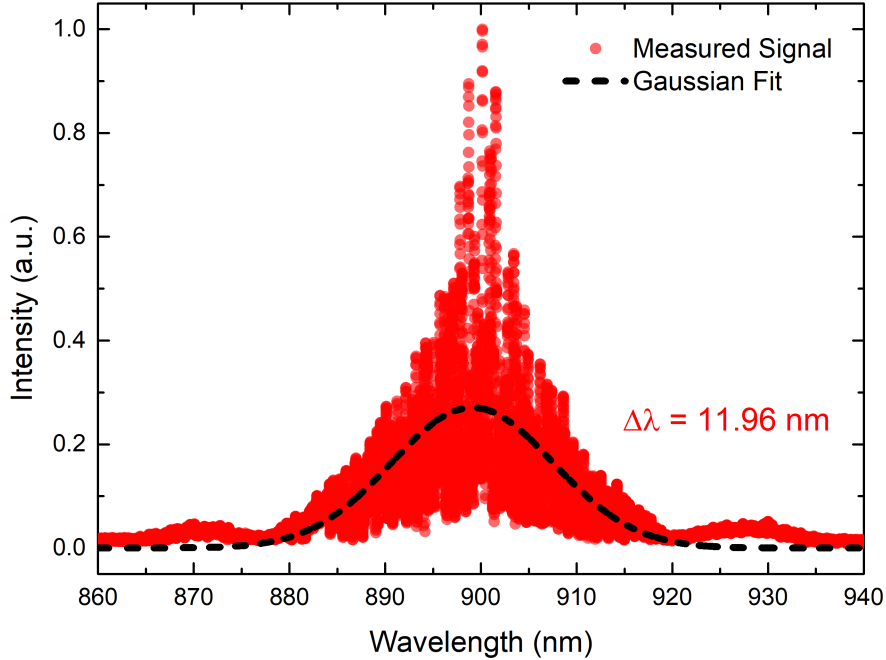


Figure 4.2: **Spectrum of the unmodified beam exiting the laser at 900 nm.** The spectrum of the beam at 900 nm without pulse-stretching. A spectral bandwidth of 11.96 nm is obtained using a Gaussian fit. The beam is measured after the power attenuation set-up at the exit of the laser to ensure no additional optics introduce dispersion.

4.3.1 Autocorrelation characterisation

The concept of autocorrelation is prevalent in several fields of study. Intrinsically, autocorrelation refers to the correlation of a signal with itself as a function of delay time. This general concept is applied to the measurement of the duration of ultrashort pulses where conventional photodiodes and detectors are too slow to directly measure the duration. In our measurement we use intensity autocorrelation to measure the duration of the prism-pair stretched pulses. In intensity autocorrelation, the beam is split using a beam splitter, creating two copies of itself. One arm is directed towards a translating mirror or a rotating mirror, as in our case, to delay of the beams. Then both beams are focused onto a $\chi^{(2)}$ nonlinear crystal, where a shorter wavelength signal is generated through the mechanism of second-harmonic generation (SHG), when there is temporal overlap of the two beams [59]. Due to particular criteria for SHG like momentum matching, near perfect spatial overlap on the crystal and high peak power, the alignment is imperative to obtaining a signal. A pre-built custom rotating mirror autocorrelator was used in this measurement. The autocorrelator is shown in Figure 4.3 with beam paths shown for clarity. The nonlinear crystal used here is BBO. There is a shortpass filter placed before the detector to isolate the harmonic

signal (blue).

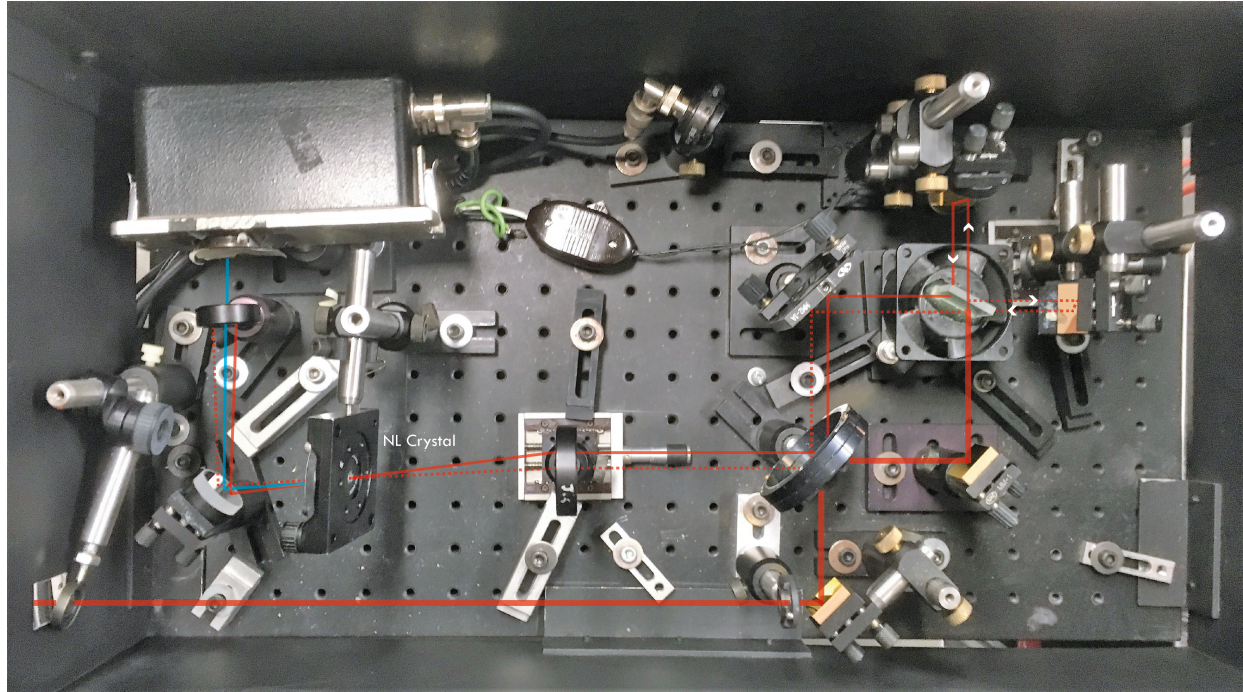


Figure 4.3: **Rotating mirror autocorrelator.** The rotating glass creates a relative delay between the two beams. They appear at different heights on the output of the rotating glass. Both beams are focused down with a lens onto a BBO crystal. The generated SHG signal is directed towards a detector where a shortpass filter isolates the SHG (blue) signal.

The signal read by the slow detector is given by the integral:

$$I_M(\tau) = \int_{-\infty}^{+\infty} |E(t)E(t-\tau)|^2 dt = \int_{-\infty}^{+\infty} I(t)I(t-\tau) dt \quad (4.9)$$

where I_M is the signal read by the detector and τ is the time delay between the two pulses. For Gaussian pulses the pulse duration is $\sqrt{2}$ times longer than the full-width half maximum (FWHM) of the autocorrelation signal.

The autocorrelation measurement was performed for different positions of prism-pair separation distances. The autocorrelation curves and fits are presented in Figure 4.4a and the pulse durations as a function of prism-pair separation distance is shown in Figure 4.4b. The pulse-width of the unmodified beam is observed to be 101.74 fs, which is close to the transform limit pulse-width for the measured spectral bandwidth, as presented in the previous section. The specifications of the laser source state that the pulses should be 75 fs with an internal dispersion compensation mechanism, so 75 fs should be observed at output. However, that is not what is measured and the high-power variable power attenuator comprising of a waveplate and polariser are not sufficient to add sufficient dispersion to expand the pulse by 25 fs. For a more detailed analysis of the introduced GDD, a spectrum would be taken at every separation distance to complement the autocorrelation

measurement so a time-bandwidth product can be extracted. In theory, the negative dispersion, the negative term in Eq. (4.7), would have to be large enough to overcome the initial positive chirp of the laser and the positive GDD introduced by the beam propagating inside the prisms. Looking at Figure 4.4b, it is obvious that the compensation for the laser and prism introduced dispersion is achieved within the distance of 0 and 52 cm, which is where the second data point is located. However, for the purposes of this study only an experimental realisation of pulse-stretching with negligible spatial chirp was required and achieved. Therefore, no further measurements or calculations were performed beyond the ones presented in Figure 4.2 and 4.4.

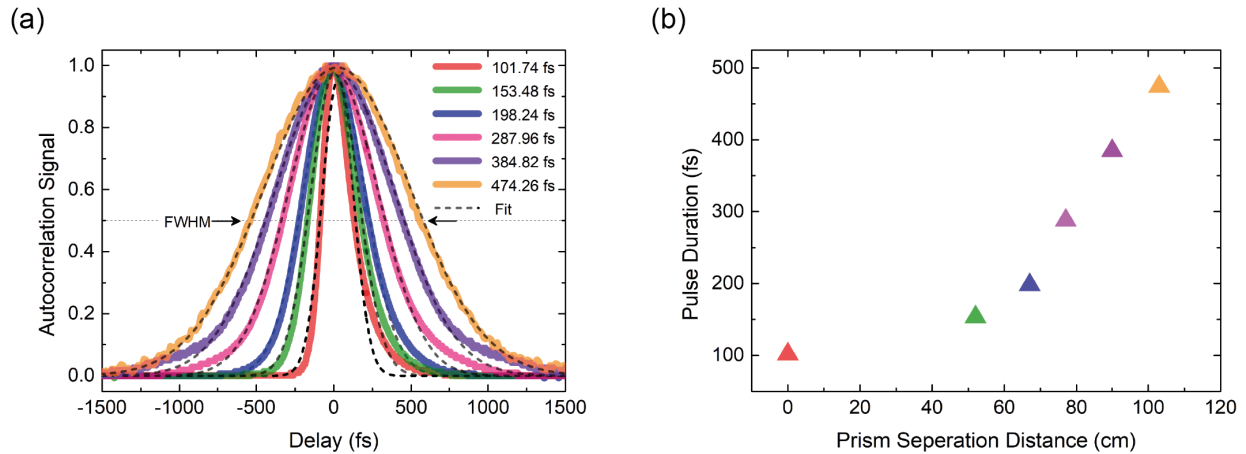


Figure 4.4: **Autocorrelation characterisation.** (a) Autocorrelation measurement, (b) Pulse duration as a function of prism-pair separation distance

The stretching factor of the set-up was limited by the space on the optical table where the separation distance between the prisms could not be increased further than 103 cm. At this point a pulse-width of 474.26 fs is achieved. For the purposes of this study, this value is sufficient as it is longer than the time-scale of the nonlinearity of interest, which is denoted by τ_1 . This time-scale is reported to range from 100-200 fs. In the subsequent chapter, these time constants will be measured.

4.4 Pulse-width dependent Z-scan measurement

It is well understood that the relative timescales of the excitation pulse and the system response times determine the induced dynamics in the system. To investigate the effects of pulse duration on nonlinear refraction, we stretch the ~ 100 fs pulse upto ~ 475 fs at 900 nm to observe the effects in the long pulse regime; longer than the duration of the nonlinearity or relaxation time, τ_1 . The beam stretched by the prism-pair pulse stretching set-up is directed into the Z-scan set-up and measurements are performed at the different stretched pulse-widths. The cumulative results of this measurement are shown in Figure 4.5 and a full set of Z-scan profiles for the presented data are also provided in Figure 4.6.

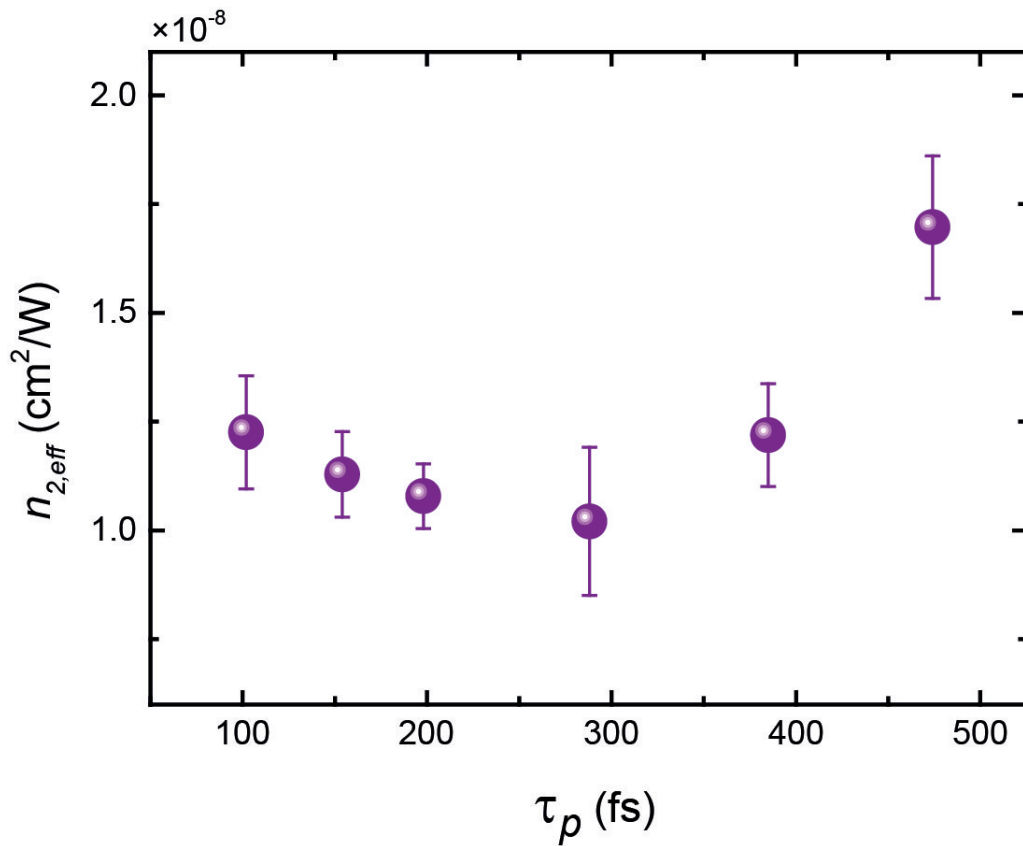


Figure 4.5: **Pulse-width dependence of $n_{2,eff}$.** The dependence of $n_{2,eff}$ on the excitation pulse-width. The $n_{2,eff}$ is observed to increase as the pulse-width becomes longer.

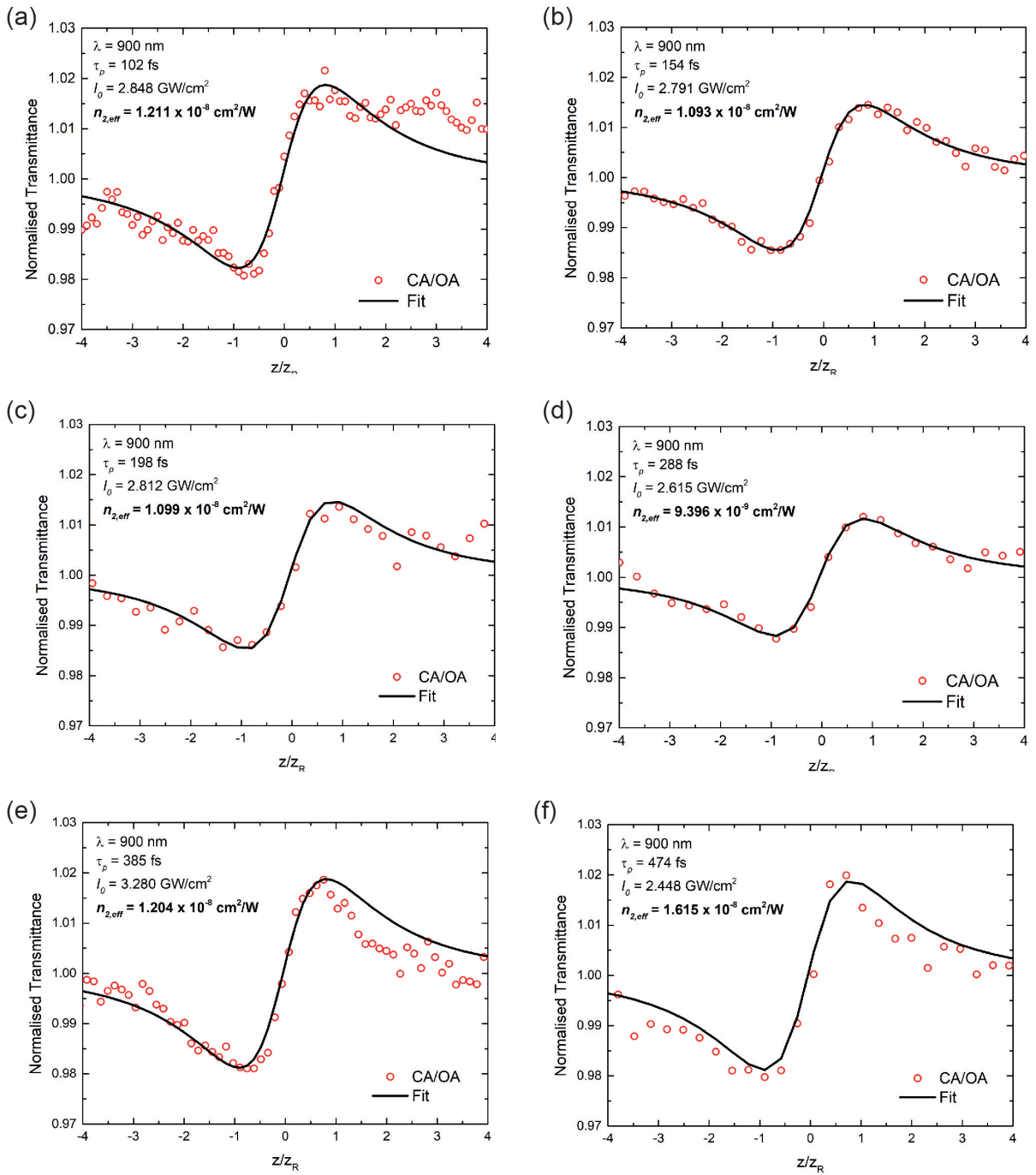


Figure 4.6: **Z-scan profiles at 900 nm with pulse durations spanning 102-475 fs.** Z-scan profiles containing absorption normalised CA (CA/OA) and the fit. Plots (a-f) show the data and fits for stretched pulse durations of 102, 154, 198, 288, 385 and 474 fs, respectively. All data sets are taken at similar on-axis irradiances with the exact values and the corresponding $n_{2,eff}$ values also provided.

The results show a clear dependence of $n_{2,eff}$ on the excitation pulse duration, with $n_{2,eff}$ becoming larger with increasing pulse-width. This trend was theoretically predicted by Vermeulen *et al.* [7] and shown here experimentally. The $n_{2,eff}$ ranges from 1.02×10^{-8} to 1.7×10^{-8} cm²/W in this pulse duration regime with a minimum between 200-300 fs. The decay constant $\tau_1 \sim 113$ fs measured in Figure 5.2 falls near the beginning of the data set. However, doping can modify the decay constant values with *p*- and *n*-doping making the time constants long and shorter, respectively [60]. This data trend coincides with previously reported Z-scan studies on graphene performed with picosecond excitations where the $n_{2,eff}$ is larger than what is reported in the femtosecond regime. In addition to this, a similar comparative analysis performed on carbon disulphide (CS₂), reference material used for calibration of Z-scan measurements, revealed a similar dependence of the $n_{2,eff}$ on pulse duration [61]. In a recent publication [7], this pulse-width dependence of $n_{2,eff}$ is theoretically derived for a regime when the effective decay constant is larger than the pulse duration in Z-scan measurements. The interplay of relative carrier heating and cooling times is said to induce a nonlinear response that may not originate only from the conventional electronic Kerr-type nonlinearity but also from what they refer to as saturable photoexcited-carrier refraction (SPCR). The saturability in graphene deviates from saturability in other 2D materials due to the presence of its unique gapless band structure which facilitates spontaneous saturation near the Dirac point even when there is no field [6]. Therefore, it is apt that we refer to the Kerr-type nonlinearity characterised using the Z-scan method as $n_{2,eff}$.

Chapter 5

Temporal evolution of the effective Kerr coefficient of Graphene

5.1 Introduction

Several natural processes in nature occur on very fast timescales like pico- (10^{-12} s) and femtoseconds (10^{-15} s). These can include atomic motion, molecular vibrations, photon absorption and emission, and other scattering events. Due to macroscopic phenomena stemming from these fast processes, it becomes imperative to measure and characterise them. To accurately measure ultra-fast processes, the uncertainty in timing must be smaller than the timescale of the process under investigation. A primary limitation of directly measuring these processes is that detectors such as photodiodes and oscilloscopes possess temporal resolutions on the order of 10^{-10} s. Therefore, a fundamentally different approach towards time-resolved measurements was developed. The technique, colloquially known as pump-probe spectroscopy, involves observing the state of a process indirectly through the observation of a *probe* laser pulse. This method has become the basis of most time-resolved measurements. This chapter focuses on studying the temporal evolution of the $n_{2,eff}$ Kerr-type nonlinearity in graphene by the means of a pump-probe integrated Z-scan measurement. The first subsection will elucidate on the methodology of the pump-probe measurement, while the latter subsection presents the experimental set-up and the results obtained via this measurement.

5.2 Pump-probe Spectroscopy

Experimental methods to measure dynamic properties of materials on a femtosecond timescale has provided a window into ultrafast processes responsible for electronic and optical properties. In a pump-probe scheme, a high-intensity optical pump pulse perturbs the system from equilibrium and a time-delayed weak probe pulse measured the photoinduced change in either transmission or reflection of the sample at that probe delay point. The probe is delayed with the use of a translation stage that provides an alternative variable path for the probe pulse; the spatial translation converts to a temporal delay via the speed of light. The technique is a sampling technique that reconstructs the signal. The entire time domain signal is not collected all at once, but is recovered by the change in optical properties as a function of probe delay time. Each data sample is the average signal over many reflected or transmitted pulses at a given time delay, thus eliminating the detector response time as a limitation of the temporal resolution. In ultrafast pump-probe spectroscopy, the minimum time resolution is limited by the pump and probe pulse durations and the interval between the measured time delays, which is determined by the spatial resolution of the delay stage. Time-resolved differential transmission $\Delta T/T$ and differential reflectivity $\Delta R/R$ measurements are both possible via this method, and both measurements together allow for the determination of the complex refractive index, complex dielectric constant, complex conductivity, or complex susceptibility.

When considering the experimental implementation of this technique, there are several configurations that this technique can be achieved depending on requirement and equipment. In general, the relative power of the probe beam should be less than the pump beam (pump/probe power ratio $> 10 : 1$), so the probe merely samples the material properties without modifying them. Also, when spatially overlapped at the sample, the focused spot size of the probe beam should be smaller than that of the pump (typically a pump/probe ratio $> 2 : 1$) so that the probe measured an area of the photoexcited sample that is approximately uniformly excited. The measurement can be using *degenerate* pump-probe beams, which means both the pump and probe have the same wavelengths. In this case isolating the probe beam is achieved with the use of an optical chopper and lock-in amplifier. The pump (or probe) can be modulated at frequency f_c and readily be extracted at the detector. In the case of a *nondegenerate* pump-probe scheme, a wavelength filter can be used to block the pump beam at the detector. It is common to use polarisation optics to isolate the probe in both pump-probe schemes. a half-wave plate and polarizing beam splitter are used to prepare the beams on entry and another polarizer is used to extinguish the pump at detection. The pump-probe are orthogonal to each other. In polarisation sensitive measurements like in waveguides, the former methods of probe isolation are more appropriate. The set-ups can also be made with the pump-probe beams in collinear or non-collinear geometry, which again is chosen depending on measurement requirements.

There are a few general considerations when piecing together a robust pump-probe experiment: **(i) Photon energy.** The photon energy or the laser wavelength determines the electronic transitions

excited by the pump pulse and sampled by the probe pulse. In semiconductor systems, the band gap is the relevant energy scale for photon energy. An above-band-gap photon creates an electron-hole pair, increasing the conductivity; while below-band-gap excitation, free-carrier absorption dominates the response. **(ii) Excitation fluence.** The pulse energy per unit area defines fluence and determines the local heating and density of quasiparticles photo-generated by the absorbed pump pulse. The fluence must be large enough to produce a measurable change with a signal-to-noise ratio larger than 1. The fluence should also be small enough to not trigger a transition of an alternate order, and be kept below the material's damage threshold. **(iii) Temporal resolution.** Temporal sensitivity is primarily determined by the pump and probe pulse widths and the spatial resolution of the delay stage. The temporal resolution (i.e. pump pulse width) needs to be better than the shortest temporal feature to accurately recover the various lifetimes present in the relaxation process. **(iv) Frequency bandwidth.** An ultrafast optical pulse necessarily has a finite bandwidth that can be calculated from the time domain waveform using a Fourier transform (FT). A distribution of pump wavelengths excites a distribution of states, while a distribution of probe wavelengths measures the electronic properties over the range of states. **(v) High sensitivity.** Measuring minuscule changes in transmission or reflectivity can be achieved with the use of high-repetition-rate lasers, high frequency modulation, lock-in detection, and high-sensitivity photodiodes. The use of an optical chopper and lock-in amplifier eliminates noise that is within the pass band of the lock-in, reducing overall noise. High-repetition-rate lasers enhance the signal-to-noise ratio by increased counting statistics of the measured signal. Higher-repetition-rate lasers and higher frequency chopping generally improve the overall signal-to-noise.

Detection is an imperative aspect of obtaining an accurate pump-probe measurement. The choice of detector is primarily determined by three criteria. **(i) Response time:** The temporal resolution of the system results from the path length difference between the pump and probe pulses and not from the response time of the detector. The required detector response time is given by the chopper modulation frequency of the pump/probe beams. For a chopper frequency of 500 Hz, the detector response time needs to at last 2 ms. **(ii) Wavelength:** The detector must have responsivity at the probe wavelength to generate a measurable signal. In semiconductor and avalanche photodiodes, the probe photon energy must be larger than the band gap of the semiconductor material. Long wavelength detectors are frequently cooled to minimise detection of thermal blackbody radiation as a means to reduce noise. **(iii) Noise equivalent power (NEP):** The NEP is the minimum optical power needed to produce a detector signal with a signal-to-noise ratio of 1. This is the smallest signal that can be recovered from the system and is an important figure of merit to minimize. In addition to the detector, a lock-in detection scheme is also common to reduce noise and isolate the desired signal. A reference signal is supplied to the lock-in amplifier using an optical chopper that is in the path of the pump (probe). The lock-in amplifier filters the measured signal for a signal with the optical chopper's modulation frequency [62].

5.3 Pump-probe Integrated Z-scan measurement

Originally introduced by Sheik-Bahae *et al.* [42], the Z-scan technique proved to be an experimentally facile yet sensitive method to extract the phase and magnitude of the Kerr coefficient. The optically induced self-refraction is quantified by relating the phase modulation of the traversing beam to the transmittance in the far-field in Closed Aperture (CA) configuration, while the Open Aperture (OA) configuration captures the effect of absorption. This technique was modified by Wang *et al.* [63] to extract the temporal evolution through the integration of a secondary time delayed beam to obtain the time-resolved Z-scan measurement. The pump-probe integrated Z-scan set-up (PPZS) is schematically illustrated in Figure 5.1. The set-up can be operated in multiple modes of measurement. In the single-beam mode, the set-up is a standard Z-scan measurement. In dual-beam mode, with the addition of a lock-in amplifier, chopper and cross-polarisation filtering, the set-up can be used to perform a standard pump-probe measurement for the extraction of relaxation time constants. When used in conjunction with the Z-scan components, the dual-beam mode is used for the time-resolved Z-scan measurements.

5.3.1 Experimental set-up

The experimental set-up for this measurement is illustrated in Figure 5.1. The excitation source is a high-power Ti:sapphire laser (Coherent Chameleon Vision S) delivering ~ 100 fs pulses at wavelengths tunable from 690 to 1050 nm, at a repetition rate of 80 MHz. When operating in single beam mode, the set-up is a classic Z-scan measurement. The beam is focused onto the sample using an anti-reflection (AR) coated achromatic doublet lens (ADL) with a focal length of 75 mm. The beam is bisected in the far-field by an AR coated non-polarising beam splitter (NP-BP) to obtain the OA and CA profiles. The OA is used to normalise for absorption and laser fluctuations in the CA trace. The normalised CA transmittance is fitted to the equation: $T(x, \Delta\Phi_0) \simeq 1 - \frac{4\Delta\Phi_0 x}{(x^2+9)(x^2+1)}$, where x is the Rayleigh length (z_R) normalised position (z/z_R) and $\Delta\Phi_0$ is the nonlinearity induced phase shift. When a pulsed source is used with pulse-width comparable to the duration of the nonlinearity, the nonlinear refractive index is extracted via $n_2 = \frac{\sqrt{2}\Delta\Phi_0}{k_0 I_0 L_{eff}}$, where k_0 is the wave vector, I_0 is the on-axis irradiance and L_{eff} is the effective length of the sample [43]. In dual-beam mode, we use degenerate pump and probe at 900 nm, in a collinear configuration with a 20:1 pump/probe ratio. The pump and probe are orthogonally polarised using a $\lambda/2$ waveplate ($\lambda/2$), polarising beam-splitter (P-BS) and polariser (Pol1) before the sample. An analyser polariser (Pol2) placed after the sample is rotated to achieve extinction of the pump beam.

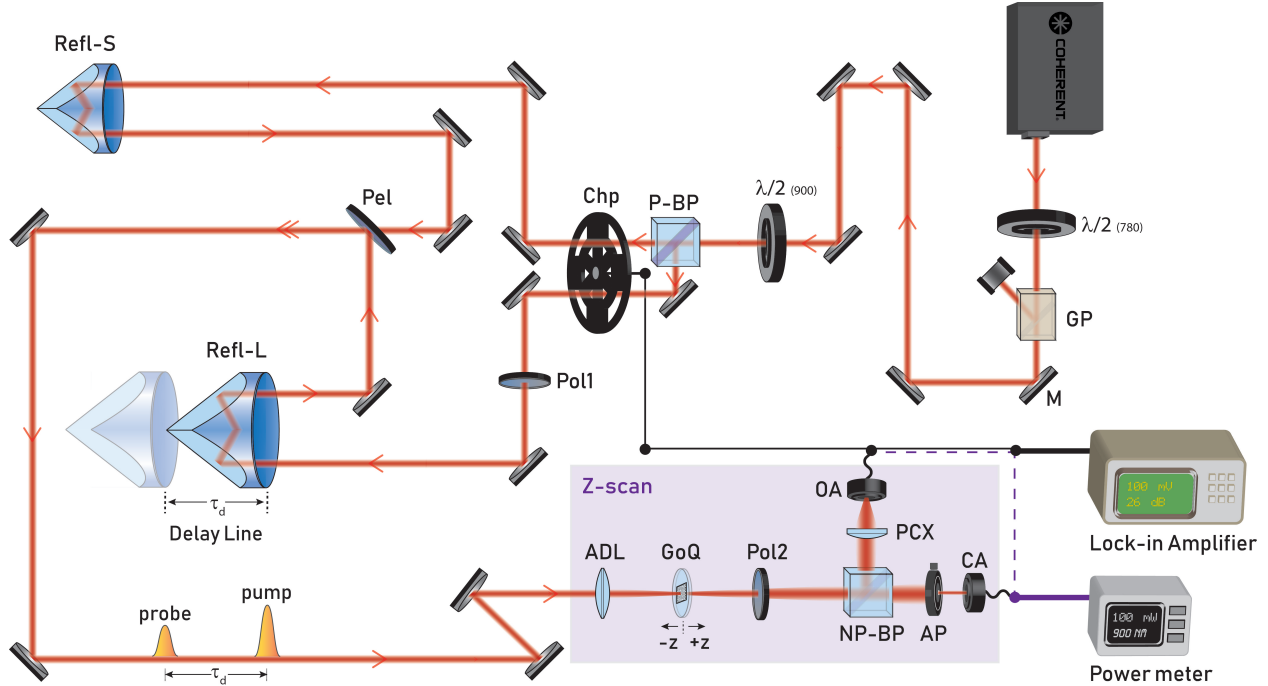


Figure 5.1: **Pump-probe integrated Z-scan set-up (PPZS)**. The source is Ti:sapphire tunable laser capable of emitting from 690 to 1050 nm at a repetition rate of 80 MHz at ~ 100 fs. The laser has a variable high power attenuator on exit comprising of a half-waveplate ($\lambda/2_{(780)}$) and a Glan-Laser polariser (GP). The beam is directed by silver mirrors (M) into another half-waveplate ($\lambda/2_{(900)}$) and polarising beamsplitter (P-BP) to prepare the orthogonal pump (transmitted) and probe (reflected) beams. Both beams are then directed through the dual-frequency chopper (Chp). The pump is directed into a small static retroreflector (Refl-S), while the probe is directed through a polariser (Pol1) and a large retroreflector (Refl-L) that is mounted on a translation stage that allows for one beam to be delayed relative to another. Upon return, both beams are combined at a pellicle beamsplitter (Pel) and guided to the Z-scan set-up. Both beams are then focused using an achromatic doublet lens (ADL) and impinge upon the graphene on quartz sample (GoQ), followed by another polariser (Pol2) which is oriented parallel to Pol1 for extinction of the pump beam. The beam is then bisected in the far-field by a non-polarising beamsplitter (NP-BP) with the reflected arm directed into the Open Aperture (OA) detector and the transmitted arm directed through an adjustable aperture (AP) into the Closed Aperture (CA) detector. For all Z-scan based measurements, single-beam or temporal, the Power Meter is utilised for data acquisition. In pump-probe mode the chopper and Lock-in Amplifier are used for data acquisition.

5.3.2 Temporal evolution of $n_{2,eff}$

The initial measurement performed using this set-up was a temporal cross-correlation to determine the time constant τ_1 of graphene, shown in Figure 5.2. The measurement reveals a τ_1 relaxation

time constant of about ~ 113 fs. In general, a complete characterisation of the relaxation dynamics requires the extraction of τ_1 and τ_2 , but for the purposes of our study obtaining a second time constant at longer time-scales is not necessary.

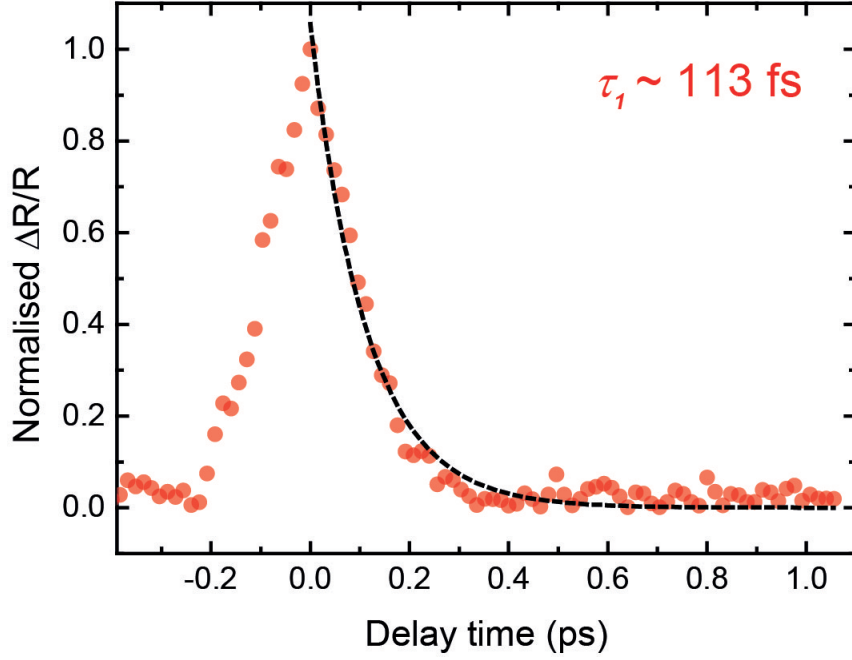


Figure 5.2: **Temporal cross-correlation in graphene.** Temporal correlation measurement on graphene with a decay constant of $\tau_1 \sim 113$ fs.

The temporal evolution of the nonlinearity is obtained using the dual-mode PPZS set-up. A single-beam (pump) Z-scan measurement is performed to locate the peak and valley positions of the sample. In order to locate the zero delay position of the probe, the sample (GoQ) is placed at the peak position and the probe is scanned until a cross-correlation signal of the pump and probe pulses is obtained, shown in Figure 5.3a. The FWHM of the signal is 150 fs, which gives a pulse duration of 110 fs for the probe, considering a pulse duration of 102 fs for the pump. A similar scan is run at the valley position and both time-resolved data sets are used to extract the differential peak-valley transmittance, $\Delta T_{pv}(t_d) = \pm \left[\frac{T(t_d, Z_p)}{T_{OA}(t_d, Z_p)} - \frac{T(t_d, Z_v)}{T_{OA}(t_d, Z_p)} \right]$, where $Z_{p/v}$ are the positions of the peak and valley, respectively, t_d is the probe delay, and T_{OA} is the OA transmittance for normalisation. The sign of ΔT_{pv} is given by the sign of $Z_p - Z_v$. The pump power used for this measurement was 200 mW, equating to an intensity of ~ 3.5 GW/cm². The pump to probe power ratio was kept at 20:1. In general, the far-field aperture should only allow about 1% of light transmittance to isolate the effect of wave front distortion due to phase modulation, however, due to the weak signal of the probe the aperture is opened to allow 10% of transmittance with additional averaging at each acquisition point.

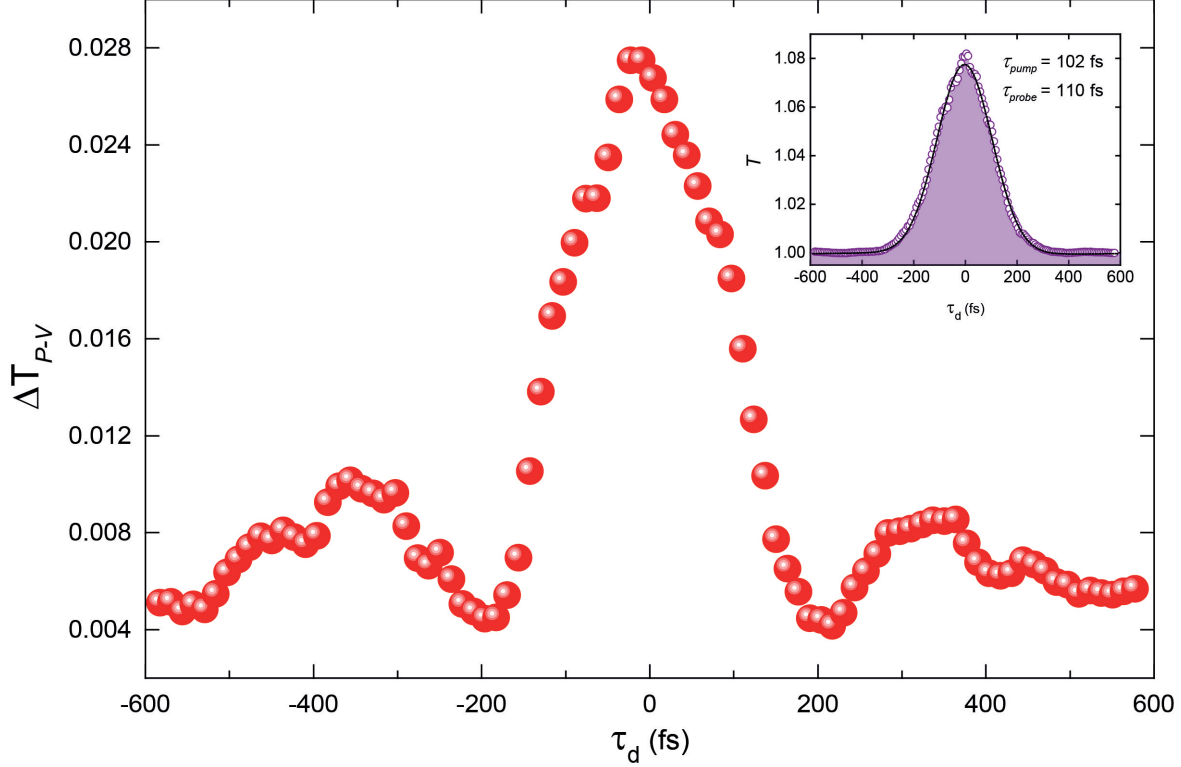


Figure 5.3: **Pump-probe integrated Z-scan measurement.** Time-resolved degenerate Z-scan measurement of graphene. Since ΔT_{pv} is proportional to $n_{2,eff}$, the plot follows the evolution of the induced phase modulation in graphene. The effect peaks at zero time delay and relaxes at longer timescales, showing some oscillatory behaviour as it relaxes. **(Inset)** Temporal cross correlation of pump and probe pulses at peak position.

The temporal evolution of the nonlinearity is shown in Figure 5.3b. The effect peaks at zero probe delay and relaxes on the time-scale of τ_1 , while at longer time scales, τ_2 , ΔT_{pv} shows no discernible variation. The symmetric shape of the figure leads us to believe that in this measurement we are simply observing the probe following the pump signals rather than unravelling the nonlinear phenomena hidden at shorter time scales. This is also supported by the fact that the pulse duration of the pump and probe is similar to the measured temporal cross-correlation extracted in Figure 5.2. Therefore, we can conclude that the relaxation dynamics contributing to the observation of the nonlinear refraction are simply too fast to be measured by our laser pulses in this manner. The variation of ΔT_{P-V} or the induced phase shift $\Delta\Phi$ seen in Figure 5.3 relates to the Gaussian power distribution of the pump pulse which reaches its maximum value (i.e. ~ 3.5 GW/cm²) at the center peak of the pulse. Therefore, according to $n_{2,eff} = \frac{\sqrt{2}\Delta\Phi_0}{k_0 I_0 L_{eff}}$, the $n_{2,eff}$ remains constant relatively constant at a value of 1.12×10^{-8} cm²/W as the increasing ΔT_{P-V} is simply balanced by the increasing on-axis irradiance, I_0 . This measurement clearly shows that on the time scale greater than the heating and cooling times, the probe follows the pump and Kerr nonlinearity is

tunable and controllable over this time scale. The modulation is understood through the relation $n = n_0 + \Delta n$, where $\Delta n = n_{2,eff}I$, and the Δn parameter varies while $n_{2,eff}$ remains constant. For the purposes of all-optical switching the on/off time of the nonlinearity is controlled by the pulse-duration and power of pulse. If the pulse-duration is longer than the relaxation times of the nonlinearity, then the evolution of the observed nonlinearity simply follows the Gaussian power distribution of the pulse. In this way through modulation of the Δn term, by changing the pulse properties, the switch can be controlled. However, there is saturation that takes place at relatively high intensities, leading to a deviation between the pump power within the pulse and the observed Δn .

Chapter 6

Conclusions

Through the systematic measurement and analysis of the effect of the spectral and temporal properties of the pulse, we were able to gain a more fundamental understanding of the parameters governing the observed nonlinear optical effect in graphene. In general, graphene shows the ability to have its nonlinear behaviour be modulated in both magnitude and sign, somehow that is limited in current silicon based photonics. Until now no study has been performed explicitly addressing this point of contention. This sheds significant light on the widespread debate in the field regarding the large variation in the $n_{2,eff}$ value for graphene due to varying experimental conditions and sample preparation techniques.

The dependence of $n_{2,eff}$ on the exciting wavelength revealed a quadratic ($n_{2,eff} \propto \lambda^2$) relationship both experimentally and theoretically. Through the pulse-duration dependent measurement, we were able to confirm the theoretically predicted relationship between $n_{2,eff}$ and the laser pulse-duration in the hundreds of femtosecond regime, with $n_{2,eff}$ growing larger with longer pulse-duration. The time-resolved Z-scan measurement revealed that the heating and cooling dynamics within our graphene sample are too fast to be probed using ~ 100 fs pulses using this method. However, this method reveals a practical application in all-optical ultrafast switching of the nonlinearity, completely controlled by the pulse-duration and power of the impinging laser pulse. Throughout all our experiments, the value for $n_{2,eff}$ remains positive.

For future experiments, the characterisation can be extended to include Fermi level modulation via the electric field effect with the use of gated samples. Doping is a significant contributor to the modulation of $n_{2,eff}$ in graphene, as discussed extensively in theory, and an experimental characterisation would significantly contribute to the understanding of this nonlinearity. In addition to that, provide a sample tunable parameter rather than source tunable parameters, which are harder to control and can offer little variation. This should also be conducted with common substrate materials as substrate interactions can prove significant to what is observed from graphene.

With this study we have gained a fundamental understanding of the underlying processes governing the nonlinear optical phenomena and parameters to modulate the effect. In doing so we can accurately form predictable models for the purposes of photonic device design.

References

- [1] Wikimedia. Gaussian beam waist. [Online]. Available: <https://commons.wikimedia.org/wiki/File:GaussianBeamWaist.svg>
- [2] K. S. Novoselov, A. K. Geim, S. V. Morozov, D. Jiang, Y. Zhang, S. V. Dubonos, I. V. Grigorieva, and A. A. Firso, “Electric field effect in atomically thin carbon films,” *Science*, vol. 306, no. 5696, pp. 666–669, Oct 2004. [Online]. Available: <https://doi.org/10.1126/science.1102896>
- [3] N. D. Mermin and H. Wagner, “Absence of ferromagnetism or antiferromagnetism in one- or two-dimensional isotropic heisenberg models,” *Science*, vol. 17, no. 22, pp. 1133–1136, Nov 1966. [Online]. Available: <https://doi.org/10.1103/PhysRevLett.17.1133>
- [4] A. H. C. Neto, F. Guinea, N. M. R. Peres, K. S. Novoselov, , and A. K. Geim, “The electronic properties of graphene,” *Review of Modern Physics*, vol. 81, no. 1, Jan-Mar 2009. [Online]. Available: <https://journals.aps.org/rmp/abstract/10.1103/RevModPhys.81.109>
- [5] B. Semnani, “Graphene-assisted integrated nonlinear optics,” Ph.D. dissertation, Electrical and Computer Engineering, University of Waterloo, Waterloo ON Canada, 2018.
- [6] B. Semnani, R. Jago, S. Safavi-Naeini, A. H. Majedi, E. Malic, and P. Tassin, “Anomalous optical saturation of low-energy dirac states in graphene and its implication for nonlinear optics,” *arxiv*, 2018. [Online]. Available: <https://arxiv.org/abs/1806.10123>
- [7] N. Vermeulen, D. Castell-Lurbe, M. Khoder, I. Pasternak, A. Krajewska, T. Ciuk, W. Strupinski, J. Cheng, H. Thienpont, and J. V. Erps, “Graphenes nonlinear-optical physics revealed through exponentially growing self-phase modulation,” *Nature Communications*, no. 9, Jul 2018. [Online]. Available: <https://www.nature.com/articles/s41467-018-05081-z#article-info>
- [8] P. P. Banerjee, *Nonlinear Optics: Theory, Numerical Modeling, and Applications*. Marcel Dekker, Inc., 2004.
- [9] R. Y. Chiao, E. Garmire, and C. H. Townes, “Self-trapping of optical beams,” *Physical Review Letters*, vol. 13, no. 15, pp. 479–482, October 1964. [Online]. Available: <https://doi.org/10.1103/PhysRevLett.13.479>
- [10] S. A. Mikhailov, “Non-linear electromagnetic response of graphene,” *A Letters Journal Exploring the Frontiers of Physics*, vol. 79, no. 2, June 2007. [Online]. Available: <https://doi.org/10.1209/0295-5075/79/27002>

- [11] J. Cheng, N. Vermeulen, and J. Sipe, “Numerical study of the optical nonlinearity of doped and gapped graphene: From weak to strong field excitation,” *Physical Review B*, vol. 92, no. 23, Dec 2015. [Online]. Available: <https://doi.org/10.1103/PhysRevB.92.235307>
- [12] K. J. Ooi, L. K. Ang, and D. T. Tan, “Waveguide engineering of graphene’s nonlinearity,” *Applied Physics Letters*, vol. 105, no. 11, p. 111110, Sep 2014. [Online]. Available: <https://doi.org/10.1063/1.4895934>
- [13] S. Mikhailov, “Quantum theory of the third-order nonlinear electrodynamic effects of graphene,” *Physical Review B*, vol. 93, no. 08, Jul 2016. [Online]. Available: <https://doi.org/10.1103/PhysRevB.93.085403>
- [14] B. Semnani, A. H. Majedi, and S. Safavi-Naeini, “Nonlinear quantum optical properties of graphene,” *Journal of Optics*, vol. 18, no. 03, p. 14, Feb 2016. [Online]. Available: <https://doi.org/10.1088/2040-8978/18/3/035402>
- [15] S. A. Mikhailov and K. Ziegler, “Nonlinear electromagnetic response of graphene: frequency multiplication and the self-consistent-field effects,” *Journal of Physics: Condensed Matter*, vol. 20, no. 38, Aug 2008. [Online]. Available: <https://doi.org/10.1088/0953-8984/20/38/384204>
- [16] Z. Zhang and P. L. Voss, “Full-band quantum-dynamical theory of saturation and four-wave mixing in graphene,” *Optics Letters*, vol. 36, no. 23, pp. 4569–4571, Dec 2011. [Online]. Available: <https://doi.org/10.1364/OL.36.004569>
- [17] J. L. Cheng, N. Vermeulen, and J. E. Sipe, “Third order optical nonlinearity of graphene,” *New Journal of Physics*, vol. 16, May 2014. [Online]. Available: <https://doi.org/10.1088/1367-2630/16/5/053014>
- [18] D. Chatzidimitriou, A. Pitolakis, and E. E. Kriezis, “Rigorous calculation of nonlinear parameters in graphene-comprising waveguides,” *Journal of Applied Physics*, vol. 118, no. 2, July 2015. [Online]. Available: <https://doi.org/10.1063/1.4926501>
- [19] D. B. S. Soh, R. Hamerly, and H. Mabuchi, “Comprehensive analysis of the optical kerr coefficient of graphene,” *Physical Review A*, vol. 94, no. 2, Aug 2016. [Online]. Available: <https://doi.org/10.1103/PhysRevA.94.023845>
- [20] V. A. Margulis, E. E. Muryumin, and E. A. Gaiduk, “Quadratic electro-optic kerr effect in doped graphene,” *Journal of Optics*, vol. 19, no. 6, May 2017. [Online]. Available: <https://doi.org/10.1088/2040-8986/aa6b6a>
- [21] Z.-W. Li, G.-Q. Liu, Q.-Z. Huang, J.-S. Xia, and Y. Wang, “Intensity dependent refraction and absorption in doped graphene by perturbation theory,” *Optik - International Journal for Light and Electron Optics*, vol. 156, pp. 975–980, Mar 2018. [Online]. Available: <https://doi.org/10.1016/j.ijleo.2017.12.042>
- [22] E. Hendry, P. Hale, J. Moger, A. Savchenko, and S. Mikhailov, “Coherent nonlinear optical response of graphene,” *Physical Review Letters*, vol. 105, no. 09, Aug 2010. [Online]. Available: <https://doi.org/10.1063/1.3623760>
- [23] M. B. M. Krishna, V. P. Kumar, N. Venkatramaiah, R. Venkatesan, and D. N. Rao, “Nonlinear optical properties of covalently linked graphene-metal porphyrin composite

- materials,” *Applied Physics Letters*, vol. 98, no. 8, Feb 2011. [Online]. Available: <https://doi.org/10.1063/1.3553500>
- [24] R. Ciesielski, A. Comin, M. Handloser, K. Donkers, G. Piredda, A. Lombardo, A. C. Ferrari, and A. Hartschuh, “Graphene near-degenerate four-wave mixing for phase characterization of broadband pulses in ultrafast microscopy,” *Nano Letters*, vol. 15, no. 8, p. 49684972, Jun 2015. [Online]. Available: <https://doi.org/10.1021/acs.nanolett.5b00893>
- [25] H. Zhang, S. Virally, Q. Bao, L. K. Ping, S. Massar, N. Godbout, and P. Kockaert, “Z-scan measurement of the nonlinear refractive index of graphene,” *Optics Letters*, vol. 37, no. 11, pp. 1856–1858, Jun 2012. [Online]. Available: <https://doi.org/10.1364/OL.37.001856>
- [26] W. Chen, G. Wang, S. Qin, C. Wang, J. Fang, J. Qi, X. Zhang, L. Wang, H. Jia, and S. Chang, “The nonlinear optical properties of coupling and decoupling graphene layers,” *AIP Advances*, vol. 3, Apr 2013. [Online]. Available: <https://doi.org/10.1063/1.4802889>
- [27] L. Miao, Y. Jiang, S. Lu, B. Shi, C. Zhao, H. Zhang, and S. Wen, “Broadband ultrafast nonlinear optical response of few-layers graphene: toward the mid-infrared regime,” *Photonics Research*, vol. 3, no. 5, pp. 214–219, 2015. [Online]. Available: <https://doi.org/10.1364/PRJ.3.000214>
- [28] G. Demetriou, H. T. Bookey, F. Bianalana, E. Abraham, Y. Wang, W. Ji, and A. K. Kar, “Nonlinear optical properties of multilayer graphene in the infrared,” *Optics Express*, vol. 24, no. 12, Jun 2016. [Online]. Available: <https://doi.org/10.1364/OE.24.013033>
- [29] M. A. Duguay and J. W. Hansen, “An ultrafast light gate,” *Applied Physics Letters*, vol. 15, no. 192, pp. 192–194, Sep 1969. [Online]. Available: <https://doi.org/10.1063/1.1652962>
- [30] X. Wang, L. Yan, M. Yue, and Q. Dong, “Pump polarization dependence of the optical kerr gate with elliptically polarized probe light,” *Journal of Optics*, vol. 20, no. 2, Jan 2018. [Online]. Available: <https://doi.org/10.1088/2040-8986/aa9dc8>
- [31] E. Dremetsika, B. Dlubak, S.-P. Gorza, C. Ciret, M.-B. Martin, S. Hofmann, P. Seneor, D. Dolfi, S. Massar, P. Emplit, and P. Kockaert, “Measuring the nonlinear refractive index of graphene using the optical kerr effect method,” *Optics Letters*, vol. 41, no. 14, pp. 3281–3284, Jul 2016. [Online]. Available: <https://doi.org/10.1364/OL.41.003281>
- [32] E. Dremetsika and P. Kockaert, “Enhanced optical kerr effect method for a detailed characterization of the third-order nonlinearity of two-dimensional materials applied to graphene,” *Physical Review B*, vol. 96, no. 23, p. 235422, Dec 2017. [Online]. Available: <https://doi.org/10.1103/PhysRevB.96.235422>
- [33] K. J. Ahn, J. Y. Gwak, B. J. Lee, S. Y. Choi, M. H. Kim, I. H. Baek, Y. U. Jeong, and F. Rotermund, “Wavelength and fluence-dependent third-order optical nonlinearity of mono- and multi-layer graphene,” *Applied Optics*, vol. 56, no. 36, pp. 9920–9924, Dec 2017. [Online]. Available: <https://doi.org/10.1364/AO.56.009920>
- [34] S. Thakur, B. Semnani, and A. H. Majedi, “Spectrally-dependent z-scan measurement of the nonlinear refractive index of graphene,” *Photonics North (PN), 2017; IEEE Xplore*, Nov 2017. [Online]. Available: <https://doi.org/10.1109/PN.2017.8090599>

- [35] J. M. Dawlaty, S. S. adnd Mvs Chandrashekar, F. Rana, and M. G. Spencer, “Measurement of ultrafast carrier dynamics in epitaxial graphene,” *Applied Physics Letters*, vol. 92, no. 04, Jan 2008. [Online]. Available: <https://doi.org/10.1063/1.2837539>
- [36] S. Kumar, M. Anija, N. Kamaraju, K. Vasu, K. Subrahmanyam, A. Sood, and C. Rao, “Femtosecond carrier dynamics and saturable absorption in graphene suspensions,” *Applied Physics Letters*, vol. 95, no. 19, Oct 2009. [Online]. Available: <https://doi.org/10.1063/1.3264964>
- [37] R. W. Newson, J. Dean, B. Schmdt, and H. M. van Driel, “Ultrafast carrier kinetics in exfoliated graphene and thin graphite films,” *Optics Express*, vol. 17, no. 04, pp. 2326–2333, Feb 2009. [Online]. Available: <https://doi.org/10.1364/OE.17.002326>
- [38] J. Xu, “Linear optical characterization of graphene structure,” Ph.D. dissertation, Electrical and Computer Engineering, University of Waterloo, Waterloo ON Canada, 2017.
- [39] R. Nair, P. Blake, A. Gringorenko, K. Novoselov, T. Booth, T. Stauber, N. Peres, and A. Geim, “Fine structure constant defines visual transparency of graphene,” *Science*, vol. 320, no. 5881, p. 1308, Jun 2008. [Online]. Available: <https://doi.org/10.1126/science.1156965>
- [40] G. Xing, H. Guo, X. Zhang, T. C. Sum, and C. H. A. Huan, “The physics of ultrafast saturable absorption in graphene,” *Optics Express*, vol. 18, no. 05, pp. 4564–4574, Mar 2010. [Online]. Available: <https://doi.org/10.1364/OE.18.004564>
- [41] N. Vermeulen, D. Castell-Lurbe, J. Cheng, I. Pasternak, A. Krajewska, T. Ciuk, W. Strupinski, H. Thienpont, and J. V. Erps, “Negative kerr nonlinearity of graphene as seen via chirped-pulse-pumped self-phase modulation,” *Physical Review Applied*, vol. 6, no. 4, p. 044006, Oct 2016. [Online]. Available: <https://doi.org/10.1103/PhysRevApplied.6.044006>
- [42] M. Sheik-bahae, A. Said, and E. W. V. Stryland, “High-sensitivity, single-beam n_2 measurements,” *Optics Letters*, vol. 14, no. 17, pp. 955–957, September 1989. [Online]. Available: <https://doi.org/10.1364/OL.14.000955>
- [43] P. Chapple, J. Staromlynska, J. Hermann, , T. Mckay, and R. Mcduff, “Single-beam z-scan: Measurement techniques and analysis,” *Journal of Nonlinear Optical Physics and Materials*, vol. 06, no. 03, pp. 251–293, September 1997. [Online]. Available: <https://doi.org/10.1142/S0218863597000204>
- [44] J. Hermann and P. Wilson, “Factors affecting optical limiting and scanning with thin nonlinear samples,” *Journal of Nonlinear Optical Physics and Materials*, vol. 02, no. 04, pp. 613–629, October 1993. [Online]. Available: <https://doi.org/10.1142/S021819919300036X>
- [45] J. Hermann, “Beam shape sensitivity of spatial scanning,” *SPIE Proceedings*, vol. 1692, pp. 56–62, August 1992. [Online]. Available: <https://doi.org/10.1117/12.138068>
- [46] S. Mian, B. Taheri, and J. Wicksted, “Effects of beam ellipticity on z-scan measurements,” *Journal of the Optical Society of America B*, vol. 13, no. 05, pp. 856–863, 1996. [Online]. Available: <https://doi.org/10.1364/JOSAB.13.000856>
- [47] A. E. Siegman, “New developments in laser resonators,” *SPIE Proceedings: Optical Resonators*, vol. 1224, p. 13, June 1990. [Online]. Available: <https://doi.org/10.1117/12.18425>

- [48] P. Chapple and P. Wilson, “Z-scans with near-gaussian laser beams,” *Journal of Nonlinear Optical Physics and Materials*, vol. 05, no. 02, pp. 419–436, April 1996. [Online]. Available: <https://doi.org/10.1142/S0218863596000271>
- [49] J. Hermann and P. Wilson, “Analytical description of a nonlinear optical power limiter,” *SPIE Proceedings: Electro-Optical Materials for Switches, Coatings, Sensor Optics, and Detectors*, vol. 401, pp. 613–629, October 1990. [Online]. Available: <https://doi.org/10.1117/12.21688>
- [50] R. Sutherland, “Effects of multiple internal sample reflections on nonlinear refractive z-scan measurements,” *Applied Optics*, vol. 33, no. 24, pp. 5576–5584, 1994. [Online]. Available: <https://doi.org/10.1364/AO.33.005576>
- [51] M. Sheik-bahae, A. Said, T.-H. Wei, D. J. Hagan, and E. W. V. Stryland, “Sensitive measurement of optical nonlinearities using a single beam,” *IEEE Journal of Quantum Electronics*, vol. 26, no. 4, pp. 760–769, April 1990. [Online]. Available: <https://doi.org/10.1109/3.53394>
- [52] Thorlabs. (2009, Aug) Bp209-vis - dual scanning slit beam profiler 200 - 1100 nm 2.5 m - 9 mm. [Online]. Available: <https://www.thorlabs.com/thorproduct.cfm?partnumber=BP209-VIS>
- [53] R. Khare and P. K. Shukla, *Coherence and Ultrashort Pulse Laser Emission*. Intechopen, Dec 2010, ch. 10, pp. 205–226. [Online]. Available: <https://www.intechopen.com/books/coherence-and-ultrashort-pulse-laser-emission>
- [54] Technology and A. C. N. Corporation. (2006) Application note prism compressor for ultrashort laser pulses. [Online]. Available: https://www.newport.com/medias/sys_master/images/h25/h7f/8797242818590/Prism-Compressor-for-Ultrashort-Laser-Pulses-App-Note-29.pdf
- [55] J.-C. Diels and W. Rudolph, *Ultrashort Laser Pulse Phenomena*. Elsevier, 2006, ch. 2, pp. 61–142. [Online]. Available: <https://www.sciencedirect.com/science/book/9780122154935>
- [56] R. Photonics. Time-bandwidth product. [Online]. Available: https://www.rp-photonics.com/time_bandwidth_product.html
- [57] R.E.Sherriff, “Analytic expressions for group-delay dispersion and cubic dispersion in arbitrary prism sequences,” *Journal of Optical Society of America B*, vol. 15, no. 3, pp. 1224–1230, March 1998. [Online]. Available: <https://doi.org/10.1364/JOSAB.15.001224>
- [58] W. Sellmeier, “Zur erklärung der abnormen farbenfolge im spectrum einiger substanzen,” *Annalen der Physik*, vol. 219, no. 6, pp. 272–282, 1871. [Online]. Available: <https://doi.org/10.1002/andp.18712190612>
- [59] R. Photonics. Autocorrelators. [Online]. Available: <https://www.rp-photonics.com/autocorrelators.html>
- [60] J. C. Johannsen, S. Ulstrup, A. Crepaldi, F. Cilento, M. Zacchigna, J. A. Miwa, C. Cacho, R. T. Chapman, E. Springate, F. Fromm, C. Raidel, T. Seyller, P. D. C. King, F. Parmigiani, M. Gironi, and P. Hofmann, “Tunable carrier multiplication and cooling in graphene,” *Nano Letters*, vol. 15, no. 1, pp. 326–331, Dec 2015. [Online]. Available: <https://pubs.acs.org/doi/abs/10.1021/nl503614v>

- [61] I. Nikolakakos, A. Major, J. Aitchison, and P. Smith, “Broadband characterization of the nonlinear optical properties of common reference materials,” *IEEE Journal of Selected Topics in Quantum Electronics*, vol. 10, no. 5, pp. 1164 – 1170, Dec 2004. [Online]. Available: <https://ieeexplore.ieee.org/document/1366391/>
- [62] R. P. Prasankumar and A. J. Taylor, *Optical techniques for solid-state materials characterisation*. CRC Press, 2012.
- [63] J. Wang, M. Sheik-Bahae, D. J. H. A. A. Said, and E. W. V. Stryland, “Time-resolved z-scan measurements of optical nonlinearities,” *Journal of the Optical Society of America B*, vol. 11, no. 6, pp. 1009–1017, Jun 1994. [Online]. Available: <https://www.osapublishing.org/josab/abstract.cfm?uri=josab-11-6-1009>
- [64] H. Lorentz, *The Theory of Electrons and Application tot the Phenomena of Light and Radiant Hear*. Dover Publications, 2003 (originally published 1915).
- [65] A. Levi, *Essential Classical Mechanics for Device Physics*. IOP Books, 2016.
- [66] R. W. Boyd, *Nonlinear Optics*, 3rd ed. Academic Press, 2010.
- [67] R. C. Miller, “Optical second harmonic generation in piezoelectric crystals,” *Applied Physics Letters*, vol. 5, no. 1, pp. 17–19, July 1964. [Online]. Available: <https://doi.org/10.1063/1.1754022>
- [68] D. Weaire, B. S. Wherrett, D. A. B. Miller, and S. D. Smith, “Effect of low-power nonlinear refraction on laser-beam propagation in insb,” *Optics Letters*, vol. 4, no. 10, pp. 331–333, October 1979. [Online]. Available: <https://doi.org/10.1364/OL.4.000331>
- [69] J. Arnaud, “Representation of gaussian beams by complex rays,” *Applied Optics*, vol. 24, no. 4, pp. 538–543, February 1985. [Online]. Available: <https://doi.org/10.1364/AO.24.000538>
- [70] R. Pfisterer. (2010, Aug) Software computing: Beam analysis: The basics of gaussian beam decomposition. [Online]. Available: <http://www.laserfocusworld.com/articles/2010/07/software-and-computing-beam-analysis-the-basics-of-gaussian-beam-decomposition.html>
- [71] P. W. Milonni and J. H. Eberly, *Laser Physics*. John Wiley & Sons Inc., 2010.
- [72] Thorlabs. (2000, Oct) Wph05m-780 - 1/2 mounted zero-order half-wave plate 1 mount 780 nm. [Online]. Available: <https://www.thorlabs.com/thorproduct.cfm?partnumber=WPH05M-780>
- [73] ——. (2009, Jan) Rsp1x15 - rotation mount for 1 (25.4 mm) optics 360 continuous or 15 indexed rotation 8-32 tap. [Online]. Available: <https://www.thorlabs.com/thorproduct.cfm?partnumber=RSP1X15ad-image-0>
- [74] ——. (2000, Jan) Gl10-b - mounted glan-laser polarizer 10 mm ca, ar coating: 650 - 1050 nm. [Online]. Available: <https://www.thorlabs.com/thorproduct.cfm?partnumber=GL10-B>
- [75] ——. (2005, Dec) Pf10-03-p01-10 - 1 protected silver mirrors. [Online]. Available: <https://www.thorlabs.com/thorproduct.cfm?partnumber=PF10-03-P01-10>
- [76] ——. (2012, Jul) La1509-b-ml - 1 n-bk7 plano-convex lens sm1-threaded mount, f = 100.0 mm, arc: 650-1050 nm. [Online]. Available: <https://www.thorlabs.com/thorproduct.cfm?partnumber=LA1509-B-ML>

- [77] A. Materials. Cvd graphene on quartz substrate. [Online]. Available: <http://www.acsmaterial.com/graphene-on-quartz-substrate-839.html>
- [78] Thorlabs. (2009, May) Pt1-z8 - 25 mm (0.98) one-axis motorized translation stage 1/4-20 taps. [Online]. Available: <https://www.thorlabs.com/thorproduct.cfm?partnumber=PT1-Z8>
- [79] ——. (2015, Aug) Ccm1-bs014-m - 30 mm cage cube-mounted non-polarizing beamsplitter 700 - 1100 nm m4 tap. [Online]. Available: <https://www.thorlabs.com/thorproduct.cfm?partnumber=CCM1-BS014/M>
- [80] ——. (2000, Jun) Nd01a - reflective 25 mm nd filter sm1-threaded mount optical density 0.1. [Online]. Available: <https://www.thorlabs.com/thorproduct.cfm?partnumber=ND01A>
- [81] ——. (2015, Oct) Lb1676-b-ml - mounted n-bk7 bi-convex lens 1 f = 100.0 mm arc: 650-1050 nm. [Online]. Available: <https://www.thorlabs.com/thorproduct.cfm?partnumber=LB1676-B-ML>
- [82] ——. (2015, Mar) P500s - 1 mounted precision pinhole 500 m pinhole diameter. [Online]. Available: <https://www.thorlabs.com/thorproduct.cfm?partnumber=P500S>
- [83] Newport. Germanium detector 780-1800 nm od3 attenuator db15. [Online]. Available: <https://www.newport.com/p/918D-IR-OD3R>
- [84] ——. Benchtop optical power and energy meter, dual channel, rohs. [Online]. Available: <https://www.newport.com/p/2936-R>
- [85] Thorlabs. Tdc001 - t-cube dc servo motor controller. [Online]. Available: <https://www.thorlabs.com/thorproduct.cfm?partnumber=TDC001>
- [86] ——. (2000, Oct) Ps853 - n-sf11 equilateral dispersive prism, 25 mm. [Online]. Available: <https://www.thorlabs.com/thorproduct.cfm?partnumber=PS853>
- [87] Newport. Ugp-1 ultima gimbal prism mount, 1 in., 100 tpi adjustment screws. [Online]. Available: <https://www.newport.com/p/UGP-1>
- [88] Thorlabs. (2007, Jan) Pfd10-03-p01 - 1 inch protected silver d-shaped mirror. [Online]. Available: <https://www.thorlabs.com/thorproduct.cfm?partnumber=PFD10-03-P01>
- [89] ——. (2011, Aug) Km100d - right-handed kinematic mount for 1 inch d-shaped mirrors. [Online]. Available: <https://www.thorlabs.com/thorproduct.cfm?partnumber=KM100D>
- [90] ——. (2016, Mar) Hrs1015-p01 - 1 x 1 inch hollow roof prism mirror protected silver. [Online]. Available: <https://www.thorlabs.com/thorproduct.cfm?partnumber=HRS1015-P01>
- [91] ——. (2012, Jun) Ahwp10m-980 - 1 in mounted achromatic half-wave plate, sm1-threaded mount, 690 - 1200 nm. [Online]. Available: <https://www.thorlabs.com/thorproduct.cfm?partnumber=AHWP10M-980>
- [92] ——. (2015, Aug) Ccm1-pbs253/m - 30 mm cage cube-mounted polarizing beamsplitter cube, 900-1300 nm, m4 tap. [Online]. Available: <https://www.thorlabs.com/thorproduct.cfm?partnumber=CCM1-PBS253/M>

- [93] ——. (2014, Feb) Lpvis050-mp2 - 12.5 mm sm05-mounted linear polarizer, 550 - 1500 nm. [Online]. Available: <https://www.thorlabs.com/thorproduct.cfm?partnumber=LPVIS050-MP2>
- [94] ——. (2004, Jul) Bp145b3 - 1 in pellicle beamsplitter, coated for 45:55 (r:t) split ratio for 1-2 um. [Online]. Available: <https://www.thorlabs.com/thorproduct.cfm?partnumber=BP145B3>
- [95] Newport. (-, -) Broadband hollow retroreflector, 63.5 mm, 5 arc sec parallelism, 450-10,000 nm. [Online]. Available: <https://www.newport.com/p/UBBR2.5-5S>
- [96] ——. (-, -) Broadband hollow retroreflector, 1.0 in, 2 arc sec parallelism, 450-10,000 nm. [Online]. Available: <https://www.newport.com/p/UBBR1-2S>

Appendix A

Mathematical Derivations

A.1 Gaussian Beam Equation (GBE)

The most fundamental description of waves in electromagnetics is that of a plane wave. A plane wave is described as having wavefronts that are infinite parallel planes. The implications of this are that in the transverse direction relative to propagation, there is no spatial variation and the phase is constant across the surface of the planes. However, this simplistic wave model cannot be used to describe a laser beam, where there is evolution in the transverse plane during propagation. In order to derive an equation to describe such a wave, the usual wave equation must be modified to include transverse variation. In this section the GBE will be explicitly derived starting from Maxwell equations.

Table A.1: Maxwell Equations

Name	Equation	Interpretation
Gauss' flux theorem	$\nabla \cdot \mathbf{E} = \frac{\rho}{\epsilon}$ (A.1)	The electric flux leaving an enclosed volume is proportional to the charge inside.
Gauss' law of magnetism	$\nabla \cdot \mathbf{B} = 0$ (A.2)	The total magnetic flux through a closed surface is zero because the net of the inward and outward flux is zero as magnetic poles always comes in pairs.
Faraday's law of induction	$\nabla \times \mathbf{E} = -\frac{\partial \mathbf{B}}{\partial t}$ (A.3)	A time-varying magnetic field will produce a circulating electric field.
Ampère's circuital law	$\nabla \times \mathbf{B} = \mu(\mathbf{J} + \epsilon \frac{\partial \mathbf{E}}{\partial t})$ (A.4)	A time-varying electric field and/or a current will produce a circulating magnetic field.

Starting from Eq. (A.3), a cross product is applied to both sides. The result is expanded using the

double cross product identity $[\nabla \times (\nabla \times \mathbf{E}) = \nabla(\nabla \cdot \mathbf{E}) - \nabla^2 \mathbf{E}]$, Eq. (A.1) and Eq. (A.4):

$$\begin{aligned}\nabla \times (\nabla \times \mathbf{E}) &= -\frac{\delta(\nabla \times \mathbf{B})}{\delta t} \\ \nabla \left(\frac{\rho}{\epsilon} \right) - \nabla^2 \mathbf{E} &= \frac{\delta(\mu(\mathbf{J} + \epsilon \frac{\delta \mathbf{E}}{\delta t}))}{\delta t}\end{aligned}$$

Considering solutions in a source (\mathbf{J}) and a charge (ρ) free region, those terms are set to zero. This results in the wave equation that considers the spatial and temporal evolution of the electric field:

$$\boxed{\nabla^2 \mathbf{E} = \frac{1}{c^2} \frac{\delta^2 \mathbf{E}}{\delta t^2}; c = \frac{1}{\sqrt{\mu \epsilon}}}$$
 (A.5)

where c is the speed of light and is related to the magnetic permeability (μ_0) and the electrical permittivity (ϵ_0) in free space. In certain classes of physical problems, the solutions can be obtained by considering time-independent behaviour. The time-independent form of the wave equation is colloquially known as the *Helmholtz equation*, which can be obtained from the wave equation derived above by applying separation of variables. We start by considering an arbitrary time and space dependent wave function $\Psi = (\mathbf{r}, t) = \mathbf{A}(\mathbf{r})T(t)$. This form can then be substituted back into Eq. (A.5), and the spatial and temporal parts can be separated:

$$\frac{\nabla^2 \mathbf{A}}{\mathbf{A}} = \frac{1}{c^2} \frac{d^2 T}{dt^2}$$

Examining this equation, we can see that any spatial variation on the left depends on the temporal variation on the right, and vice versa. For this equation to be valid, both sides of the equation must be equal to a separation constant:

$$\frac{\nabla^2 \mathbf{A}}{\mathbf{A}} = -k^2 \quad \text{and} \quad \frac{1}{c^2} \frac{d^2 T}{dt^2} = -k^2$$
 (A.6)

where \mathbf{k} is the wave vector and has the relation $\mathbf{k} = \omega c$ with the angular frequency ω . The separation constant is strategically chosen in this form to ease the formulation of solutions. The constant can be substituted to obtain purely space and time dependent wave equations:

$$\boxed{(\nabla^2 + \mathbf{k}^2)\mathbf{A} = 0 \quad \text{and} \quad \left(\frac{d^2}{dt^2} + \omega^2 \right) T = 0}$$
 (A.7)

Now that the time-independent wave equation (Helmholtz) has been found, the next step towards obtaining a suitable wave equation is the application of the *paraxial approximation*. The term *paraxial* is used because all of the light must travel nearly parallel to the z -axis (extremely low divergence angle) in order for the beam to have a sufficiently slow z dependence. In order to resolve the now varying transverse components of the wave, the electric field can be written in the form of $\mathbf{E}(x, y, z) = \Psi(x, y)e^{-j\mathbf{k}z}$, where $\Psi(x, y)$ describes the transverse profile and the exponential

denotes the direction of propagation. The importance of this step is to separate the fast-varying exponential from the slow varying transverse component. The transverse function varies slowly, controlling the diameter and strength of a laser beam as it propagates. Substituting this equation into the Helmholtz equation and expanding yields:

$$\begin{aligned} & \left(\frac{\delta^2}{\delta x^2} + \frac{\delta^2}{\delta y^2} + \frac{\delta^2}{\delta z^2} + \mathbf{k}^2 \right) \Psi(x, y, z) e^{-jkz} = 0 \\ & \left(\frac{\delta^2 \Psi}{\delta x^2} + \frac{\delta^2 \Psi}{\delta y^2} + \frac{\delta^2 \Psi}{\delta z^2} - 2j\mathbf{k} \frac{\delta \Psi}{\delta z} - \mathbf{k}^2 \Psi + \mathbf{k}^2 \Psi + 1 \right) e^{-jkz} = 0 \end{aligned}$$

The paraxial approximation originates from wave analysis in ray optics. It is determined by considering these two inequalities:

$$\left| \frac{\delta^2 \Psi}{\delta z^2} \right| \ll 2\mathbf{k} \left| \frac{\delta \Psi}{\delta z} \right| \quad \text{and} \quad \left| \frac{\delta^2 \Psi}{\delta z^2} \right| \ll \left| \frac{\delta^2 \Psi}{\delta x^2} \right|, \left| \frac{\delta^2 \Psi}{\delta y^2} \right| \quad (\text{A.8})$$

The first inequality tells us that the variation of propagation is slow on the scale of the wavelength, which is to say that the amplitude (Ψ) varies slowly with z . The second inequality tells us that the variation of propagation is slow on the scale of the transverse extent of the wave, making the wavefronts nearly perpendicular to the z -axis. Under these conditions, Eq. (A.12) simplifies to:

$$\boxed{\left[\nabla_T^2 - 2j\mathbf{k} \frac{\delta}{\delta z} \right] \Psi(x, y, z) = \left(\frac{1}{r} \frac{\delta}{\delta r} \left(r \frac{\delta}{\delta r} \right) - 2j\mathbf{k} \frac{\delta}{\delta z} \right) \Psi(r, \phi, z) = 0} \quad (\text{A.9})$$

The equation derived above provides us with the paraxial wave equation (PWE) in both Cartesian and cylindrical coordinates. There is a distinction between the transverse component denoted by the subscript (∇_T), which includes the x, y components with z being considered the direction of propagation. The most important result of this derivation is that the solution to this equation are the Gaussian beam modes. Due to the geometry of Gaussian beams it is helpful to tackle the problem in cylindrical coordinates. With this form we can now insert a trial solution of the form:

$$\Psi_0 = \exp \left[-j \left(P(z) + \frac{kr^2}{2q(z)} \right) \right] \quad (\text{A.10})$$

where the subscript (Ψ_0) denotes the fundamental Gaussian mode (TEM_{00}). Inserting this trial

solution into the PWE gives:

$$\begin{aligned}
& \left(\frac{1}{r} \frac{\delta}{\delta r} \left(r \frac{\delta}{\delta r} \right) - 2j\mathbf{k} \frac{\delta}{\delta z} \right) \exp \left[-j \left(P(z) + \frac{kr^2}{2q(z)} \right) \right] = 0 \\
& \left(\frac{1}{r} \frac{\delta}{\delta r} \left(-j \frac{kr^2}{q(z)} \right) - 2k \frac{dP(z)}{dz} + \frac{k^2 r^2}{q^2(z)} \frac{dq(z)}{dz} \right) \Psi_0 = 0 \\
& \left(-j \frac{2k}{q(z)} - j \frac{kr}{q(z)} \frac{\delta}{\delta r} - 2k \frac{dP(z)}{dz} + \frac{k^2 r^2}{q^2(z)} \frac{dq(z)}{dz} \right) \Psi_0 = 0 \\
& -\frac{k^2 r^2}{q^2(z)} - j \frac{2k}{q(z)} - 2k \frac{dP(z)}{dz} + \frac{k^2 r^2}{q^2(z)} \frac{dq(z)}{dz} = 0 \\
& \frac{k^2}{q(z)} \left(\frac{dq(z)}{dz} - 1 \right) r^2 - 2k \left(\frac{dP(z)}{dz} + \frac{j}{q(z)} \right) r = 0
\end{aligned} \tag{A.11}$$

Since the equation must hold for all r , the terms can be separated by the coefficients r^2 and r , and two differential equations are obtained:

$$\frac{dq(z)}{dz} = 1 \quad \text{and} \quad \frac{dP(z)}{dz} = -\frac{j}{q(z)} \tag{A.12}$$

The solution to the first differential is: $q(z) = q_0 + z$, where q_0 is the constant of integration and is the value of q at $z = 0$. However, q_0 cannot be real or the beam would have infinite energy, therefore, the equation can be rewritten with a new imaginary constant as:

$$q(z) = z + jz_R \tag{A.13}$$

where z_R is the Rayleigh length, to be elaborated upon. The parameter $q(z)$ is called the *complex radius of curvature*, and can be rewritten with the real and complex values separated:

$$\frac{1}{q(z)} = \frac{1}{z + jz_R} = \frac{z}{z^2 + z_R^2} - j \frac{z_R}{z^2 + z_R^2} \tag{A.14}$$

Now the second differential can be solved as:

$$\begin{aligned}
\frac{dP(z)}{dz} &= -\frac{j}{q(z)} = -\frac{j}{z + jz_R} \\
jP(z) &= \int_0^z \frac{dz}{z + jz_R} \\
jP(z) &= \ln \left[1 - j \left(\frac{z}{z_R} \right) \right] \\
\exp(-jP(z)) &= \exp \left[-\ln \left(1 - j \left(\frac{z}{z_R} \right) \right) \right] \\
\exp(-jP(z)) &= \left[1 - j \left(\frac{z}{z_R} \right) \right]^{-1} \\
\exp(-jP(z)) &= \left[1 + \left(\frac{z}{z_R} \right)^2 \right]^{\frac{-1}{2}} \exp \left[j \tan^{-1} \left(\frac{z}{z_R} \right) \right]
\end{aligned} \tag{A.15}$$

The final form shown in Eq. (A.15) has the amplitude and phase separated. Given these two solutions, we first define several parameters relevant to the Gaussian beam to ease the derivation and understanding of the final GBE.

$$w_0 = \sqrt{\frac{\lambda_0 z_R}{n\pi}} \quad (\text{A.16})$$

$$w(z) = w_0 \sqrt{1 + \left(\frac{z}{z_R}\right)^2} \quad (\text{A.17})$$

$$R(z) = z \left[1 + \left(\frac{z}{z_R}\right)^2\right] \quad (\text{A.18})$$

$$\phi(z) = \tan^{-1} \left(\frac{z}{z_R}\right) \quad (\text{A.19})$$

Eq. (A.16) defines the *beam waist*, w_0 , that is the radius of the beam at focus. Following this the propagating *spot size*, $w(z)$, is defined in Eq. (A.17). Eq. (A.18) defines the *radius of curvature*, $R(z)$, that is the radius of the propagating wavefronts, where $R(z)$ is infinite at focus ($z=0$). Finally, Eq. (A.19) defines the *Guoy phase shift*, $\phi(z)$, which accounts for the phase changes during propagation. Considering the solutions found in Eq. (A.14) and Eq. (A.15), and the parameters defined above, we can finally write out the well known **Gaussian beam equation**:

$$E(r, z, t) = E_0(t) \left[\frac{w_0}{w(z)} \exp\left(-\frac{r^2}{w^2(z)}\right) \exp\left(-j\frac{kr^2}{2R(z)}\right) \exp\left(-j(kz - \phi(z))\right) \right] \quad (\text{A.20})$$

With the fundamental mode GBE now derived, we can briefly discuss the important physical implications of the parameters previously defined. It is apparent that in this form the GBE is expanded explicitly to show the spatial part, while the temporal part is contained within the leading term, $E_0(t)$. This leading term comes into play when focusing on the temporal properties of the beam. To aid this, a schematic representation of a Gaussian beam is provided in A.1 with the relevant parameters labelled. The *Rayleigh length* (z_R) in combination with the wavelength is sufficient to determine the Gaussian beam completely. It is given by:

$$z_R = \frac{\pi n w_0^2}{\lambda_0} \quad (\text{A.21})$$

The physical meaning of this parameter is evident when $z=z_R$ is inserted in Eq. (A.17), and the spot size is seen to be $\sqrt{2}w_0$. This tells us that at z_R around the focal plane, the Gaussian beam is expanded by a factor $\sqrt{2}$. It is seen as a measure of the collimation of the beam. The longer the Rayleigh length is, the lower the divergence angle (Θ). From Eq. (A.21) it is also evident that the shorter z_R , the smaller the beam waist. The *radius of curvature* ($R(z)$) is an essential component when describing spherical waves. As the analysis of the Z-scan technique depends on

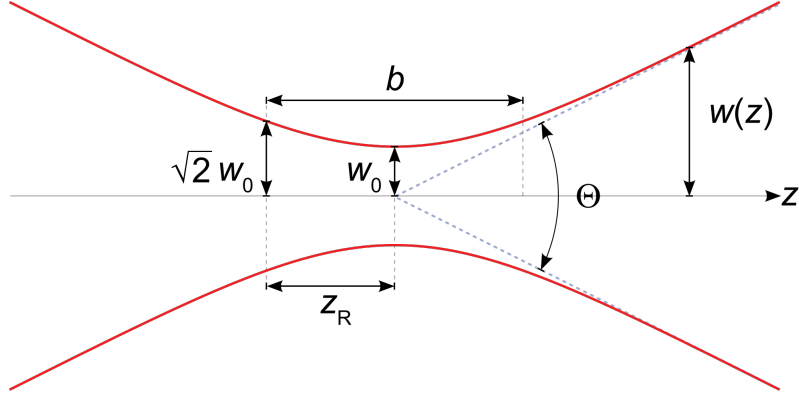


Figure A.1: Schematic illustration of a Gaussian beam [1]

the distortion of wavefronts, it becomes important to be able to describe these wavefronts. The behaviour of $R(z)$ can be summed up by considering three different regions: (1) $R(z) = \infty$ near the waist, the wavefront is perpendicular to the optic axis. (2) $R(z) = 2z_R$ at $z = z_R$, the wave is like coming from a point source at a distance z_R behind the origin. (3) $R(z) = z$ in the far-field, the wave is like generated by a point source at the origin and is follows a linear dependence. The *Guoy phase shift* ($\phi(z)$) is the imaginary component of the beam equation that accounts for the phase modulation as the beam propagates. This phase is what is tracked in the *thin* film approximation for the Z-scan technique. The wave experiences an intrinsic π phase shift as z is scanned through the confocal parameter. As the beam propagates through a medium, it accumulates an additional phase during propagation, especially when propagating through a medium.

A.2 Anharmonic Oscillator Model

We start by considering the anharmonic oscillator model which allows us to apply classical concepts of a driven damped mechanical oscillator to the interaction of an electromagnetic field to a dielectric material. This model will first be used to derive the linear response (harmonic oscillator) and then will be extended to the nonlinear regime by considering an anharmonic potential which will account for higher order processes. Unless we indulge in particle physics, the building blocks of matter are atoms. Each atom consists of a positively charged nucleus comprised of neutrons and protons, and negatively charged electrons. The atom displays charge neutrality with the protons equalling the number of electrons. The energy equilibrium resulting from the balancing of the coulombic forces endows the dielectric material with its phase stability. In the late nineteenth century, only armed with this knowledge of particle physics and classical mechanics, Lorentz [64] saw the problem of atom-field interactions in terms of a spring with one large mass (nucleus) connected to a smaller mass (the electron). Upon the impingement of an external electromagnetic field, the field couples to the spring causing a mechanical displacement from equilibrium. This displacement of an electron produces a dipole moment, $\mathbf{d} = e\mathbf{x}$, for the atom and an atomic polarisation, $\mathbf{p} = -e\mathbf{x}$, with the direction of the dipole moment oriented from negative ($-e$) to positive charge (e). Any system out of equilibrium will work to return to equilibrium, therefore, there are internal restoring forces that are vectorally opposite but equal in magnitude to oppose the external field. With a qualitative picture in mind about the process, we can start to formulate a mathematical framework to describe this process. It is appropriate at this point to list a few important equations and quantities which will be elaborated upon immediately after [65]:

$$\mathbf{F}_{restoring}(\mathbf{x}) = -m\omega_0^2\mathbf{x} - a\mathbf{x}^2 - b\mathbf{x}^3 + \dots \quad (\text{A.22})$$

$$\mathcal{U}(\mathbf{x}) = \frac{1}{2}m\omega_0^2\mathbf{x}^2 + \frac{1}{3}a\mathbf{x}^3 + \frac{1}{4}b\mathbf{x}^4 + \dots \quad (\text{A.23})$$

$$\tilde{\mathbf{E}}(t) = \mathbf{E}_1(\omega_1)e^{-j\omega_1 t} + \mathbf{E}_2(\omega_2)e^{-j\omega_2 t} + \mathbf{E}_3(\omega_3)e^{-j\omega_3 t} + \dots = \sum_n \mathbf{E}(\omega_n)e^{-j\omega_n t} \quad (\text{A.24})$$

$$\frac{d^2\mathbf{x}}{dt^2} + \gamma\frac{d\mathbf{x}}{dt} + \omega_0^2\mathbf{x} + a\mathbf{x}^2 + b\mathbf{x}^3 + \dots = -\frac{e}{m}\mathbf{E} \quad (\text{A.25})$$

$$\mathbf{P}(\mathbf{E}) = \epsilon_0(\chi^{(1)}\mathbf{E} + \chi^{(2)}\mathbf{E}\mathbf{E} + \chi^{(3)}\mathbf{E}\mathbf{E}\mathbf{E} + \dots) \quad (\text{A.26})$$

Eq. (A.22) provides an expression for the restoring forces of the system where ω_0 is the natural resonance frequency of the oscillator, m is the mass of the electron, and $a(b)$ are the coefficients that characterise the strengths of their respective term. Eq. (A.23) gives us the expression for the anharmonic potential. This expression represents the true potential experienced by the oscillator and is obtained by performing an integration on Eq. (A.22). The equation of motion for the system is represented by Eq (A.25) where the external driving force of the electric field (\mathbf{E}) and a damping term led by the damping coefficient (γ) are included. The form of the driving electric field

is provided in Eq. (A.24), where the series is a summation over frequency ω_n . The introduction of multiple frequencies is justified in nonlinear processes such as harmonic generation, four wave mixing or down-conversion, which are all multi-photon processes. In general, a perturbation method approach is taken in solving the nonlinear differential shown in Eq. (A.25). This is to say that the contribution of the higher order terms are small compared to the linear term ($\omega_0^2 \mathbf{x} \gg a\mathbf{x}^2 \gg b\mathbf{x}^3$) and are treated as such. In accordance with this, the trial solution has the form of $\mathbf{x} = \lambda \mathbf{x}^{(1)} + \lambda^2 \mathbf{x}^{(2)} + \lambda^3 \mathbf{x}^{(3)} + \dots$, where λ characterises the strength of the perturbation. Once we solve the differential we can obtain expressions for the electric susceptibility (χ) which are seen in Eq. (A.26) for the polarisation vector (\mathbf{P}). The polarisation vector is the total polarisation per unit volume and expresses the density of induced or permanent electric dipole moments in a dielectric material, thereby providing us with a description of the material's response to an external electric field. The material assumption here is that it is isotropic, that is to say that any parameter and their properties are independent of direction. The expansion coefficients, $\chi^{(i)}$, are the i -th order electric susceptibilities. In addition to that, it is evident that this is a power series expansion in the electric field. The goal of the following subsections will be to derive expressions for the $\chi^{(1)}$ and $\chi^{(3)}$ susceptibilities. From the susceptibility, one can derive expressions for the dielectric constant, index of refraction and optical conductivity, making it fundamental to describing optical phenomena in materials. The derivations shown here are adapted from *Nonlinear Optics* by Robert Boyd [66].

A.2.1 Linear

The linear response of the system is obtained by considering the behaviour of the harmonic oscillator or simply considering the linear terms of equations 1.1-5. The relevant equations are as follows:

$$\frac{d^2 \mathbf{x}(t)}{dt^2} + \gamma \frac{d\mathbf{x}(t)}{dt} + \omega_0^2 \mathbf{x}(t) = -\frac{e}{m} \mathbf{E}(t) \quad (\text{A.27})$$

$$\mathbf{x}(t) = \lambda \mathbf{x}^{(1)}(t) = \lambda \mathbf{x}^{(1)}(\omega_1) e^{-j\omega_m t} + c.c. \quad (\text{A.28})$$

$$\mathbf{E}(t) = \mathbf{E}_1 e^{-j\omega_m t} + c.c. \quad (\text{A.29})$$

$$\mathbf{P}(\mathbf{E}) = \epsilon_0 \chi^{(1)} \mathbf{E} \quad (\text{A.30})$$

We begin by taking the trial solution (A.28) and electric field (A.29) and inserting them into the equation of motion (A.27). By carrying out the differentiation, the following expression is obtained:

$$\mathbf{x}^{(1)}(\omega_m) = \frac{e \mathbf{E}(\omega_m)}{m(\omega^2 + j\gamma\omega_m - \omega_0^2)} \quad (\text{A.31})$$

With an expression for charge displacement, $\mathbf{x}^{(1)}(\omega_m)$, we can define the first order polarisation vector $\mathbf{P}^{(1)}$ as follows:

$$\mathbf{P}^{(1)} = -Ne \mathbf{x}^{(1)}(\omega_m) = \frac{-Ne^2}{m} \frac{1}{(\omega_m^2 - \omega_0^2) + j\gamma\omega_m} \mathbf{E}(\omega_m) = \epsilon_0 \chi^{(1)}(\omega_m) \mathbf{E}(\omega_m) \quad (\text{A.32})$$

where N is the average number of identical individual dipole moments contributing to the polarisation per unit volume, ϵ_0 is the permittivity of vacuum, and $\chi^{(1)}$ is the electric susceptibility. It can be easily followed that the first order electric susceptibility is:

$$\boxed{\chi^{(1)}(\omega_m) = \frac{Ne^2}{m\epsilon_0} \frac{1}{((\omega_0^2 - \omega_m^2) - j\gamma\omega_m)} = \frac{Ne^2}{m\epsilon_0} \frac{1}{\mathcal{D}(\omega_m)}} \quad (\text{A.33})$$

where we have defined a complex denominator function, $\mathcal{D}(\omega_m)$, for mathematical convenience. The susceptibility function can be separated into its real and imaginary components as such:

$$\chi^{(1)} = \chi_{Re}^{(1)} - j\chi_{Im}^{(1)}$$

$$\chi_{Re}^{(1)}(\omega_m) = \frac{\omega_p^2(\omega_0^2 - \omega_m^2)}{(\omega_0^2 - \omega_m^2)^2 + \omega_m^2\gamma^2} \quad (\text{A.34})$$

$$\chi_{Im}^{(1)}(\omega_m) = \frac{\omega_p^2\omega_m\gamma}{(\omega_0^2 - \omega_m^2)^2 + \omega_m^2\gamma^2} \quad (\text{A.35})$$

It is often necessary to separate the real and imaginary components of these quantities because in doing so one can appreciate the isolated effects of loss mechanisms as gleaned from the imaginary component. We can now define the expression for the complex linear refractive index in terms of susceptibility:

$$\tilde{n} = n_0 - j\kappa$$

$$\tilde{n} = \sqrt{1 + \chi^{(1)}}$$

$$n_0(\omega) = \frac{1}{\sqrt{2}} \sqrt{\left(1 + \chi_{Re}^{(1)}(\omega_1)\right) + \sqrt{\left(1 + \chi_{Re}^{(1)}(\omega_1)\right)^2 + \chi_{Im}^{(1)2}(\omega_1)}} \quad (\text{A.36})$$

$$\kappa(\omega) = \frac{1}{\sqrt{2}} \sqrt{-\left(1 + \chi_{Re}^{(1)}(\omega_1)\right) + \sqrt{\left(1 + \chi_{Re}^{(1)}(\omega_1)\right)^2 + \chi_{Im}^{(1)2}(\omega_1)}} \quad (\text{A.37})$$

The real part (n) of \tilde{n} is the linear refractive index, while the complex part (κ) is the extinction coefficient which relates to the absorption coefficient of the material. In performing this derivation, we have related the macroscopic quantity of refractive index to microscopic atomic polarisations as induced by an impinging field. This derivation can be further pursued under the Drude model to obtain complex conductivities but that is beyond the scope of this work.

A.2.2 Nonlinear

Having derived a concise framework for the linear regime, we can now consider the higher order processes. As mentioned previously, the origin of optical/electronic properties is based in the material's crystallographic properties. When considering the second ($\chi^{(2)}$) and third ($\chi^{(3)}$) order

susceptibilities, it is seen that every material exhibits a third order susceptibility, albeit the contribution of $\chi^{(3)}$ is very small. However, for a material to exhibit a second order susceptibility, it must have non-centrosymmetric inversion symmetry. In this case, the $\chi^{(3)}$ term still exists, but is overshadowed by the large $\chi^{(2)}$ term. By default, materials that have a centrosymmetric inversion symmetry have no contribution from the even terms in susceptibility. The second and third order processes are colloquially known as the linear and quadratic electro-optic effect. The use of this verbiage will become clear by the end of this derivation. It would follow that after deriving the relation for $\chi^{(1)}$, the relation for $\chi^{(2)}$ will be derived. However, the nonlinearity of interest derives from $\chi^{(3)}$, therefore, we will jump directly into deriving the third order susceptibility, however, the framework for solving for $\chi^{(2)}$ follows the same process.

We begin again by laying out the relevant equations as follows:

$$\frac{d^2\mathbf{x}(t)}{dt^2} + \gamma\frac{d\mathbf{x}(t)}{dt} + \omega_0^2\mathbf{x}(t) + b\mathbf{x}^3(t) = -\frac{e}{m}\mathbf{E}(t) \quad (\text{A.38})$$

$$\mathbf{x}(t) = \lambda\mathbf{x}^{(1)} + \lambda^2\mathbf{x}^{(2)} + \lambda^3\mathbf{x}^{(3)} + \dots \quad (\text{A.39})$$

$$\mathbf{E}(t) = \mathbf{E}_1e^{-j\omega_1t} + \mathbf{E}_2e^{-j\omega_2t} + \mathbf{E}_3e^{-j\omega_3t} + c.c. \quad (\text{A.40})$$

$$\mathbf{P}(\mathbf{E}) = \epsilon_0(\chi^{(1)} + \chi^{(3)}\mathbf{E}\mathbf{E})\mathbf{E} \quad (\text{A.41})$$

In similar fashion the trial solution (A.39) is inserted into the nonlinear equation of motion (A.38). By requiring that the terms proportional to λ^n vanishing separately for each value of n , we obtain separate differential equations for each order in $\mathbf{x}^{(1,2,3)}$:

$$\frac{d^2\mathbf{x}^{(1)}(t)}{dt^2} + \gamma\frac{d\mathbf{x}^{(1)}(t)}{dt} + \omega_0^2\mathbf{x}^{(1)}(t) = -\frac{e}{m}\mathbf{E}(t) \quad (\text{A.42})$$

$$\frac{d^2\mathbf{x}^{(2)}(t)}{dt^2} + \gamma\frac{d\mathbf{x}^{(2)}(t)}{dt} + \omega_0^2\mathbf{x}^{(2)}(t) = 0 \quad (\text{A.43})$$

$$\frac{d^2\mathbf{x}^{(3)}(t)}{dt^2} + \gamma\frac{d\mathbf{x}^{(3)}(t)}{dt} + \omega_0^2\mathbf{x}^{(3)}(t) - b(\mathbf{x}^{(1)} \cdot \mathbf{x}^{(1)})\mathbf{x}^{(1)} = 0 \quad (\text{A.44})$$

We can easily recognise that Eq. (A.42) is the equation of motion for the linear regime and the solution found in the previous subsection still applies. Considering Eq. (A.43), we know that in this centrosymmetric media, the second order response is non-existent. Mathematically, the equation is damped but not driven, therefore, the steady-state solution is $\mathbf{x}^{(2)} = 0$. To calculate the third-order response, a slight substitution has been made for ease of derivation where $\mathbf{x}^{(3)} = (\mathbf{x}^{(1)} \cdot \mathbf{x}^{(1)})\mathbf{x}^{(1)}$. By inserting the expression found in the linear regime for first order charge displacement (A.31) into Eq. (A.44), the following expression is obtained:

$$\frac{d^2\mathbf{x}^{(3)}(t)}{dt^2} + \gamma\frac{d\mathbf{x}^{(3)}(t)}{dt} + \omega_0^2\mathbf{x}^{(3)}(t) = -\sum_{mnp} \frac{be^3[\mathbf{E}(\omega_m) \cdot \mathbf{E}(\omega_n)]\mathbf{E}(\omega_p)}{m^3\mathcal{D}(\omega_m)\mathcal{D}(\omega_n)\mathcal{D}(\omega_p)} \times e^{-j(\omega_m+\omega_n+\omega_p)t} \quad (\text{A.45})$$

The summation over m , n and p shows that the equation contains many different frequencies and the complex denominator function, $\mathcal{D}(\omega)$, is the same as defined previously. For ease of derivation, we denote one of the frequencies as $\omega_q = \omega_m + \omega_n + \omega_p$. Now the solution of Eq. (A.45) can be written in the form:

$$\mathbf{x}^{(3)}(t) = \sum_q \mathbf{x}^{(3)}(\omega_q) e^{-j\omega_q t} \quad (\text{A.46})$$

Substituting Eq. (A.46) into Eq. (A.45), we find:

$$\begin{aligned} ((\omega_0^2 - \omega_q^2) - j\gamma\omega_q)\mathbf{x}^{(3)}(\omega_q) &= - \sum_{mnp} \frac{be^3[\mathbf{E}(\omega_m) \cdot \mathbf{E}(\omega_n)]\mathbf{E}(\omega_p)}{m^3\mathcal{D}(\omega_m)\mathcal{D}(\omega_n)\mathcal{D}(\omega_p)} \\ \mathbf{x}^{(3)}(\omega_q) &= - \sum_{mnp} \frac{be^3[\mathbf{E}(\omega_m) \cdot \mathbf{E}(\omega_n)]\mathbf{E}(\omega_p)}{m^3\mathcal{D}(\omega_q)\mathcal{D}(\omega_m)\mathcal{D}(\omega_n)\mathcal{D}(\omega_p)} \end{aligned} \quad (\text{A.47})$$

With this the third order polarisation term and susceptibility can be defined:

$$\begin{aligned} \mathbf{P}^{(3)} &= -Ne\mathbf{x}^{(3)}(\omega_q) = \sum_{mnp} \frac{-Nbe^4}{m^3} \frac{E(\omega_m)E(\omega_n)E(\omega_p)}{\mathcal{D}(\omega_q)\mathcal{D}(\omega_m)\mathcal{D}(\omega_n)\mathcal{D}(\omega_p)} \\ \mathbf{P}^{(3)} &= \sum_{mnp} \epsilon_0 \chi^{(3)}(\omega_q; \omega_m, \omega_n, \omega_p) E(\omega_m)E(\omega_n)E(\omega_p) \end{aligned} \quad (\text{A.48})$$

$$\boxed{\chi^{(3)}(\omega_q; \omega_m, \omega_n, \omega_p) = \frac{-Nbe^4}{m^3\epsilon_0} \frac{1}{\mathcal{D}(\omega_q)\mathcal{D}(\omega_m)\mathcal{D}(\omega_n)\mathcal{D}(\omega_p)}} \quad (\text{A.49})$$

We have now obtained a concise expression for the third order susceptibility. It is clear that the third-order nonlinearity has some form of a four-wave interaction. This expression is sufficient in describing the nonlinear polarisation contribution in this regime but at visual inspection gives minimum phenomenological understanding of the expression. In similar treatment as the linear regime, we can separate the real and imaginary components through tedious algebra, however, we can perform a simplification to obtain a real expression using an empirical rule introduced by Miller [67] which allows us to estimate the magnitude of the susceptibility term under a few assumptions. The atomic number (N) is nearly constant ($\sim 10^{22} \text{ cm}^{-3}$) for all condensed matter, and the parameters m and e are both fundamental constants. We can estimate the size of nonlinear coefficient b by considering that the linear and nonlinear contributions to the restoring force given by Eq. (A.22) will become comparable to the atomic dimension d , which says $m\omega_0^2 d = mbd^3$, implying $b = \frac{\omega_0^2}{d^2}$. Considering the nonresonant excitation case approximating $\mathcal{D}(\omega)$ as ω_0^2 and $N \sim 1/d^3$, we can obtain the following simplified expression:

$$\boxed{\chi^{(3)} \simeq \frac{Nbe^4}{\epsilon_0 m^3 \omega_0^8} = \frac{e^4}{\epsilon_0 m^3 \omega_0^6 d^5}} \quad (\text{A.50})$$

Having treated the linear and nonlinear terms in isolation, we can now discuss effective behaviour of the material when the third-order nonlinearity is probed. Considering the total polarisation vector for a third-order nonlinearity given in Eq. (A.41), the term in the bracket can be isolated and defined as the effective susceptibility as thus:

$$\chi^{eff} = \chi^{(1)} + \chi^{(3)}|\mathbf{E}(\omega)|^2 \quad (\text{A.51})$$

Using a similar relationship shown for the linear regime, the real part of the total refractive index is derived as such:

$$\begin{aligned} \tilde{n} &= \sqrt{1 + \chi^{eff}} = \sqrt{1 + \chi^{(1)} + \chi^{(3)}|\mathbf{E}(\omega)|^2} \\ \tilde{n} &= \sqrt{n_0^2 + \chi^{(3)}|\mathbf{E}(\omega)|^2} \\ \tilde{n} &= n_0 \sqrt{1 + \frac{\chi^{(3)}|\mathbf{E}(\omega)|^2}{n_0^2}} \end{aligned} \quad (\text{A.52})$$

In general, the latter term under the square root is much smaller than 1. Using the Taylor series expansion, the effective refractive index can be rewritten as:

$$\tilde{n} \approx n_0 + \frac{\chi^{(3)}}{2n_0}|\mathbf{E}(\omega)|^2$$

$$\boxed{\tilde{n} = n_0 + \Delta n = n_0 + n_2 I} \quad (\text{A.53})$$

where n_0 is the previously derived linear refractive index (A.36), Δn is the third-order nonlinear susceptibility-induced refractive index change, and n_2 is the nonlinear refraction coefficient. Here we have substituted $|\mathbf{E}(\omega)|^2$ by I , as they are proportional to each other. More specifically, $|\mathbf{E}(\omega)|^2 = \frac{1}{\epsilon_0 c n_0} I$. A qualitative analysis of Eq. (A.53) tells us that there is a linear dependence on the intensity of the impinging field on the contribution of nonlinear refraction to the cumulative refractive behaviour. As mentioned previously, this effect is colloquially known as the quadratic electro-optic effect, as the nonlinear effect is proportional to the square of the electric field.

A.3 Nonlinear Refraction

In this section we will derive the general theory that the Z-scan measurement is based on and how far-field transmittance is used to extract the effects of nonlinear refraction. The derivation is adapted from Sheik-bahae's first two articles about this technique [42] [51]. The analysis will follow the changes in the incident beam as it enters and propagates the sample, and then the free space propagation of this modified beam to the aperture and detector plane. Before delving into the mathematics it is

Gaussian beam

The inception of this analysis is at well-known Gaussian beam equation, which has been derived in Appendix A.1. As we will make use of the resulting equation we present it here for easy reference:

$$E(r, z, t) = E_0(t) \left[\frac{w_0}{w(z)} \exp \left(-\frac{r^2}{w^2(z)} - j \frac{kr^2}{2R(z)} \right) \exp \left(-j\phi(z, t) \right) \right] \quad (\text{A.54})$$

where z is the distance along the propagation axis, $w(z) = w_0 \sqrt{1 + \frac{z^2}{z_R^2}}$ is the beam radius, w_0 is the beam waist (3.5, A.16), $R(z) = z \left(1 + \frac{z^2}{z_R^2} \right)$ is the radius of curvature of the wavefront, z_R is the Rayleigh length (3.6), and λ and k are the usual laser wavelength and wave vector, respectively. The leading term $E_0(t)$ is the temporal envelope of the laser pulse. Since we are after the induced phase variations from the samples, we focus on the phase term, ϕ . However, the term is a function of only z and not r , which tells us that radial phase variations are considered to be constant in this term. For our purposes, we are probing the radial phase variations, therefore, the phase function $\phi(z, t)$ will be omitted but a new phase term, $\Delta\phi(r)$, will be used.

Induced phase shift

The total refraction phenomenon in the sample will include the linear (n_0) and nonlinear term (n_2) as shown in Eq. (A.53): $\tilde{n} = n_0 + \Delta n = n_0 + n_2 I$. For the analysis, a thin sample approximation is utilised. The sample can be considered thin if the sample length (L) does not induce spatial variations in the beam diameter either due to diffraction or nonlinear refraction. This allows for the assumption that the interaction between the sample and the laser pulse occurs only at a single point and not over the entire interaction length of the sample. This condition is satisfied if the following two inequalities are satisfied: $L \ll z_R$ for diffraction, and $L \ll \frac{z_R}{\Delta\phi(0)}$ for nonlinear refraction. In general, $\Delta\phi(0)$ is very small and less restrictive condition for diffraction, $L < z_R$, proves sufficient as demonstrated through experiment [51]. With this assumption and a slowly-varying envelope approximation (SVEA), where the spatial and temporal amplitudes change slowly as compared to wavelength, the phase and the amplitude of the electric field can be described by the following pair of differential equations:

$$\frac{d\Delta\phi(r, z, t, L)}{dz'} = \Delta n(I)k \quad (\text{A.55})$$

$$\frac{dI}{dz'} = -\alpha(I)I \quad (\text{A.56})$$

where z' is the propagation depth in the sample and $\alpha(I)$ includes the linear and nonlinear absorption terms. These equations govern the propagation of a Gaussian beam through the sample. Ignoring absorptive effects for now, and considering only a third-order nonlinearity Eq. (A.55) can be solved and an expression for the phase shift at the exit surface of the sample is:

$$\Delta\phi(r, z, t, L) = \Delta\phi_0(z, t, L) \exp\left(-\frac{2r^2}{w^2(z)}\right)$$

$$\Delta\phi_0(z, t, L) = \frac{\Delta\Phi_0(t, L)}{1 + \frac{z^2}{z_R^2}}$$

$$\Delta\Phi_0(t, L) = k\Delta n(t)L_{eff} \quad (\text{A.57})$$

where $\Delta\Phi_0(t)$ is the on-axis phase shift at the focal plane and is define above, L_{eff} is the effective interaction length of the sample defined as $L_{eff} = \frac{1-e^{-\alpha L}}{\alpha}$, α is the linear absorption coefficient, and $\Delta n(t)$ is defined by $n_2 I_0(t)$ where $I_0(t)$ is the on-axis irradiance . We can now rewrite the equation for the Gaussian beam at the exit surface of the sample by including the induced phase shift:

$$E_e(r, z, t) = E(r, z, t)e^{-\frac{\alpha L}{2}} e^{j\Delta\phi(r, z, t, L)} \quad (\text{A.58})$$

Propagation through free space

By using the complex electric field exiting the sample (A.58), the far-field pattern of the beam at the aperture plane can be determined. By using a Gaussian Decomposition (GD) procedure as done by Weaire *et al.* [68] and also by Sheik-Bahae *et al.* [51], we can obtain the far-field pattern. The basic idea behind GD is to use a basis set of Gaussian beams to construct the desired optical field, through individual propagation of the beams (m) and then coherently resumming the individual beam. This motivation for following such a procedure was the increased complexity in mathematics when an optical field encountered a surface [69]. Gaussian beams are the choice function for the implementation of this method because the Fourier transform of a Gaussian function is another Gaussian function, so the functional form of the Gaussian beam does not change during propagation. In comparison, a plane wave changes to an Airy function when propagated to the far-field. If you start with a collection of Gaussian beams, you will finish with a collection of Gaussian beams [70]. The electric field at the exit plane is decomposed into a summation of Gaussian beams through a Taylor series expansion of the nonlinear phase term. Since, only small phase changes are considered, only the first few terms of the series need to be considered:

$$e^{j\Delta\phi(r, z, t)} = \sum_{m=0}^{\infty} \frac{[j\Delta\phi_0(z, t)]^m}{m!} e^{-2mr^2/w^2(z)} \quad (\text{A.59})$$

By including the effects of propagation (A.59) to the initial beam curvature (A.54), we obtain the resultant field pattern (E_a):

$$E_a(r, t) = E(r = 0, z, t)e^{-\frac{\alpha L}{2}} \sum_{m=0}^{\infty} \frac{[j\Delta\phi_0(z, t)]^m w_{m0}}{m! w_m} \exp\left(-\frac{r^2}{w_m^2(z)} - j\frac{kr^2}{2R_m(z)} + j\theta_m\right) \quad (\text{A.60})$$

By denoting d as the propagation distance from the exit surface to the aperture plane and defining $g = 1 + \frac{d}{R(z)}$, the Gaussian beam parameters for m individual beams can be defined:

$$w_{m0}^2 = \frac{w^2(z)}{2m + 1} \quad (\text{A.61})$$

$$w_m^2 = w_{m0}^2 \left[g^2 + \frac{d^2}{d_m^2} \right] \quad (\text{A.62})$$

$$R_m = d \left[1 - \frac{g}{g^2 + d^2/d_m^2} \right]^{-1} \quad (\text{A.63})$$

$$\theta_m = \tan^{-1} \left[\frac{d/d_m}{g} \right] \quad (\text{A.64})$$

$$d_m = \frac{kw_{m0}^2}{2} \quad (\text{A.65})$$

Transmittance through aperture

With a form for the optical field function which includes the a sample induced phase shift and propagation to the aperture plane, the transmitted power through the aperture can be obtained by spatially integrating Eq. (A.60) from $r = 0$ to $r = r_a$, where r_a is the radius of the aperture:

$$P_T(\Delta\Phi_0(t)) = c\epsilon_0 n_0 \pi \int_0^{r_a} |E_a(r, t)|^2 r dr \quad (\text{A.66})$$

Including the temporal variation of the pulse, the normalised Z-scan profile can be related to the transmitted power as:

$$T(z) = \frac{\int_{-\infty}^{\infty} P_T(\Delta\Phi_0(t)) dt}{S \int_{-\infty}^{\infty} P_i(t) dt} \quad (\text{A.67})$$

where $P_i(t) = \pi w_0^2 I_0(t)/2$ is the instantaneous input power within the sample, $S = 1 - \exp(-2r_a^2/w_a^2)$ is the linear transmittance through the aperture, and w_a is the radius of the beam at the aperture plane. Let us first consider a steady state result which implies an instantaneous nonlinearity and a temporally square pulse, which is equivalent to continuous wave (CW) source. Considering only a cubic nonlinearity and the assumption of a small phase change ($|\Delta\Phi_0| \gg 1$), only the first two terms in Eq.(A.60) need to be retained. Following these simplifications and making use of the

relations (A.61 -A.65), the Z-scan transmittance (A.67) can be rewritten as:

$$T(z, \Delta\Phi_0) = \frac{|E_a(z, r = 0, \Delta\phi_0)|^2}{|E_a(z, r = 0, \Delta\phi_0 = 0)|^2}$$

$$T(z, \Delta\Phi_0) = \frac{|(g + jd/d_0)^{-1} + j\Delta\phi_0(g + jd/d_1)^{-1}|^2}{|(g + jd/d_0)^{-1}|^2} \quad (\text{A.68})$$

Using the far-field condition $d \gg z_R$, we can simplify the above equation to gain a geometry-independent normalised transmittance as:

$$T(z, \Delta\Phi_0) \simeq 1 - \frac{4\Delta\Phi_0 x}{(x^2 + 9)(x^2 + 1)} \quad (\text{A.69})$$

where $x = z/z_R$. This equation can be fit to normalised Z-scan data to obtain a best fit value for $\Delta\Phi_0$. This expression can be further simplified, by considering the normalised peak-valley separation, ΔT_{p-v} . By differentiating Eq. (A.69) by z ($dT(z, \Delta\Phi_0)/dz = 0$), the following relations are obtained:

$$x_{p,v} = \pm \sqrt{\frac{\sqrt{52} - 5}{3}} \simeq \pm 0.858 \quad (\text{A.70})$$

$$\Delta Z_{p-v} = \pm 1.7z_0 \quad (\text{A.71})$$

$$\Delta T_{p-v} = \frac{8|x_{p,v}|}{(x_{p,v}^2 + 9)(x_{p,v}^2 + 1)} \Delta\Phi_0 = 0.406\Delta\Phi_0 \quad (\text{A.72})$$

For a small $|\Delta\Phi_0|$, the peak and valley occur a distance of ± 0.858 around the focus (A.70, A.71). In order to simplify the fitting process, a simple algebraic relation (A.72) is found. Numerical calculations show that this relation is accurate to within 0.5% for $|\Delta\Phi_0 \leq \pi|$. To include the effect of a finite aperture we can multiply Eq. (A.72) by $(1 - S)^{0.25}$, where S is the previously defined linear transmittance through the aperture.

Transient solution

The steady-state results can be extended to include transient effects induced by pulsed radiation by using the time-averaged index change $\langle \Delta n(t) \rangle$:

$$\langle \Delta n(t) \rangle = \frac{\int_{-\infty}^{\infty} \Delta n_0(t) I_0(t) dt}{\int_{-\infty}^{\infty} I_0(t) dt} \quad (\text{A.73})$$

With a nonlinearity having an instantaneous response and decay times relative to the pulsewidth of the laser, for a temporally Gaussian pulse the time averaged index change and phase shift are:

$$\langle \Delta n(t) \rangle = \Delta n / \sqrt{2}$$

$$\langle \Delta\Phi_0(t) \rangle = \Delta\Phi_0\sqrt{2} \quad (\text{A.74})$$

where Δn now represents the peak-on-axis index change at focus and $\Delta\Phi_0 = kn_{2,eff}I_0(t)L_{eff}$. The $\sqrt{2}$ is an averaging factor for the instantaneous Kerr nonlinearity for a Gaussian pulse. Now the nonlinear index of refraction can be determined via a simple substitution:

$$n_{2,eff} = \frac{\sqrt{2}\Delta\Phi_0}{k_0I_0L_{eff}} \quad (\text{A.75})$$

Eq. (A.75) provides a simplistic expression for the n_2 value which can be extracted from the Z-scan data. Most importantly it accounts for the temporal effects when the pulse width of the source becomes comparable to the duration of the nonlinearity or simply the relaxation coefficient.

Critical Power

We will derive an expression for the critical power required for self-refraction to occur and dominate diffraction. The following discussion is taken from two different texts, namely *"Nonlinear Optics: Theory, Numerical Modeling, and Applications"* by Banerjee [8] and *Laser Physics* by Milonni and Eberly [71].

The wave equation (A.5) for the electric field ($\mathbf{E} = E_0e^{-j\omega t}$) is derived in Appendix A.1. By substituting Eq. (A.53) into the equation to account for refraction, approximating $n_2 \ll n_0$, we obtain:

$$\nabla^2\mathbf{E} - \frac{n^2}{c^2}\frac{\delta^2\mathbf{E}}{\delta t^2} \approx \nabla^2\mathbf{E} - \frac{1}{c^2}(n_0^2 + 2n_0n_2\mathbf{E}^2)\frac{\delta^2\mathbf{E}}{\delta t^2} = 0 \quad (\text{A.76})$$

Invoking the paraxial approximation as done in the derivation of the Gaussian Beam equation (A.1) and averaging over an optical period results in:

$$\nabla_T^2 E_0 + 2jk\frac{\delta E_0}{\delta z} + \frac{k^2 n_2}{n_0}|E_0|^2 E_0 = 0 \quad (\text{A.77})$$

where $k = n_0\omega/c$ is the usual wave vector and ∇_T^2 is the transverse Laplacian. The transverse term accounts for changes in the beam perpendicular to the propagation axis, thus encompassing the effects of diffraction. Due to the term accounting for transverse changes, the term is dependent on size of the beam or the cross section. By denoting the cross section radius as a_0 , we can simplify the term as: $\nabla_T^2 E_0 \sim a_0^{-2} E_0$. The $\frac{k^2 n_2}{n_0}|E_0|^2 E_0$ contains the nonlinear refraction term and describes the self-refraction in the sample. It follows that in order for nonlinear refraction to dominate diffraction, this term must be comparable to the transverse term: $\frac{k^2 n_2}{n_0}|E_0|^2 E_0 \sim a_0^{-2} E_0$, which simplifies to $a_0^2 |E_0|^2 \sim \frac{n_0}{k^2 n_2}$.

The beam intensity I is proportional to the square of the electric field ($|E_0|^2$) via the relation $I = (n_0 c \epsilon_0 / 2) |E_0|^2$. Intensity is simply power per unit area (W/cm^2), therefore, to obtain a critical power the critical intensity must be multiplied by the cross section of the beam as follows:

$$P_{cr} \sim (\pi a_0^2) I = \frac{\pi n_0 c \epsilon_0}{2} a_0^2 |E_0|^2$$

$$P_{cr} = \frac{\pi n_0 c \epsilon_0}{2} \frac{n_0}{k^2 n_2}$$

$$P_{cr} = \frac{\pi n_0^2 c \epsilon_0}{2 k^2 n_2}$$

$$\boxed{P_{cr} = \frac{c \epsilon_0 \lambda^2}{8 \pi n_2}} \quad (\text{A.78})$$

From this expression it is seen that the beam power must exceed this threshold, *not the intensity*, for self-refraction to occur. Even if the beam is focused tighter, self-refraction will not occur as diffraction will also increase with a reduction in beam diameter.

Appendix B

Supplementary

Table B.1: Catalog of optical components and controllers used in experimental set-ups

Identifier	Optical Component	Manufacturer/ Part (Number)	Notes
Z-scan experimental set-up [Figure 3.2]			
	Modelocked Ti:Sapphire Tunable Laser	Coherent Chameleon Vision S	$\lambda = 690 - 1040$ nm $\tau_{pulse} = 75$ fs $f = 80$ MHz $M^2 < 1.1$
HWP	Zero-Order Half-Wave Plate	Thorlabs WPH05M-780 [72]	Antireflection coating: 780 nm
RM	Rotation Mount	Thorlabs RSP1X15 [73]	360^0 continuous or 15^0 indexed rotation
GLP	Glan-Laser Calcite Polarizer	Thorlabs GL10-B [74]	Clear Aperture: 10 mm Antireflection coating: 650-1050 nm
M	Protected Silver Mirror	Thorlabs PF10-03-P01 [75]	-
PCX	N-BK7 Plano-Convex Lens	Thorlabs LA1509-B-ML [76]	Focal length = 100.0 mm Antireflection coating: 650-1050 nm
GoQ	Graphene on Quartz substrate	ACS Material CVQZ1011 [77]	CVD Graphene grown on copper, transferred onto substrate
Stage	Motorised Translation Stage	Thorlabs PT1-Z8 [78]	Travel range: 25 mm Resolution: 50 nm
NP-BS	Cube-Mounted, Non-Polarizing, 50:50 Beamsplitter Cube	Thorlabs CCM1-BS014/M [79]	Antireflection coating: 700-1100 nm
ND	Neutral Density Filter	Thorlabs ND01A [80]	Optical Density = 0.1 ($T = 79\%$)
BCX	N-BK7 Bi-Convex Lens	Thorlabs LB1676-B-ML [81]	Focal length = 100.0 mm Antireflection coating: 650-1050 nm
AP	Precision Pinhole	Thorlabs P500S [82]	Diameter = 500 ± 10 μm
CA OA	Germanium Detector	Newport 918D-IR-OD3R [83]	Spectral range: 780-1800 nm OD3 Attenuator Sensor size: 3 mm
-	Newport Benchtop Optical Power and Energy Meter	Newport 2936-C [84]	Dual Channel USB interface Sampling Rate: 250 kHz
-	Beam Profiler	Thorlabs 2936-C [52]	Dual scanning slit Min beam diameter: $2.5 \mu m$ Max beam diameter: 9 mm 13.5% clip width
-	T-Cube DC Servo Motor Controller	Thorlabs TDC001 [85]	-

Identifier	Optical Component	Manufacturer/ Part (Number)	Notes
Prism-pair pulse stretching experimental set-up [Figure 4.1]			
PSM	N-SF11 Equilateral Dispersive Prism	Thorlabs PS853 [86]	25 mm
GblMt	Ultima Gimbal Prism Mount, 1 in., 100 TPI Adjustment Screws	Newport UGP-1 [87]	-
POM	Pick-off mirror (D-shaped mirror and mount)	Thorlabs PFD10-03-P01 [88] KM100D [89]	-
HRM	1"x1" Hollow Roof Prism Mirror	Thorlabs HRS1015-P01 [90]	-
Pump-probe experimental set-up [Figure 5.1]			
$\lambda/2_{(900)}$	1" Achromatic Half-Wave Plate	Thorlabs AHWP10M-980 [91]	SM1-Threaded Mount, 690 - 1200 nm
P-BP	Polarising Beamsplitter Cube	Thorlabs CCM1-PBS253/M [92]	30 mm Cage Cube-Mounted
Chp	Optical Chopper	-	-
Pol1/2	1/2" Mounted VIS Linear Polariser	Thorlabs LPVIS050-MP2 [93]	-
Pel	1" Pellicle Beamplitter	Thorlabs BP145B3 [94]	Coated for 45:55 (R:T) Split Ratio for 1-2 μm
Refl-L	Broadband Hollow Retroreflector	Newport UBBR2.5-5S [95]	63.5 mm, 5 arc sec parallelism, 450-10,000 nm
Refl-S	Broadband Hollow Retroreflector	Newport UBBR1-2S [96]	1.0 in, 2 arc sec parallelism, 450-10,000 nm